UNIVERSITY OF TWENTE

Hybrid and disturbance-observer-based control of a peristaltic pump

Master's thesis

Author:

T.J.C. Tijman op Smeijers

Examination committee:

dr.ir. W.B.J. Hakvoort*
dr.ir. M.A. Beijen*,**
dr.ir. A.Q.L. Keemink*
ir. G.J. Boerrigter**
dr.ir. S.J.A.M. van den Eijnden***

February 7, 2024

Master programme of Mechanical Engineering
Faculty of Engineering Technology
Department of Precision Engineering (MS^3)

* University of Twente, Faculty of Engineering Technology
** DEMCON High-Tech Systems Enschede B.V.
*** Eindhoven University of Technology, Department of Mechanical Engineering

Preface

This thesis marks the conclusion of my time as a master's student at the University of Twente. It is my final work towards obtaining a degree for the Master Mechanical Engineering. Throughout my thesis, I learned a lot, ranging from modeling extensive mechatronic systems to testing my own controller designs on complex experimental setups. I found great enjoyment in working on it for the past months and hope you will enjoy reading it as well.

I would like to thank everyone who contributed to this thesis, but especially my supervisors Michiel Beijen and Gijs Boerrigter. The amount of detail in the feedback I received from you and the extensive discussions we had on all sorts of topics related to my thesis were very valuable to me and contributed a lot to my development. The genuine interest and enthusiasm you showed in combination with the casual ambiance we shared was something I greatly valued. Thanks a lot!

Thijs Tijman op Smeijers

Oldenzaal, Februari 7, 2024

Summary

Peristaltic pumps are used for transporting liquids within disposable tubes and are commonly found in medical devices. A rotating pump wheel with several rollers is placed against the tube, such that a certain amount of liquid is trapped between two consecutive rollers and subsequently "pushed" through the tube. The peristaltic pump principle, however, introduces disturbances, thereby distorting the desired rotational speed of the pump. Demcon recently developed a peristaltic pump for one of its medical devices. The pump uses linear proportional plus double integral (PI2) control to reject the aforementioned disturbances. However, linear control suffers from fundamental trade-offs between performance and stability, thereby posing limits on disturbance rejection. To further improve upon disturbance rejection of the peristaltic pump, this thesis proposes both a hybrid and a disturbance-observer-based control strategy.

The hybrid control strategy makes use of the *hybrid integrator-gain system* (HIGS). The HIGS can be exploited for constructing nonlinear filter elements that mimic the amplification characteristics of classical linear filters such as integrators and low-pass filters, but with reduced phase lag. From a design point-of-view, these HIGS-based filters provide additional freedom in controller tuning as gain and phase are no longer related via Bode's gain-phase relationship. This, in turn, allows for achieving higher bandwidths and improved disturbance rejection capabilities without compromising transient performance and robustness margins.

This thesis presents a novel HIGS-based PI2 controller that reduces the steady-state error of the motor speed while additionally improving transient performance and maintaining robustness margins compared to linear PI2 control. An initial design is presented by means of a conference paper. Subsequent thorough analysis of HIGS-based PI2 controller design resulted in a structured tuning methodology for HIGS-based PI2 controllers, eventually presenting an improved design compared to the paper. Simulation studies indicate comparable performance at higher speeds but up to 24.7% improvement in root-mean-square (RMS) value at lower speeds with the new HIGS-based PI2 design compared to the HIGS-based PI2 design from the paper. Experimental validation of the new design on the peristaltic pump demonstrates up to 30.1% RMS improvement over linear PI2 control, with additional transient improvements up to 50.0% in overshoot for similar rise time, all while maintaining the same robustness margins.

The disturbance-observer-based control strategy considered is called *inversion-based disturbance-observer-based control* (IBDOBC). The basic idea behind IBDOBC is to estimate input disturbances and/or uncertainties using an inverse nominal plant model and directly compensate the controller output with the estimate. IBDOBC is an addition to a conventional feedback controller, which could for example be linear or HIGS-based. The feedback controller can conventionally be designed according to tracking performance specifications and stability, whilst IBDOBC is used to further reject disturbances and suppress uncertainties. This thesis presents an IBDOBC design that allows for reducing the steady-state error of the motor speed of the peristaltic pump. Experimental validation of the IBDOBC design in combination with linear PI2 control showed improvements up to 44.8% in terms of RMS value compared to linear PI2 control, whereas the IBDOBC design in combination with HIGS-based PI2 control showed improvements up to 50.5%.

Contents

Chapter 1

Introduction

1.1 Peristaltic pumps

Peristaltic pumps are used for the transport of liquids within plastic tubes. A rotating pump wheel with several rollers is placed against the tube, such that a certain amount of liquid is trapped between two consecutive rollers and subsequently "pushed" through the tube [1]. Because there is no direct contact between the pump wheels and the fluid, there is no chance of fluid contamination. Therefore, typical applications of peristaltic pumps can be found in medical devices where the flow goes through disposable tubes [2, 3].

A downside of peristaltic pumps is the occurrence of flow and pressure ripples in the fluid, which is inherent to the peristaltic pump principle. The periodicity of these ripples directly depends on the rotational speed of the pump and their presence distorts this speed. Besides, effects such as non-perfect commutation of the (brushless) DC motor and friction can further disturb the desired motor speed. In this thesis, all effects contributing to these ripples/pulsations about the desired motor speed are referred to as the *pump ripple*.

Recently, Demcon developed a peristaltic pump for one of its medical devices, schematically shown in Figure 1.1. With the current linear feedback controller, the aforementioned pump ripple is strongly visible in typically measured performance plots. This is illustrated in the time domain in Figure 1.2a, where a clear pulsation effect about the setpoint value of 3 rotations per second (rps) can be observed. Figure 1.2b shows the corresponding amplitude spectrum, indicating several pump ripple frequencies. A dominant peak is visible at 12 Hz, which is 4 times the setpoint speed in rps. The factor 4 follows from the fact that there are 8 pump wheels per rotation and there is a transmission ratio of 2 between the two pulleys within the pump, hence the ratio $8/2 = 4$. Higher harmonics of this effect in Hz occur at every multiple of 4 of the setpoint speed in rps. These peaks are physically a result of the varying resistance between rollers and tube. During pump motion, rollers are continuously engaging with and disengaging from the tube. A sudden increase in resistance is observed upon impact of a roller, whereas the resistance is lost when a roller gets released. Rollers are not placed symmetrically onto the tube, such that engaging and disengaging do not occur at the exact same time instances. Besides, both phenomena might physically not be the exact same effect. Furthermore, Figure 1.2b shows peaks related to non-perfect commutation. The brushless DC motor uses 3-phase sinusoidal commutation, leading to peaks in Hz at multiples of 3 times the setpoint speed in rps.

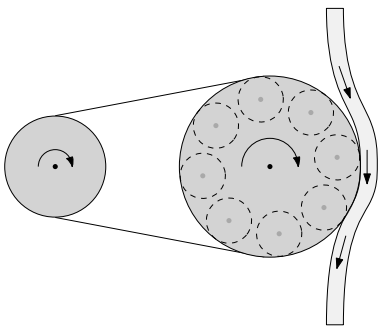

Figure 1.1: Schematic representation of the peristaltic pump developed by Demcon. The actuator is fixed onto the small pulley on the left, whereas a pump wheel with eight rollers is secured onto the larger pulley on the right.

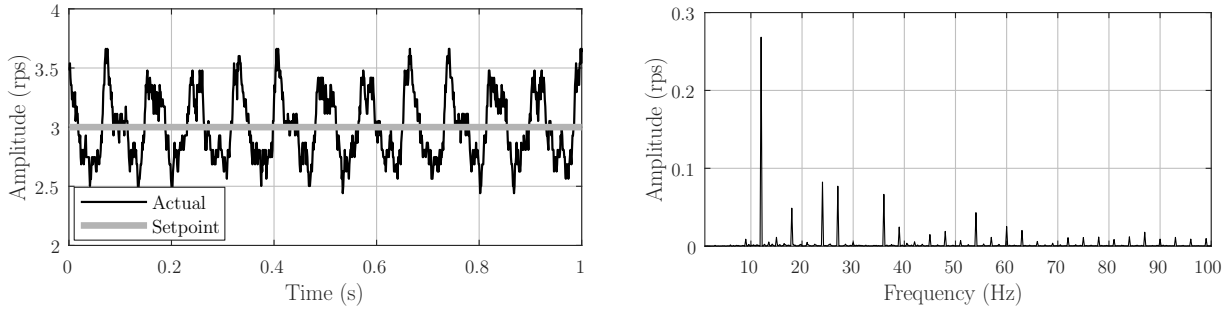

(a) **(b)**

Figure 1.2: Typical pump speed measurement represented (a) in the time domain and (b) in an amplitude spectrum using linear PI2 control.

1.2 Trade-offs in linear PID control design

Linear PID control is widely acknowledged in industry for its simplicity in implementation and limited complexity, while it achieves the desired performance for the majority of mechatronic systems [4]. Currently, the peristaltic pump developed by Demcon uses linear proportional plus double-integral (PI2) to control its speed. The double integral action is used to realize a low sensitivity function at lower frequencies to strongly reject the pump ripple. However, the addition of integral action to the controller directly comes at the cost of an increased sensitivity in other frequency ranges, at the cost of performance. This is an inevitable consequence of the Bode sensitivity integral, often referred to as the "waterbed effect" [5]. At the same time, integral action inevitably adds 90 degrees of phase lag to the system, posing limitations on (robust) stability. This is a result of Bode's gain-phase relationship, stating that the phase of the frequency response of a linear system is completely determined by its magnitude characteristics and vice versa [6]. Besides suffering from limitations in the frequency domain, time-domain limitations also pose restrictions, as adding integral action to the controller could result in overshoot in the step response of the system [5], for example.

1.3 Hybrid control as possible solution

An interesting development in the high-precision industry, where disturbance rejection also plays a crucial role, is the use of the *hybrid integrator-gain system* (HIGS) within typical motion control architectures [7, 8]. The HIGS can be exploited for constructing nonlinear filter elements that mimic the amplification characteristics of classical linear filters such as integrators and low-pass filters, but with reduced phase lag. From a design point-of-view, these HIGS-based filters provide additional freedom in controller tuning as gain and phase are no longer related via Bode's gain-phase relationship. This, in turn, allows for achieving higher bandwidths and improved disturbance rejection capabilities, without compromising transient performance and robustness margins [7].

A HIGS-based controller can be designed using conventional loop-shaping techniques, where the HIGS is approximated in the frequency domain using so-called describing function analysis [9]. However, depending on the severity of nonlinearity with the HIGS-based controller, there might be discrepancies between the expected performance based on these frequency domain approximations and the actual time domain performance [10], such that additional tuning based on time domain information might be necessary, see for example [11].

1.4 Disturbance-observer-based control as possible solution

A common approach to further improve disturbance rejection performance compared to conventional linear PID feedback control involves the addition of a disturbance observer. Disturbance observers reconstruct disturbances from measurable variables, after which the reconstruction is used to determine a control action to compensate for the effect of the disturbances. Uncertainties are typically lumped together with the disturbances, such that these are also compensated for [12, 13]. The conventional feedback controller can generally be designed according to tracking performance specifications and stability, whilst the disturbance observer can separately be designed to further reject disturbances and suppress uncertainties [14].

This thesis considers a disturbance-observer-based control approach called *inversion-based disturbance-observer-based control* (IBDOBC) [15]. IBDOBC makes use of an inverse nominal plant model to reconstruct

input disturbances and uncertainties, eliminating the need for their direct measurement which could be exceedingly complex or unfeasible. The method is suited for both periodic and non-periodic input disturbances. The pump ripple is a primarily periodic effect with quite well-understood dynamics in terms of frequency, amplitude and phase. Note that control methods like repetitive control therefore also seem suited, as these are specifically useful against periodic disturbances [16]. However, the dynamics of the pump ripple of the peristaltic pump developed by Demcon can vary quite strongly due to the use of cheap disposable tubes. Besides, the pump is practically used in a relatively unpredictable environment, such that additional unforeseen (non-periodic) disturbances could be present, justifying the use of IBDOBC.

1.5 Research objective

This thesis aims to further reduce the steady-state setpoint error of the motor speed of the peristaltic pump developed by Demcon using HIGS-based PI2 control and using IBDOBC. With HIGS-based PI2 control, the goal is additionally to maintain the same robustness margins compared to linear PI2 control. Three control designs will be considered:

- HIGS-based PI2 control;
- IBDOBC & linear PI2 control;
- IBDOBC & HIGS-based PI2 control.

The measures to quantify performance are given by:

- The root-mean square (RMS) value of the steady-state setpoint error in the time domain, computed as $\sqrt{\frac{1}{N}\sum_{i=1}^{N}|e_i(t)|^2}$, where e_i is the i^{th} sample of the setpoint error with $i \in [1, N]$, N the number of samples;
- A cumulative power spectral density plot of the steady-state setpoint error.

The main research question of this thesis is formulated as follows:

How is the steady-state performance of the peristaltic pump developed by Demcon improved using HIGS-based PI2 control and using IBDOBC combined with either linear or HIGS-based PI2 control?

The subquestions are given by:

1. What is a suitable plant and pump ripple model design for the peristaltic pump developed by Demcon?
2. How can a HIGS-based PI2 controller be systematically designed and tuned?
3. What is a suitable IBDOBC design that can be combined with both linear and HIGS-based PI2 control for the peristaltic pump developed by Demcon?

1.6 Outline

The remainder of this thesis is divided into four chapters. Chapter 2 provides a nominal plant and pump ripple model of the peristaltic pump developed by Demcon. Chapter 3 starts with a conference paper presenting an initial HIGS-based PI2 controller design for the pump. The chapter subsequently contains several extensions to the paper, resulting in a systematic tuning methodology for HIGS-based PI2 controllers, eventually presenting an improved design compared to the paper. Chapter 4 presents an IBDOBC design for the peristaltic pump developed by Demcon. Chapter 5 provides a reflection of the obtained results by summarizing the main conclusions of this thesis along with recommendations for future research.

Chapter 2

Modeling

2.1 Introduction

This chapter first presents a nominal plant model of the peristaltic pump recently developed by Demcon (Section 2.2). Then, the dynamics of the pump ripple are reconstructed from measurements, after which an analytical model of the pump ripple is derived (Section 2.3). The plant and pump ripple model are used to design, analyze and validate the controllers designed in this thesis.

2.2 Nominal plant model

The peristaltic pump is shown in Figure 2.1. It consists of a pulley with eight rollers that are used to compress a tube that carries fluids. The pulley is driven by a gear belt that is connected to another pulley at the motor side. Typically, two to three rollers compress the tube simultaneously. The pump speed is measured indirectly by differentiating the signal coming from the encoder installed at the motor shaft. A spring-loaded tensioner provides tension within the belt.

A simplified model of the peristaltic pump is shown in Figure 2.2. Here, $J_1 = 7.8 \cdot 10^{-6}$ kgm^2 denotes the combined inertia of the motor and small pulley with radius $r_1 = 8.2 \cdot 10^{-3}$ m. J_1 is connected to the fixed world by means of a rotational damper with damping constant $c = 4.5 \cdot 10^{-3}$ Nms/rad, representing viscous damping of the motor. The gear belt is modeled with translational stiffness $k = 6.8 \cdot 10^4$ N/m and damping $d = 5$ Ns/m. The large pulley has inertia $J_2 = 15.5 \cdot 10^{-6}$ kgm^2 with radius $r_2 = 17 \cdot 10^{-3}$ m. The angular displacements of the small and large pulley are denoted by θ_1 and θ_2, respectively. A motor torque T is generated by voltage U, which will be used to accurately control the angular velocity of the small pulley, denoted by $\dot{\theta}_1$, to a desired speed $\dot{\theta}_r$. The tensioner is not taken into account in the model, because experiments show that its dynamics become apparent above 400 Hz, which is sufficiently far beyond the required system bandwidth. Using first-principles modeling, the relation between voltage U and angular

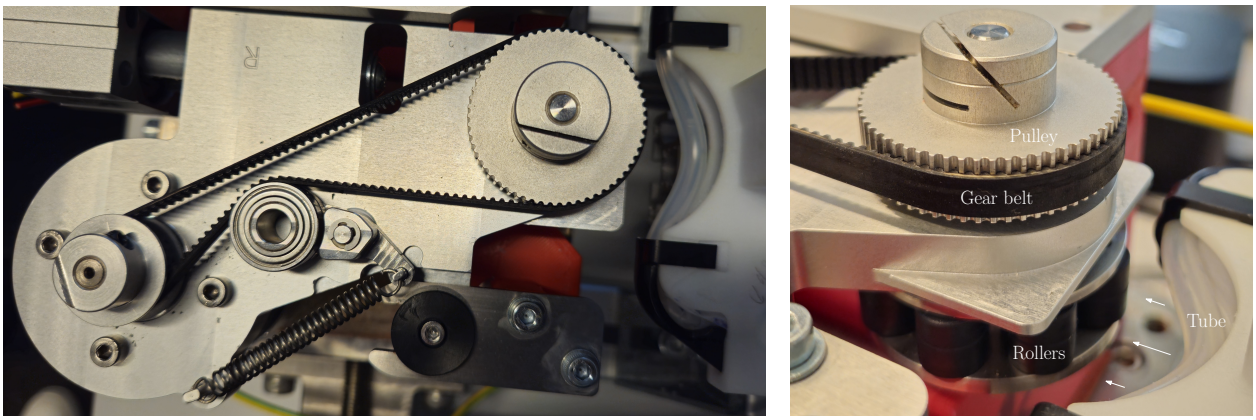

(a) **(b)**

Figure 2.1: Experimental setup of the peristaltic pump including (a) a front view and (b) a zoomed isometric view.

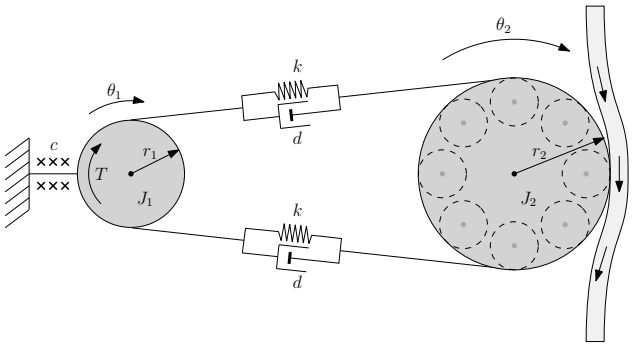

Figure 2.2: Simplified model of the peristaltic pump.

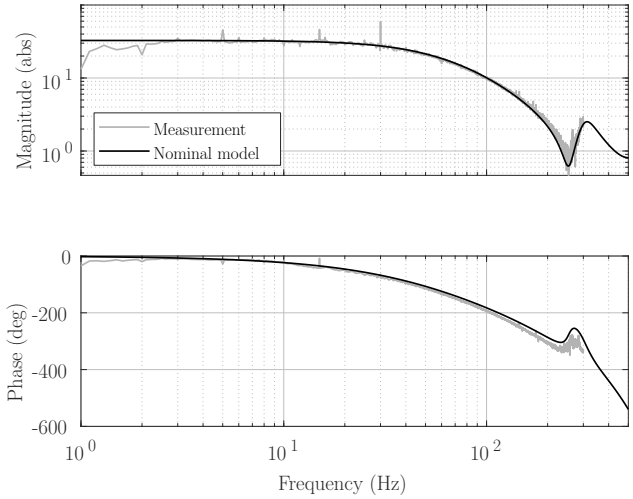

Figure 2.3: Modeled and measured frequency response function from input voltage U in %-duty cycle to output motor speed $\dot{\theta}_1$ in rps.

velocity $\dot{\theta}_1$ is given by $\dot{\theta}_1(s) = P_n(s)U(s)$, with

$$P_n(s) = \underbrace{\frac{1}{2\pi}\frac{1}{J_{tot}s + c}\frac{\frac{1}{\omega_a^2}s^2 + 2\frac{\zeta_a}{\omega_a}s + 1}{\frac{1}{\omega_r^2}s^2 + 2\frac{\zeta_r}{\omega_r}s + 1}}_{\text{Mechanical domain}}\underbrace{\frac{92}{100}\frac{\omega_{act}}{s + \omega_{act}}e^{-st_s}}_{\text{Electrical domain}}, \tag{2.1}$$

where $J_{tot} = J_1 + J_2(\frac{r_1}{r_2})^2 = 11.4\cdot10^{-6}$ kgm^2, $\omega_a = \sqrt{\frac{2kr_2^2}{J_2}} = 253\cdot2\pi$ rad/s, $\omega_r \approx \sqrt{\frac{2kr_1^2 J_{tot}}{J_1 J_2(\frac{r_1}{r_2})^2}} = 306\cdot2\pi$ rad/s, $\zeta_a = 0.062$, $\zeta_r = 0.12$. Constant $\frac{1}{2\pi}$ is required rewrite $\dot{\theta}_1$ from rad/s to rotations per second (rps), whilst constant $\frac{92}{100}$ is required to rewrite torque T in Nm to voltage U in %-duty cycle. Furthermore, $\omega_{act} = 80\cdot2\pi$ rad/s represents the induction pole of the voltage-controlled brushless DC-motor. One computational sample delay of $t_s = 0.001$ s is taken into account to match the behavior of the digital platform that is used to control the system. The model is discretized using the zero-order-hold method. Delay as a result of discrete differentiation of the encoder signal is additionally taken into account. The discretized nominal plant model is finally given by

$$P_n(z) = \frac{113}{100}\frac{(z + 2.55)(z - 1)(z + 0.22)(z^2 + 0.046z + 0.83)}{z^2(z - 0.67)(z - 0.60)(z - 1)(z^2 + 0.51z + 0.64)}. \tag{2.2}$$

A Bode plot of $P_n(z)$ is shown in Figure 2.3, along with a measured frequency response function. At lower frequencies, the plant behavior is characterized by the motor damping c. At higher frequencies, the inertia line $\frac{1}{J_{tot}s}$ is visible with an internal anti-resonance and resonance caused by the gear belt.

Furthermore, the observed rotational speed $\dot{\theta}_1$ suffers from a quantization effect as result of a finite encoder resolution of 4096 pulses per rotation. The encoder is a two-channel encoder, meaning it has a total number of states of $4 \cdot 4096$, such that for a single rotation, the positional resolution equals $\frac{1}{4\cdot4096}$ rotation. Dividing the positional resolution by the sample time $t_s = 0.001$ s subsequently gives a rotational speed resolution equal to 0.061 rps. The effect is independent of the rotational speed of the motor, such that

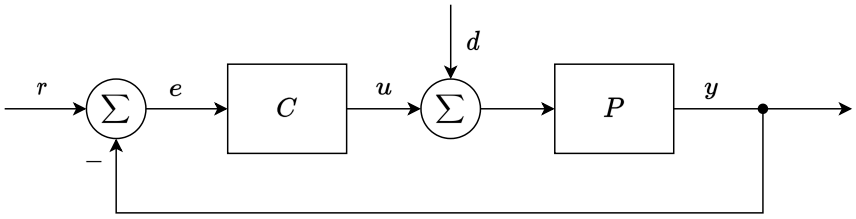

Figure 2.4: General block scheme of feedback control.

discrete steps of 0.061 rps (or a multiple of 0.061 rps) can be expected at every rotational speed. This effect is included in the simulations in this thesis.

2.3 Pump ripple model

In this section, the dynamics of the pump ripple are reconstructed from measurements, after which an analytical linear model of the pump ripple as function of setpoint speed is derived.

2.3.1 Reconstruction

Consider the block scheme in Figure 2.4, with linear feedback controller C, plant P, reference r, error e, controller output u, input disturbances d and output y. In this thesis, plant uncertainties are lumped into the input disturbances, such that the pump ripple is considered part of the input disturbances. A relation for input disturbances d is given by

$$d(z) = P^{-1}(z)y(z) - u(z). \tag{2.3}$$

Parameters y and u can be obtained from measurements, whilst the real plant P can be estimated with nominal model P_n (2.2). However, P_n has a relative degree of 3, such that its inverse has a relative degree of -3 and therefore is non-proper. Besides, P_n contains a non-minimum phase zero ($z = 2.55$), such that inversion results in an unstable transfer function.

To obtain a stable inverse nominal plant model, P_n^{-1} is appended with LTI filter Q, which effectively cancels the unstable pole in P_n^{-1} and replaces it by a similar stable term. Additionally, the Q-filter includes as many delays as needed to ensure properness of QP_n^{-1}. Input disturbances d are subsequently estimated as

$$\hat{d}(z) = Q(z)P_n^{-1}(z)y(z) - Q(z)u(z). \tag{2.4}$$

Note that additionally u is multiplied by the Q-filter. This is to ensure coherence between the first and second term in 2.4 [15]. The Q-filter design itself is given by

$$Q(z) = \frac{B_u(z)}{B_u^*(z)}\frac{1}{z^3}, \tag{2.5}$$

with

$$B_u = z + 2.55, \tag{2.6}$$

and B_u^* representing the adjoint of B_u, i.e. $B_u^*(z) = B_u(1/z)$. Multiplying with B_u cancels the unstable pole in the inverse nominal plant model (2.2), whereas dividing by B_u^* ensures the magnitude characteristics remain unchanged. Three sample delays are added to ensure properness. An analysis on the performance of different Q-filter designs can be found in the appendix in Section 2.5.

Finally, (2.4) can be solved to obtain an estimate of the input disturbances, and thus of the pump ripple. For this, steady-state measurements of u and y are used, which were obtained using controller (3.5). The result is shown in Figure 2.5. The left column in Figure 2.5 shows a sample of 1 second in the time domain. One should note that higher frequency contributions are less accurately reconstructed, as indicated in Figure 2.9 in the appendix in Section 2.5. The right column Figure 2.5 shows a sample of 90 s from the steady state presented in an amplitude spectrum. For reasons of clarity, only frequencies up to 60 Hz are shown.

The largest peak in Hz for each setpoint speed occurs at 4 times the setpoint speed in rps, similar as found in Section 1. The peak is related to the varying resistance/friction between rollers and tube. Higher

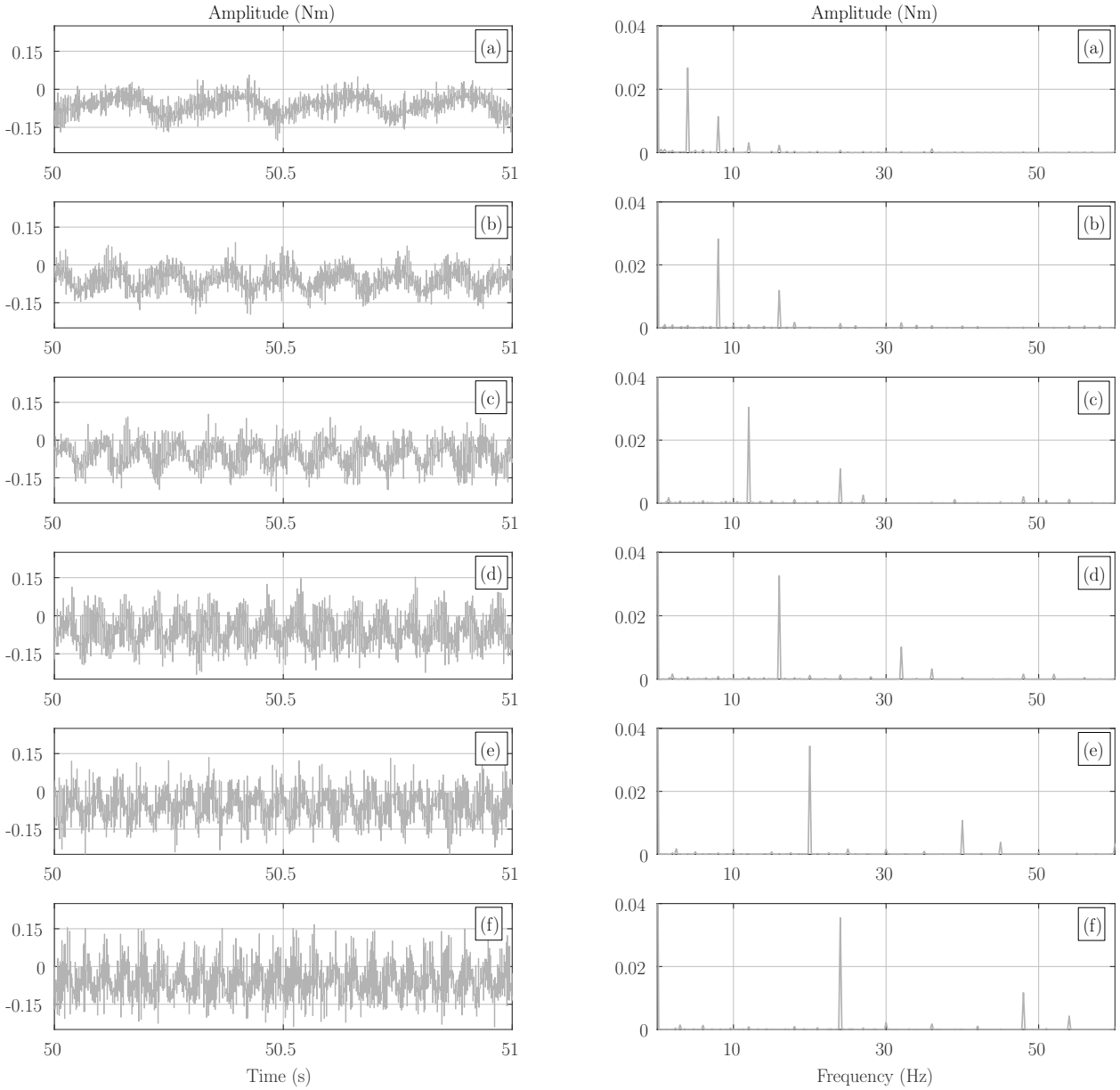

Figure 2.5: Reconstructed input disturbances $\hat{d}$ for setpoint speeds ranging from (a) 1; (b) 2; (c) 3; (d) 4; (e) 5; to (f) 6 rps represented (left column) in the time domain and (right column) in an amplitude spectrum.

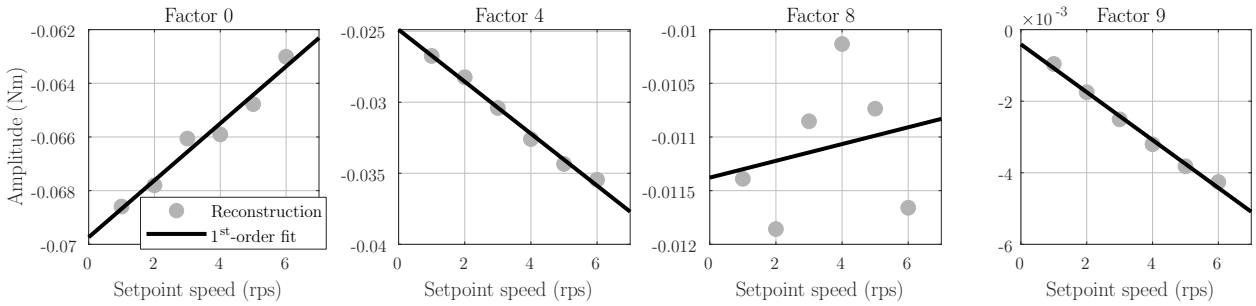

Figure 2.6: Amplitudes of the four different contributions used for the pump ripple model obtained from the amplitude spectrum in Figure 2.5, along with a 1st-order polynomial fit.

harmonics of this effect in Hz seem to occur and every multiple of 4 of the setpoint speed in rps, where the first higher harmonic shows the largest peak for all 6 setpoint speeds. All six setpoint speeds also have a significant peak at 0 Hz, although not clearly visible in Figure 2.5, indicating an offset. The main contribution to this offset seems to be the constant resistance/friction between rollers and tube, since there are two rollers attached to the tube at all times. Furthermore, similar as found in Section 1, peaks in Hz at a multiple of 3 times the setpoint speed in rps can be expected as a result of non-perfect commutation. The third harmonic of this effect, occurring at 9 times the setpoint speed in rps, shows the largest peak for this effect.

2.3.2 Modeling

Using the reconstructed pump ripple dynamics, a model for the pump ripple can be made. Common for all six setpoint speeds in Figure 2.5 are the three largest peaks in Hz at a factor 0, 4 and 8 times the setpoint speed in rps, which all seem to be a result of (varying) resistance/friction due to the peristaltic effect. These three main contributions are used for the pump ripple model. Then, especially for setpoint speeds larger than 1 rps, there is a significant contribution at 9 times the setpoint speed in rps relative to the other peaks, which seems a result of non-perfect commutation. Especially at speeds, and thus higher frequencies, where bandwidth limits might arise and plant roll-off is limited, the effect of these peaks could become significant. This contribution is therefore included in the model. Including these four contributions is expected to give a sufficiently accurate model, such that all other contributions are neglected.

The amplitudes of the four considered contributions in the amplitude spectra in Figure 2.5 (right column) are plotted as grey dots in Figure 2.6 for each of the six setpoint speeds. A 1st-order least-squares polynomial is fitted to the data, which minimizes the sum of offsets between the data points and a 1st-order function. The 1st-order approximation is considered sufficiently accurate. The four polynomial fits are used to construct a linear pump ripple model as function of speed ω. The final model (in Nm) is given by

$$d_{ripple}(\omega) : \begin{cases} 0, & \text{if } \omega = 0, \\ A_0(\omega) + A_1(\omega)\sin(8\omega\pi t) + A_2(\omega)\sin(16\omega\pi t) + A_3(\omega)\sin(18\omega\pi t), & \text{if } \omega > 0, \end{cases} \tag{2.7}$$

where ω represents speed, $A_0(\omega)$ represents the peak in Hz at factor 0 times the setpoint speed in rps, given by

$$A_0(\omega) = 0.0011\omega - 0.070, \tag{2.8}$$

$A_1(\omega)$ the peak in Hz at factor 4 times the setpoint speed in rps, given by

$$A_1(\omega) = -0.0018\omega - 0.025, \tag{2.9}$$

$A_2(\omega)$ the peak in Hz at factor 8 times the setpoint speed in rps, given by

$$A_2(\omega) = 0.000078\omega - 0.011, \tag{2.10}$$

and $A_3(\omega)$ the peak in Hz at factor 9 times the setpoint speed in rps, given by

$$A_3(\omega) = -0.00067\omega - 0.00041. \tag{2.11}$$

Note that the three sinusoids in (2.7) all have a relative phase of zero, which was obtained through manual fitting. Besides, it should be noted that the model is based on steady-state measurement data, such that it might be less accurate in transient periods. The pump ripple model (2.7) is finally illustrated in Figure 2.7 and shown in comparison to the reconstructed pump ripple (2.4).

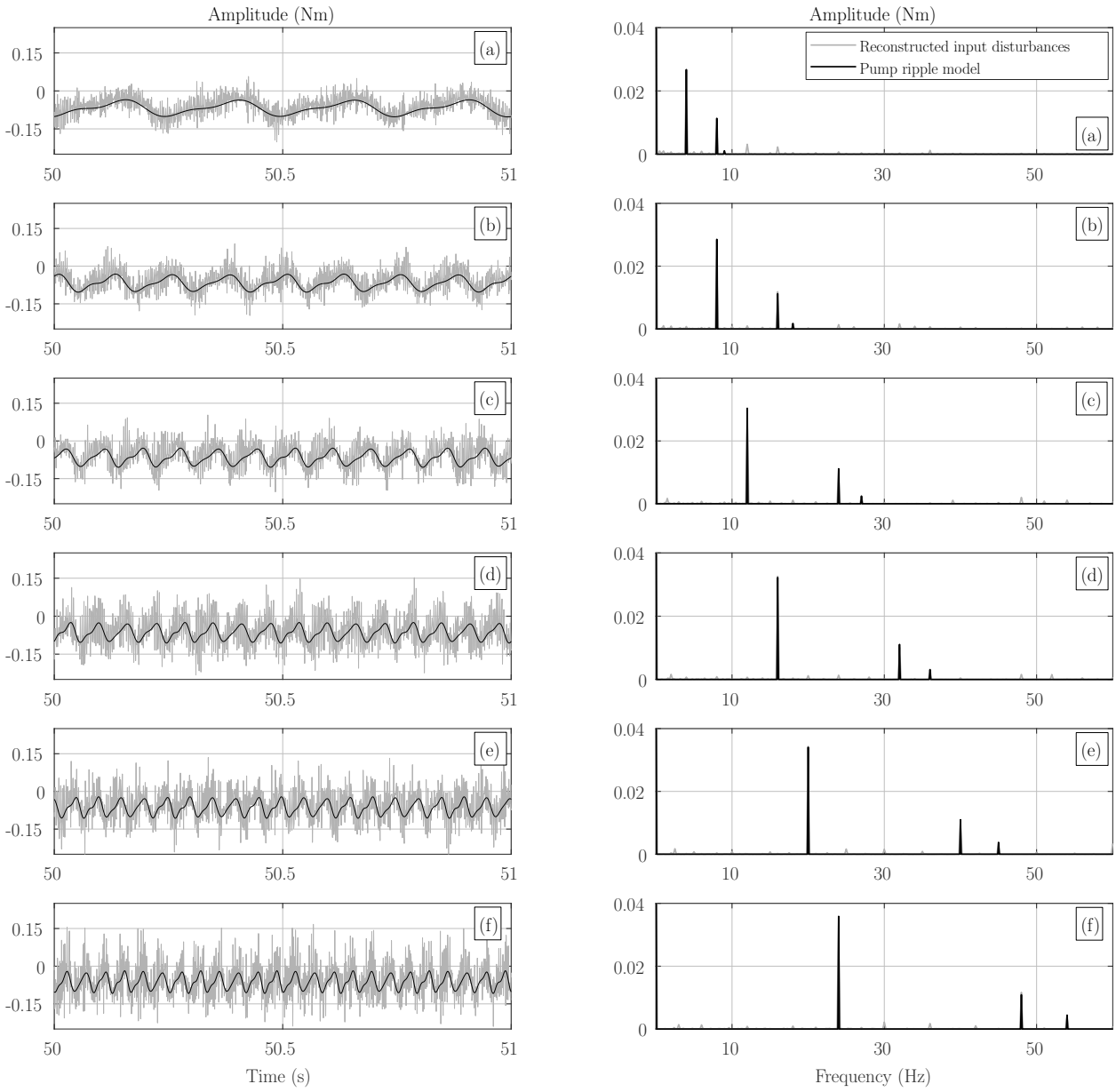

Figure 2.7: Pump ripple model d_{ripple} (black) along with the reconstructed input disturbances $\hat{d}$ (gray) for setpoint speeds ranging from (a) 1; (b) 2; (c) 3; (d) 4; (e) 5; to (f) 6 rps represented (left column) in the time domain and (right column) in an amplitude spectrum.

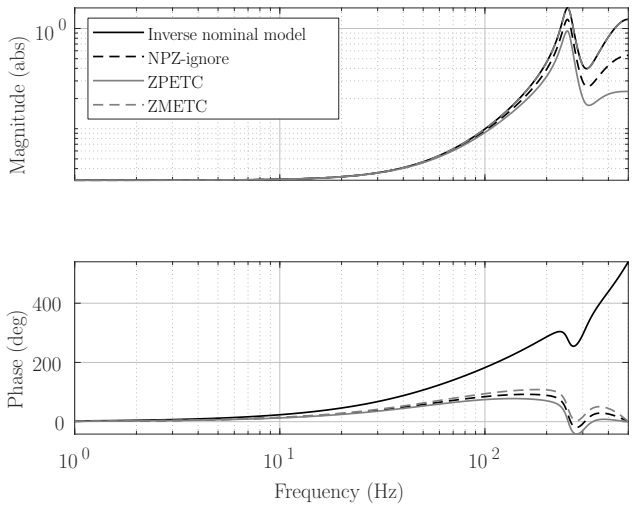

Figure 2.8: Nominal inverse plant model $P_n^{-1}(z)$ and its approximate versions using NPZ-ignore, ZPETC and ZMETC. Note that, compared to 2.16, 2.17 and 2.18, the three expressions are additionally multiplied with $P_n^{-1}(z)$.

2.4 Conclusions

This chapter presented a nominal plant model of the peristaltic pump recently developed by Demcon. Besides, the dynamics of the pump ripple were reconstructed from measurements, after which an analytical linear model of the pump ripple as function of setpoint speed was derived, consisting of the main harmonic contributions of the reconstructed pump ripple.

2.5 Appendix: Q-filter design

Three different Q-filter designs based on literature are considered, being NPZ-ignore (ignore unstable zeros), ZPETC (match phase) and ZMETC (match gain) [17]. Matching phase with ZPETC comes at cost of deviating in phase, while matching gain with ZMETC comes at cost of deviating in phase. NPZ-ignore is a compromise between both methods, where neither gain nor phase is matched, but deviations in phase and gain are less than with ZMETC and ZPETC, respectively.

Mathematically, this is realized as follows. First, nominal plant model P_n (2.2) is written in the form

$$P_n(z) = \frac{113}{100}\frac{B_s(z)B_u(z)}{A(z)}, \tag{2.12}$$

with B_s containing the stable zeros of the numerator, given by

$$B_s(z) = (z-1)(z+0.22)(z^2+0.046z+0.83), \tag{2.13}$$

B_u the unstable zeros of the numerator, given by

$$B_u(z) = z+2.55, \tag{2.14}$$

and with A the denominator, given by

$$A(z) = z^2(z-0.67)(z-0.60)(z-1)(z^2+0.51z+0.64). \tag{2.15}$$

The three different Q-filter designs are subsequently given by

$$\text{NPZ-ignore} = \frac{B_u(z)}{B_u(1)}\frac{1}{z^3}, \tag{2.16}$$

$$\text{ZPETC} = \frac{B_u(z)B_u^*(z)}{B_u^2(1)}\frac{1}{z^3}, \tag{2.17}$$

$$\text{ZMETC} = \frac{B_u(z)}{B_u^*(z)}\frac{1}{z^3}, \tag{2.18}$$

where $B_u^*(z)$ indicates the adjoint of $B_u(z)$, i.e. $B_u^*(z) = B_u(1/z)$. Each method requires three sample delays to ensure properness of $Q(z)P_n^{-1}(z)$.

The models are plotted in Figure 2.8. Note that P_n^{-1} is plotted here just as reference and cannot be implemented in practice because it is unstable and non-proper. As expected, ZMETC has identical magnitude as P_n^{-1}, but deviates in phase. Although not clearly visible Figure 2.8, ZPETC would have identical phase as P_n^{-1}, but due to the three sample delays its phase differs exactly three sample delays. And finally, NPZ-ignore shows behavior which can be considered in between ZMETC and ZPETC both in magnitude and phase.

To make a proper choice between the three methods, the error between the actual input disturbances d and the estimated input disturbances $\hat{d}$ is evaluated for each of the three methods. A low error is desired at lower frequencies, as the pump ripple mainly has lower frequency contributions. For this, a cumulative power spectral density (cPSD) plot is used. Using (2.3) and (2.4), and estimating P with P_n, a formulation of the error is given by

$$\begin{aligned} d_{error}(z) &= P_n^{-1}(z)y(z) - u(z) - (Q(z)P_n^{-1}(z)y(z) - Q(z)u(z)), \\ &= (1 - Q(z))(P_n^{-1}(z)y(z) - u(z)), \end{aligned} \tag{2.19}$$

where Q is either (2.16), (2.17) or (2.18). To obtain the power spectral density (PSD) of the error, $d_{error}(z)$ is rewritten as

$$d_{error}(z)d_{error}^H(z) = (1 - Q(z))(P_n^{-1}(z)y(z) - u(z))d_{error}^H(z), \tag{2.20}$$

$$\tag{2.21}$$

where ^{H} indicates the Hermitian. The resulting cPSD-plot for setpoint speeds ranging from 1 to 6 rps is given in Fig. 2.9. For all speeds, ZMETC shows the lowest error at lower frequencies, approximately up to 200 Hz. ZMETC is therefore finally chosen for Q in (2.5).

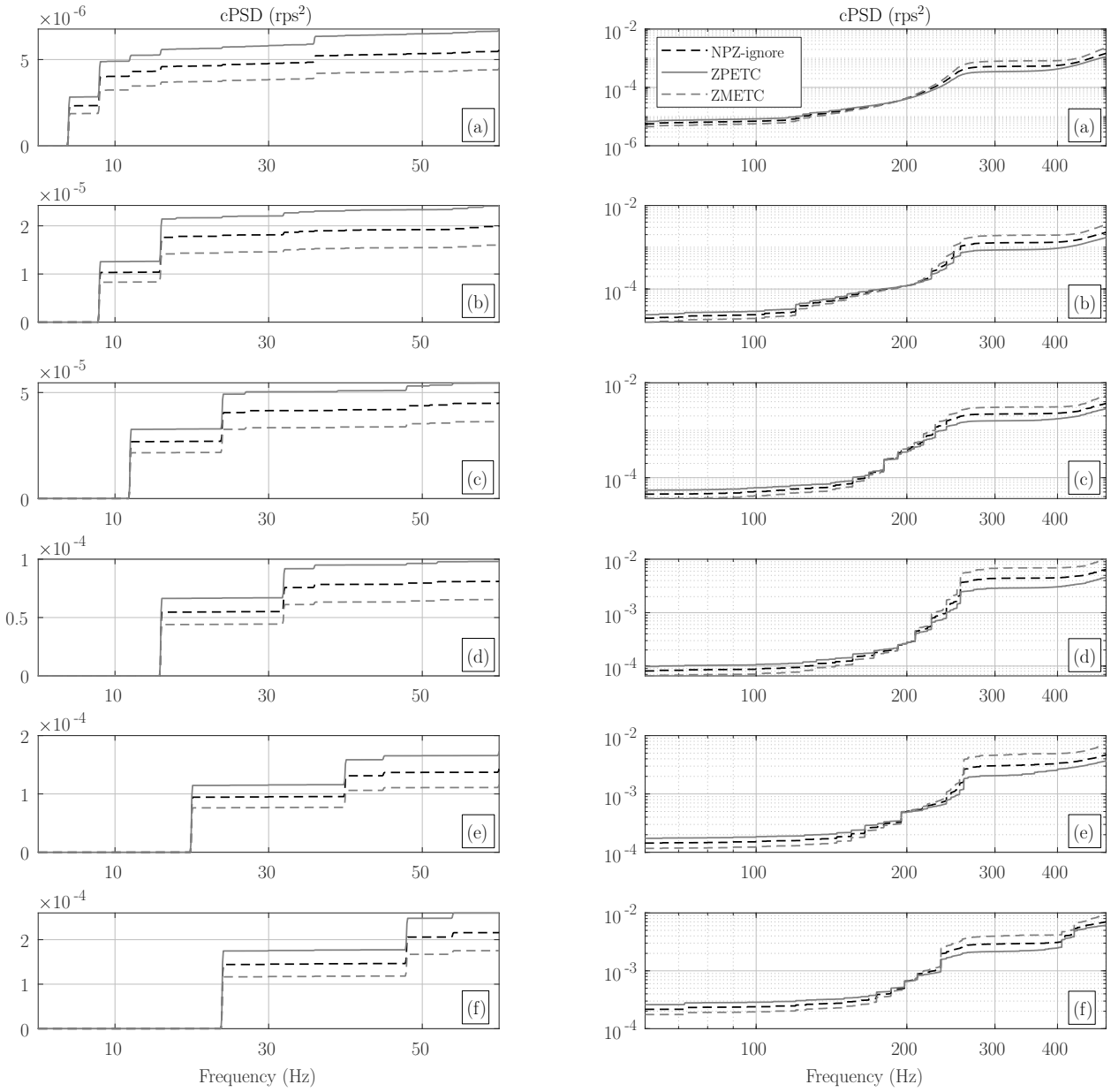

Figure 2.9: Cumulative power spectral density plot of the disturbance estimation error (2.20) with NPZ-ignore, ZPETC and ZMETC for setpoint speeds ranging from (a) 1; (b) 2; (c) 3; (d) 4; (e) 5; to (f) 6 rps represented (left column) on a linear scale from 0 to 60 Hz and (right column) on a logarithmic scale from 60 to 500 Hz.

Chapter 3

Hybrid integrator-gain-based control

3.1 Introduction

This chapter presents a HIGS-based PI2 controller design for the purpose of reducing the steady-state setpoint error of the motor speed of the peristaltic pump setup shown in Figure 2.1 compared to linear PI2 control while at least maintaining the same robustness margins. It first covers a conference paper in which a HIGS-based PI2 controller design is presented for the peristaltic pump (Section 3.2). Next, some extensions with respect to the paper are presented regarding HIGS-based integrator design (Section 3.3) and HIGS-based PI2 controller design (Section 3.4). The analyses are based on simulations, eventually proposing an improved HIGS-based PI2 controller design compared to the paper. Performance with the new HIGS-based PI2 controller is subsequently compared to the performance with the HIGS-based PI2 controller from the paper using simulations (Section 3.5), after which the performance with the new HIGS-based PI2 controller is also experimentally validated on the peristaltic pump setup shown in Figure 2.1 (Section 3.6), followed by a summary of the main conclusions from this chapter (Section 3.7).

3.2 Conference paper

The conference paper presented below is a first submission for the 2024 American Control Conference held in Toronto. Some content of the paper might overlap with other parts of this thesis. The main contributions of Thijs Tijman op Smeijers are Section II-B which describes the performance limitations of the linear controller, Section III-B which describes the HIGS-based controller architecture, design of the HIGS weighing filters and fine-tuning of the controller parameters, and Section IV which describes the implementation of the HIGS-based controller on the experimental setup including an in-depth analysis of the results. Michiel Beijen has initiated the idea of applying HIGS-based control to the peristaltic pump and has written the introduction (Section I) and the main conclusions (Section V). Gijs Boerrigter has written the modeling part in Section II-A and co-supervised Thijs together with Michiel during his graduation project. Sebastiaan van den Eijnden has written the theoretical backgrounds of HIGS in Section III-A and supported with embedding this specific contribution of HIGS-based control into the existing knowledge of HIGS-based control in literature.

Hybrid control of a variable-speed peristaltic pump

Michiel Beijen[1,2], Thijs Tijman op Smeijers[1,2], Gijs Boerrigter[2] and Sebastiaan van den Eijnden[3]

***Abstract*— Peristaltic pumps are used for transporting liquids within disposable tubes, and are commonly found in medical devices. The peristaltic pump principle, however, introduces disturbances, thereby distorting the desired rotational speed of the pump. Proportional plus double integral (PI2) control is commonly used to reject these disturbances, but at the cost of deteriorated transient response and robustness margins. To balance these trade-offs in a more desirable manner, in this paper we propose a hybrid PI2 control strategy that allows for reducing the steady-state error while maintaining robustness margins similar to linear PI2 control. Experiments on a representative setup demonstrate up to 45% improvement in disturbance rejection capabilities.**

I. Introduction

Peristaltic pumps are used for transport of liquids within plastic tubes. A rotating pump wheel with several rollers is placed against the tube, where the rollers "push" the flow forward [1]. Because there is no direct contact between the pump wheels and the fluid, there is no chance of fluid contamination. Therefore, typical applications of peristaltic pumps can be found in medical devices where fluid goes through disposable tubes [2], [3].

Due to the peristaltic pump principle, flow and pressure ripples occur in the fluid whose periodicity directly depends on the rotational speed of the pump and which distort this speed. Besides, effects such as non-perfect commutation of the brushless DC motor, friction and transient effects due to continuous setpoint variations further disturb the desired motor speed. For controlling the motor speed to a desired setpoint, classical linear methods such as PI(2)D control are typically used [3]. Linear control, however, suffers from fundamental trade-offs between performance and robustness properties [4], thereby limiting the extent to which pump ripples can be attenuated.

Several advanced control techniques have been considered to balance these trade-offs in a more desirable manner, and improve the rejection of pump speed disturbances. An attempt with fuzzy control has been considered in [3] but in the same work it was concluded that PID control outperformed the fuzzy controller. In [5], [6], [7], repetitive controllers are proposed which use sampling in the spatial domain to suppress periodic disturbances, and in [8] a repetitive controller with adaptation capabilities has been proposed. However, such repetitive controllers are only intended for specific disturbances and require a priori knowledge of the disturbance characteristics. Moreover, it takes time to let these controllers "learn" the optimal magnitude and phase characteristics of the compensating signal. A disturbance observer along with repetitive control has been proposed in [9], and a similar disturbance observer approach has been considered in [10] to reject periodic disturbances in brushless DC motors. In [2] an extended Kalman filter is applied to control the pressure in a medical device using an observer-based signal instead of a direct measurement. However, such observer-based methods also require assumptions on the underlying disturbance models which are not always easy to obtain, especially within an unpredictable environment.

An interesting development in the high-precision industry, where robustness and disturbance rejection also play a crucial role, is the use of hybrid integrator-gain systems (HIGS) within typical motion control architectures [11], [12]. HIGS can be exploited for constructing nonlinear filter elements that mimick the amplification characteristics of classical linear filters such as integrators and low-pass filters, but with reduced phase lag. From a design point-of-view, these HIGS-based filters provide additional freedom in controller tuning as gain and phase appear to be no longer related. This, in turn, allows for achieving higher bandwidths and improved disturbance rejection capabilities, without compromising transient performance and robustness margins [11].

So far, HIGS-based controllers have mainly been considered for control of high-precision motion systems that operate in predictable and contained environments [12], [13]. The main contribution of this paper is to demonstrate the feasibility of HIGS-based controllers on less predictable systems. Specifically, we aim to improve the performance of peristaltic pumps equipped with disposable tubes without using a priori knowledge of the disturbances. An intuitive replacement of an existing linear PI2 controller by its HIGS-based counterpart is proposed to improve the system bandwidth and broad-band disturbance rejection, while preserving the same transient performance and robustness margins as obtained with linear control. The performance gain of HIGS-based controllers is demonstrated experimentally on a representative peristaltic pump setup.

The remainder of this paper is organized as follows. Section II describes the application at hand and the currently implemented linear controller. HIGS-based controller design is discussed in Section III. The results of experimental validations are presented in Section IV, and the main conclusions

Part of the research leading to these results has received funding from the European Research Council under the Advanced ERC Grant Agreement PROACTHIS, no. 101055384.

[1]Department of Engineering Technology, Group of Precision Engineering, University of Twente, PO Box 217, 7500 AE Enschede, The Netherlands m.beijen@utwente.nl.

[2]Demcon high-tech systems, Institutenweg 25, 7521 PH Enschede, The Netherlands.

[3]Department of Mechanical Engineering, Control Systems Technology Group, Eindhoven University of Technology, PO Box 513, 5600 MB Eindhoven, The Netherlands.

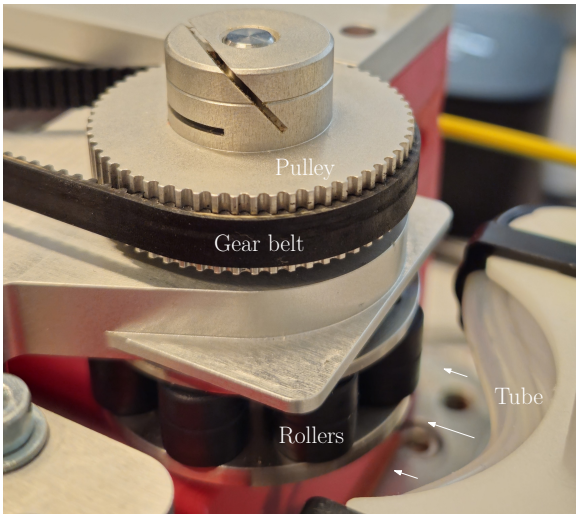

Fig. 1: Experimental setup of the peristaltic pump.

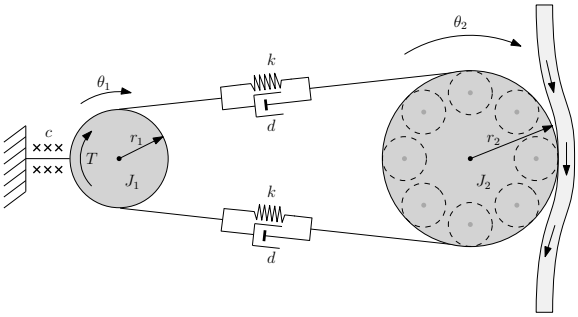

Fig. 2: Simplified model of the peristaltic pump.

are given in Section V.

II. Linear control of a peristaltic pump

In this section, we will introduce the peristaltic pump and derive a mathematical model of the system. Moreover, we will discuss the baseline linear control strategy for this application, and showcase some of the resulting trade-offs which motivate the use of a HIGS-based control strategy.

A. Mathematical model

The peristaltic pump considered in this paper is shown in Fig. 1 and consists of a pulley with eight rollers that are used to compress a tube that carries fluids. The pulley is driven by a gear belt that is connected to another pulley at the motor side. Typically, two to three rollers compress the tube simultaneously. The pump speed is measured indirectly by differentiating the signal coming from the encoder installed at the motor shaft.

A simplified model of the system is shown in Fig. 2. Here, $J_1 = 7.8 \cdot 10^{-6}$ kgm^2 denotes the combined inertia of the motor and small pulley with radius $r_1 = 8.2 \cdot 10^{-3}$ m. J_1 is connected to the fixed world by means of a rotational damper with damping constant $c = 4.5 \cdot 10^{-3}$ Nms/rad, representing viscous damping of the motor. The gear belt is modeled with translational stiffness $k = 6.8 \cdot 10^4$ N/m

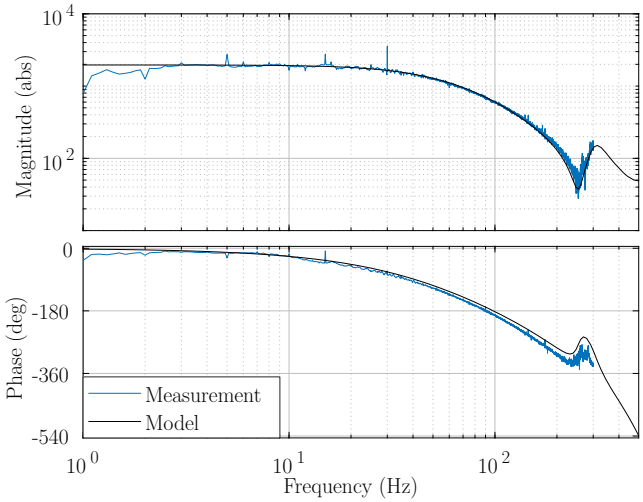

Fig. 3: Modeled and measured frequency response function from input voltage U to output motor speed $\dot{\theta}_1$.

and damping $d = 5$ Ns/m. The large pulley has inertia $J_2 = 15.5 \cdot 10^{-6}$ kgm^2 with radius $r_2 = 17 \cdot 10^{-3}$ m. The angular displacements of the small and large pulley are denoted by θ_1 and θ_2, respectively. A motor torque T is generated by voltage U, which will be used to accurately control the angular velocity of the small pulley, denoted by $\dot{\theta}_1$, to a desired speed $\dot{\theta}_r$. Using first-principles modeling, the relation between voltage U and angular velocity $\dot{\theta}_1$ is given by $\dot{\theta}_1(s) = P(s)U(s)$ with

$$P(s) = \frac{1}{2\pi} \frac{1}{J_{tot}s + c} \frac{\frac{1}{\omega_a^2}s^2 + 2\frac{\zeta_a}{\omega_a}s + 1}{\frac{1}{\omega_r^2}s^2 + 2\frac{\zeta_r}{\omega_r}s + 1} \frac{92}{100} \frac{\omega_{act}}{s + \omega_{act}} e^{-st_s}, \tag{1}$$

where $J_{tot} = J_1 + J_2(\frac{r_1}{r_2})^2 = 11.4 \cdot 10^{-6}$ kgm^2, $\omega_a = \sqrt{\frac{2kr_2^2}{J_2}} = 253 \cdot 2\pi$ rad/s, $\omega_r \approx \sqrt{\frac{2kr_1^2 J_{tot}}{J_1 J_2 (\frac{r_1}{r_2})^2}} = 306 \cdot 2\pi$ rad/s, $\zeta_a = 0.062$, $\zeta_r = 0.12$. Constant $\frac{1}{2\pi}$ is required rewrite $\dot{\theta}_1$ from rad/s to rotations per second (rps), whilst constant $\frac{92}{100}$ is required to rewrite torque T in Nm to voltage U in %-duty cycle V. Furthermore, $\omega_{act} = 80 \cdot 2\pi$ rad/s represents the induction pole of the voltage-controlled brushless DC-motor. One computational sample delay of $t_s = 0.001$ s is taken into account to match the behavior of the real-time platform. The plant model is discretized using the zero-order-hold method. A Bode plot of the modeled response from input voltage U to output motor speed $\dot{\theta}_1$ is shown in Fig. 3, along with a measured frequency response function. At lower frequencies, the plant behavior is characterized by the motor damping. At higher frequencies, the inertia line $\frac{1}{J_{tot}s}$ is visible with an internal anti-resonance and resonance caused by the gear belt. The model (1) provides valuable insights in the true system behavior and will be used for controller design in the next section.

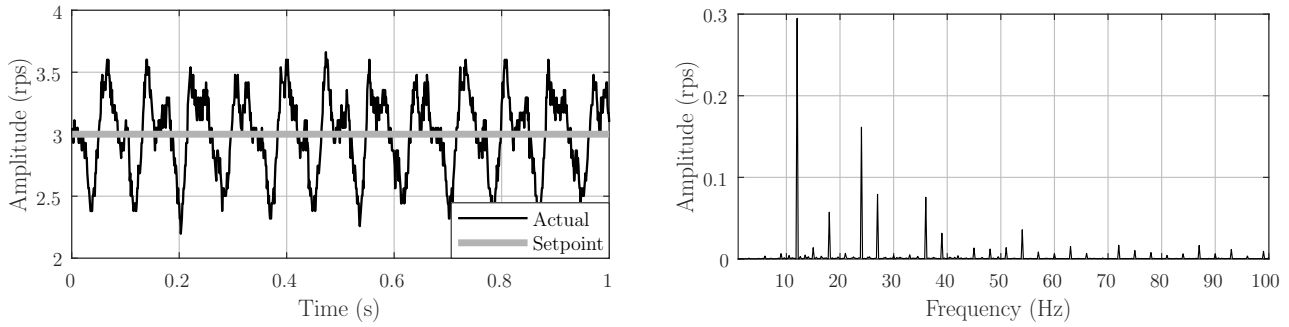

(a) (b)

Fig. 4: Typical pump speed measurement represented in the time domain (a) and in an amplitude spectrum (b) using the linear PI2 controller.

B. Linear control design and performance tradeoffs

The control objective considered in this paper is to reduce the steady-state setpoint error $e(t) = \dot{\theta}_1(t) - \dot{\theta}_r(t)$ using feedback control. We consider the following performance measures:

- Peak-to-peak value in the time domain, computed as $\max_t(e_i(t)) - \min_t(e_i(t))$, where e_i is the i^{th} sample of the setpoint error with $i \in [1, N]$, N the number of samples;
- Root-mean square value in the time domain, computed as $\sqrt{\frac{1}{N}\sum_{i=1}^{N}|e_i(t)|^2}$;
- Square-rooted cumulative power spectral density plot.

For achieving these performance objectives, we consider a linear PI2 controller C_{lin} as the baseline,

$$C_{lin}(s) = k_p\left(1 + \frac{\omega_1}{s}\right)\left(1 + \frac{\omega_2}{s}\right), \tag{2}$$

in which $k_p = 4 \cdot 10^{-4}$, $\omega_1 = 30 \cdot 2\pi$ rad/s and $\omega_2 = 10 \cdot 2\pi$ rad/s are tuned by means of classical loop-shaping techniques [14]. The corresponding open-loop, sensitivity and Nyquist characteristics are shown in Fig. 6–8. It is observed that this linear controller provides an open-loop cross-over frequency of 29.4 Hz with a sufficiently high modulus margin of 0.56.

Typically measured performance plots in both the time- and frequency-domain of the system with linear PI2 control are shown in Fig. 4. In the time-domain plot, a clear pump ripple is visible around the setpoint value of 3 rps. From the amplitude spectrum plot a dominant ripple at 12 Hz is visible, which is 4 times the setpoint value of 3 rps. The factor 4 follows from the fact that there are 8 pump wheels per rotation but there is a gear ratio of 2 between the two pulleys, hence the ratio 8/2=4. Besides, several other disturbing frequencies are present in the amplitude spectrum which might have different causes such as non-perfect motor commutation, friction, et cetera. Since there are so much disturbing frequencies, it is desired to improve the broadband disturbance rejection which is possible using HIGS-based control.

III. HIGS-BASED CONTROL OF A PERISTALTIC PUMP

To reduce the setpoint error, the HIGS-based PI2 controller design will be presented in this section.

A. HIGS description

In order to discuss our control design in detail, we start by formally introducing HIGS [15] as

$$\mathcal{H}: \begin{cases} \dot{x}_h &= \omega_h z, \text{ if } (z, u, \dot{z}) \in \mathcal{F}_1, \\ x_h &= k_h z, \text{ if } (z, u, \dot{z}) \in \mathcal{F}_2, \\ u &= x_h, \end{cases} \tag{3}$$

where $x_h \in \mathbb{R}$ denotes the integrator state, $z \in \mathbb{R}$ is the input to HIGS, $u \in \mathbb{R}$ is the generated output, and $\omega_h \in [0, \infty)$ the integrator frequency, and $k_h \in (0, \infty)$ the gain. In this paper, $k_h = 1$. The sets $\mathcal{F}_1$ and $\mathcal{F}_2$ dictate the active modes (integrator-mode, and gain-mode) of (3) and are given by

$$\mathcal{F}_1 = \left\{(z, u, \dot{z}) \in \mathbb{R}^3 \mid k_h z u \geq u^2 \wedge (z, u, \dot{z}) \notin \mathcal{F}_2\right\}, \tag{4a}$$
$$\mathcal{F}_2 = \left\{(z, u, \dot{z}) \in \mathbb{R}^3 \mid u = k_h z \wedge \omega_h z^2 > \dot{z} z\right\} \tag{4b}$$

for which the union defines the "$[0, k_h]$-sector"

$$\mathcal{F} := \mathcal{F}_1 \cup \mathcal{F}_2 = \left\{(z, u, \dot{z}) \in \mathbb{R}^3 \mid k_h z u \geq u^2\right\}. \tag{5}$$

The rationale underlying the formulation (3), (4) is as follows. In its preferred mode of operation, HIGS follows linear integrator dynamics. The integrator dynamics, however, can only be used for as long as the input–output pair (z, u) of $\mathcal{H}$ remains inside the sector $\mathcal{F}$ in (5). In this way, the signs of the integrator's input z and its output u are forced to be equivalent at all times. At moments when the input–output pair (z, u) of $\mathcal{H}$ tends to leave the sector $\mathcal{F}$, a switch to the so-called gain-mode is made to ensure $(z, u) \in \mathcal{F}$. In gain-mode, HIGS can only return to integrator-mode if the vector field following the integrator dynamics points toward the interior of $\mathcal{F}$. This is governed by the condition $\omega_h z^2 > \dot{z} z$ in (4b). A typical response of HIGS to a sinusoidal input $z(t) = \sin(\omega t)$ is shown in Fig. 5. When compared to the response of an LTI integrator to the same input, it can be seen that the amplification properties with HIGS are roughly the same, whereas the phase lag appears to be reduced.

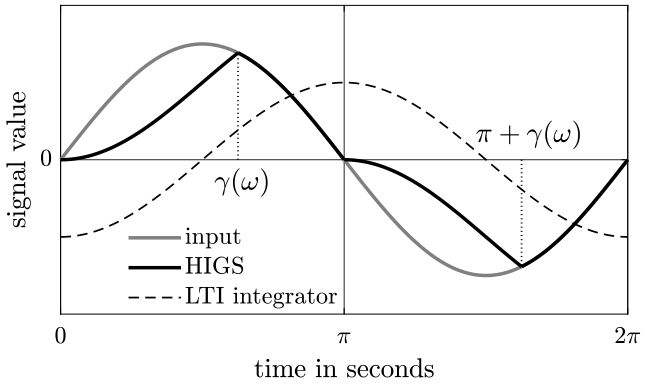

Fig. 5: Time response of HIGS in (3) (solid black) to a sinusoidal input along with the response of an LTI integrator (dashed).

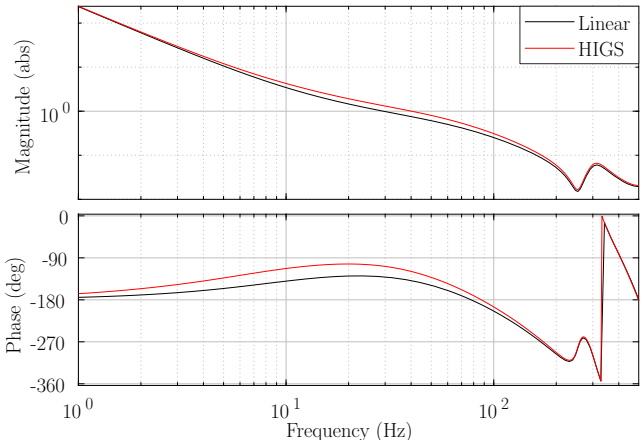

Fig. 6: Bode diagram of the open loop with linear (black) and HIGS-based control (red).

This alleged "phase" advantage can be made more intuitive through conducting a describing function analysis, that is, by finding the complex mapping from a sinusoidal input $z(t) = \sin(\omega t)$ to (3) to the fundamental harmonic in the corresponding output $u(t)$ as depicted in Fig. 5. The describing function of HIGS is given by [11]

$$\mathcal{D}(j\omega) = \frac{\omega_h}{j\omega}\left(\frac{\gamma}{\pi} + j\frac{e^{-2j\gamma}-1}{2\pi} - 4j\frac{e^{-j\gamma}-1}{2\pi}\right) + \left(\frac{\pi-\gamma}{\pi} + j\frac{e^{-2j\gamma}-1}{2\pi}\right), \tag{6}$$

with $\gamma = 2\arctan\left(\frac{\omega}{\omega_h}\right) \in [0, \pi]$ the periodic switching instance between integrator-mode and gain-mode, see also Fig. 5. The describing function (6) reveals (weak) integrator characteristics, with an induced phase lag of at most 38.15 degrees. The latter is a significant reduction as compared to the 90 degrees typically induced by an LTI integrator.

B. HIGS-based PI2 controller architecture

Equipped with the definition of the HIGS element $\mathcal{H}$ in (3) and its describing function $\mathcal{D}$ in (6), the HIGS-based PI2 controller design is provided in this section. For this purpose, we first construct a HIGS-based integrator $I\{\mathcal{H}\}$ as follows. Perform a pre- and post-multiplication of $\mathcal{H}$ with linear filters

$$L_1(s) := V(s)\left(\frac{s}{\omega_c} + 1\right), \quad \text{and} \quad L_2(s) := \frac{1}{s}V^{-1}(s),$$

where $\omega_c := \omega_h\,|1 + 4j/\pi|$, such that

$$I\{\mathcal{H}\} := L_1 \cdot \mathcal{H} \cdot L_2. \tag{7}$$

The design philosophy for the HIGS-based integrator (7) stems from describing function analysis. That is, a describing function for the HIGS-based integrator is given by $\mathcal{I}(j\omega) := L_1(j\omega)\mathcal{D}(j\omega)L_2(j\omega)$, which yields the precise magnitude characteristic of a classical integrator, but with (locally) reduced phase lag. This phase benefit will be the key mechanism for both bandwidth and transient performance improvements. The filter $V(s)$ in $L_1(s)$ is a weighting filter that is added for the purpose of conditioning the input signals to HIGS, whereas its inverse $V^{-1}(s)$ is added in $L_2(s)$ for keeping the describing function, and with that the loop-gain, unaffected. In our design, we choose $V(s)$ to be a second-order lag filter of the form

$$V(s) = \frac{\omega_p^2}{\omega_z^2}\frac{(s+\omega_z)^2}{(s+\omega_p)^2}, \tag{8}$$

with $\omega_z = 5000$ rad/s and $\omega_p = 500$ rad/s. This design choice stems form the observation that quantization effects in the measured error signals may induce high-frequent switching of HIGS, thereby inducing *gain-loss* [13].

Note that due to the simple integrator in $L_2(s)$ we introduce an additional state, which acts as a buffer in $I\{\mathcal{H}\}$ and ensures that, similar to an LTI integrator, our HIGS-based integrator is capable of sustaining a DC output.

With the design of a HIGS-based integrator in place, a HIGS-based PI2 controller is constructed by replacing the linear integrators in (2) with their HIGS-based counterparts (7), that is

$$C_{HIGS}\{\mathcal{H}\} = k_p\,(1 + \omega_1 I_1\{\mathcal{H}\})\,(1 + \omega_2 I_2\{\mathcal{H}\})\,. \tag{9}$$

Here, $k_p = 4 \cdot 10^{-4}$, $\omega_1 = 30 \cdot 2\pi$ rad/s and $\omega_2 = 10 \cdot 2\pi$ rad/s are chosen to match the linear controller design. A frequency-domain approximation of $C_{HIGS}\{\mathcal{H}\}$ is given by

$$\mathcal{C}_{HIGS}(j\omega) = k_p\big(1 + \omega_1\mathcal{I}_i(j\omega)\big)\big(1 + \omega_2\mathcal{I}_i(j\omega)\big), \tag{10}$$

where $\mathcal{I}_i(j\omega)$, $i = \{1, 2\}$ are the describing functions of the individual HIGS-based integrators. In our design, we choose the values for $\omega_{h,i} = \alpha\omega_i$, $i = \{1, 2\}$. The factor α can be used to let the behavior of the HIGS controller tend toward that of a Clegg integrator ($\alpha \to 0$) or a linear integrator ($\alpha \to \infty$) [13]. In this paper, the value $\alpha = 0.5$ is found as a good trade-off.

The open-loop, sensitivity and Nyquist characteristics of both linear and HIGS-based controller designs are shown in Fig. 6–8. Note that for the HIGS design, the frequency-domain characteristics are plotted using the describing function approximation in (10) which are quasi-linear approximations of the non-linear HIGS elements. Therefore, these

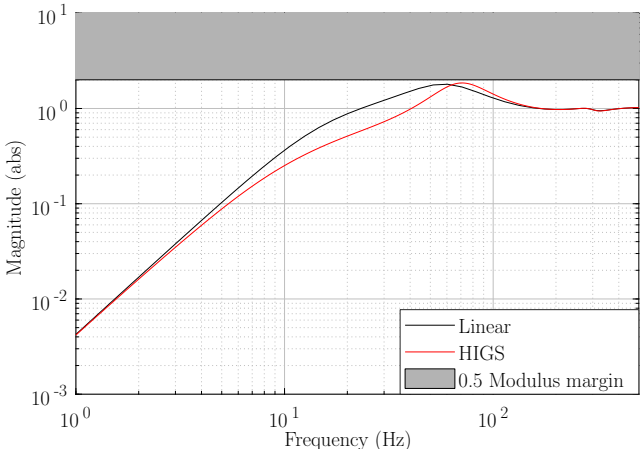

Fig. 7: Bode magnitude diagram of the sensitivity function with linear (black) and HIGS-based control (red), along with the 0.5 modulus margin (grey).

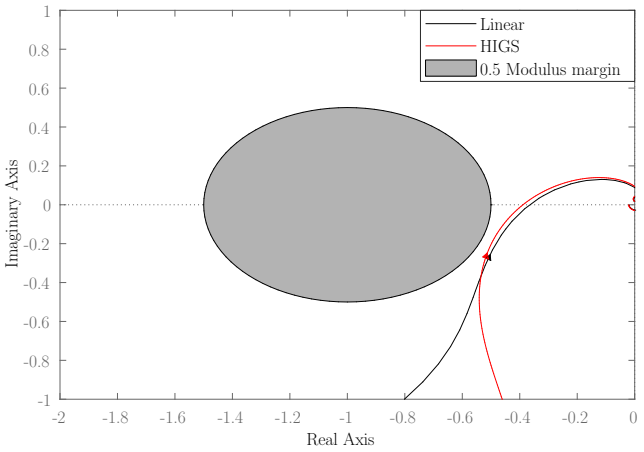

Fig. 8: Nyquist diagram of the open loop with linear (black) and HIGS-based control (red), along with a modulus margin of 0.5, showing only positive frequencies.

plots do not give an exact representation of stability and performance such as known for linear systems, but based on experiences from earlier work it is known that these plots give at least a good indication and therefore they will be used to assess performance and stability.

The open-loop Bode plot is shown in Fig. 6, demonstrating clear advantages of the HIGS-based control approach. There is a phase advantage over a broad frequency range while at the same time the cross-over frequency has been increased from 29.4 Hz to 40.2 Hz. Note that the increase in magnitude results from summing complex numbers where both the real and imaginary parts are nonzero in (10) as compared to the summation of orthogonal complex numbers in (2).

Fig. 7 shows a Bode magnitude diagram of the sensitivity function with linear and HIGS-based control, indicating improved disturbance rejection properties of the HIGS-based approach up to 64 Hz thanks to the increased cross-over frequency in the open-loop plot from Fig. 6.

TABLE I: P2P values of the setpoint error with HIGS-based control and linear control for setpoint speeds ranging from 1 to 6 rps. Improvement is calculated using $\frac{\text{P2P linear}-\text{P2P HIGS}}{\text{P2P linear}} \cdot 100\%$.

Setpoint	(rps)	1	2	3	4	5	6
P2P linear	(rps)	0.671	1.099	1.587	1.892	2.380	2.625
P2P HIGS	(rps)	0.671	0.977	1.221	1.465	1.648	1.831
Improvement	(%)	0	11	23	23	31	30

TABLE II: RMS values of the setpoint error with HIGS-based control and linear control for setpoint speeds ranging from 1 to 6 rps. Improvement is calculated using $\frac{\text{RMS linear}-\text{RMS HIGS}}{\text{RMS linear}} \cdot 100\%$.

Setpoint	(rps)	1	2	3	4	5	6
RMS linear	(rps)	0.090	0.192	0.322	0.451	0.568	0.662
RMS HIGS	(rps)	0.110	0.185	0.214	0.259	0.314	0.361
Improvement	(%)	-22	4	34	43	45	45

The Nyquist diagram of the open loops are shown in Fig. 8. Both open loops remain to the right of the point -1 along the trajectory, implying that the closed-loop is stable according to the Nyquist stability criterion [14]. Additionally, the 6 dB modulus margin is plotted, indicating that both the linear and HIGS-based open loop have sufficient modulus margin to ensure robust stability, with a similar value.

IV. Experimental validation

In this section we compare performance of the linear and HIGS-based control strategies on the peristaltic pump setup discussed in Section II. During the experiments, the system is subject to six different angular velocity setpoints. For each setpoint, steady-state measurements of 90 seconds are conducted using either linear or HIGS-based control. The measured velocity is used to quantify the peak-to-peak (P2P) and root-mean-square (RMS) values which are defined as performance measures in Section II. The results are summarized quantitatively in Table I, Table II and Fig. 9.

Small fragments of 0.5 s of the measured pump speed with linear (black) and HIGS-based control (red) are shown in the left column in Fig. 9. Both the time-domain plots in Fig. 9 as well as the P2P values in Table I show that for lower pump speeds the performance of both controllers is comparable whereas for higher pump speeds the HIGS-based controller outperforms the linear controller. This observation is in line with the expectations coming from the (approximate) sensitivity plots in Fig. 7. From this plot, the largest performance improvement is expected in the range from $10-40$ Hz, which corresponds to higher pump speeds (recall from Section II that a dominant disturbance frequency can be expected at four times the rps setpoint, i.e., 4 Hz at 1 rps and 8 Hz at 2 rps, and so on). At higher pump speeds the P2P values indicate a performance improvement up to 31%.

A frequency-domain analysis in terms of the square-rooted cumulative power spectral density ($\sqrt{\text{cPSD}}$) is shown in the right column of Fig. 9. As expected, the largest harmonic contribution to the setpoint error is the base frequency (4

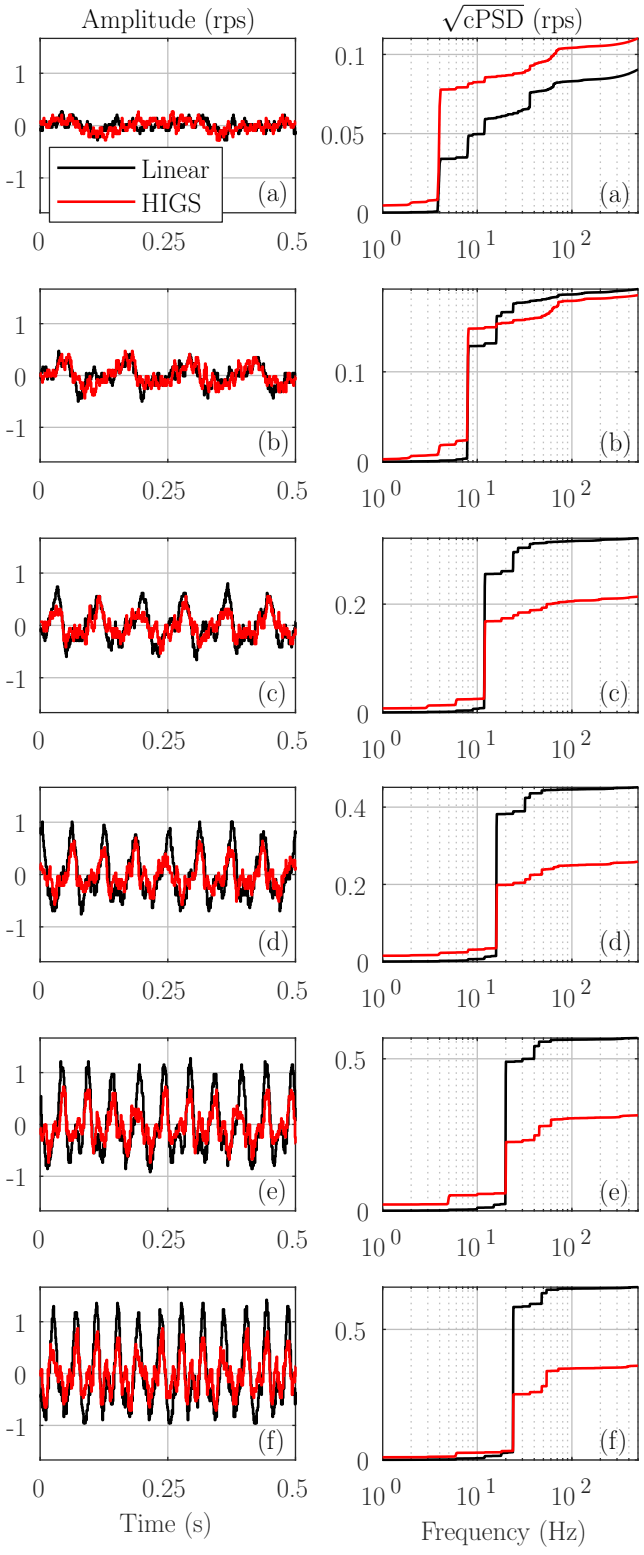

Fig. 9: (left) Steady-state time domain measurements and (right) square-rooted cumulative power spectral density representation of the setpoint error with linear (black) and HIGS-based control (red) for setpoint speeds ranging from (a) 1; (b) 2; (c) 3; (d) 4; (e) 5; (f) 6 rps.

times the rps setpoint) of the pump ripple. The values at the Nyquist frequency (500 Hz) indicate the RMS values of the setpoint error, for which the exact values are also listed in Table II. At a motor speed of 1 rps, corresponding to a dominant disturbance of 4 Hz, there appears to be a deterioration in terms of RMS values. This seems to be attributed to the gain-loss phenomenon and the generation of higher-harmonic content in HIGS [11]. At higher input velocities, there is a significant improvement in RMS values up to 45% with HIGS-based control, indicating the performance benefits of this strategy.

V. Conclusions

In this paper, we have applied a HIGS-based PI2 control strategy to a variable-speed peristaltic pump for the purpose of reducing the setpoint error of the pump speed. Performance of the hybrid control strategy is experimentally validated and compared to that of the linear PI2 controller. The measurement results demonstrate up to a significant 45% improvement in disturbance rejection, expressed in terms of peak-to-peak and root-mean-square values of the setpoint error. Future work includes formal stability and performance assessment of the closed-loop controlled system, as well as extended tuning guidelines to further exploit the additional design freedom of HIGS-based controllers.

References

[1] J. Klespitz and L. Kovács, "Peristaltic pumps—a review on working and control possibilities," in *2014 IEEE 12th International Symposium on Applied Machine Intelligence and Informatics (SAMI)*. IEEE, 2014, pp. 191–194.

[2] E. Smolinski, A. Benkmann, W. Drewelow, T. Jeinsch, and H.-J. Cappius, "Observer-based controller design for the minimally invasive surgery," *Current Directions in Biomedical Engineering*, vol. 4, no. 1, pp. 41–44, 2018.

[3] J. Klespitz and L. Kovács, "Identification and control of peristaltic pumps in hemodialysis machines," in *2013 IEEE 14th International Symposium on Computational Intelligence and Informatics (CINTI)*. IEEE, 2013, pp. 83–87.

[4] J. Freudenberg and D. Looze, "Right half plane poles and zeros and design tradeoffs in feedback systems," *IEEE transactions on automatic control*, vol. 30, no. 6, pp. 555–565, 1985.

[5] G. Hillerstrom and J. Sternby, "Application of repetitive control to a peristaltic pump," in *1993 American Control Conference*. IEEE, 1993, pp. 136–141.

[6] G. Ramos, J. Cortés-Romero, and H. Coral-Enriquez, "Spatial observer-based repetitive controller: An active disturbance rejection approach," *Control Engineering Practice*, vol. 42, pp. 1–11, 2015.

[7] N. Mooren, G. Witvoet, and T. Oomen, "Gaussian process repetitive control for suppressing spatial disturbances," *IFAC-PapersOnLine*, vol. 53, no. 2, pp. 1487–1492, 2020.

[8] M. Tomizuka, "Dealing with periodic disturbances in controls of mechanical systems," *Annual Reviews in Control*, vol. 32, no. 2, pp. 193–199, 2008.

[9] N. Dey, U. Mondal, and A. Sengupta, "Modified repetitive controller for disturbance rejection of peristaltic pump," in *2019 International Conference on Opto-Electronics and Applied Optics (Optronix)*. IEEE, 2019, pp. 1–5.

[10] R. C. L. Chuei, "Robust disturbance observer-based repetitive control for brushless dc motors," Ph.D. dissertation, Swinburne University of Technology Melbourne, Australia, 2023.

[11] M. F. Heertjes, S. J. A. M. van den Eijnden, and B. Sharif, "An overview on hybrid integrator-gain systems with applications to wafer scanners," in *2023 IEEE International Conference on Mechatronics (ICM)*, 2023, pp. 1–8.

[12] L. F. van Eijk, S. Beer, R. M. J. van Es, D. Kostić, and H. Nijmeijer, "Frequency-domain properties of the hybrid integrator-gain system and its application as a nonlinear lag filter," *IEEE Transactions on Control Systems Technology*, vol. 31, no. 2, pp. 905–912, 2023.

[13] M. F. Heertjes, S. J. A. M. van den Eijnden, W. P. M. H. Heemels, and H. Nijmeijer, "A solution to gain loss in hybrid integrator-gain systems," in *2021 IEEE Conference on Control Technology and Applications (CCTA)*. IEEE, aug 2021.

[14] S. Skogestad and I. Postlethwaite, *Multivariable feedback control: analysis and design*. John Wiley & sons, 2005.

[15] S. J. A. M. van den Eijnden, M. F. Heertjes, W. P. M. H. Heemels, and H. Nijmeijer, "Hybrid integrator-gain systems: A remedy for overshoot limitations in linear control?" *IEEE Control Systems Letters*, vol. 4, no. 4, pp. 1042–1047, oct 2020.

3.3 HIGS-based integrator designs

In this section, two different HIGS-based integrator designs are presented and analyzed. The designs are identical when approximated in the frequency domain, but result in different behavior when evaluated in the time domain. An examination of tuning parameter ω_h is conducted for each HIGS-based integrator design in both domains. Additionally, an analysis on the utilization of so-called gain loss filters is performed, which are linear time-invariant (LTI) shaping filters used to reduce the effect of gain loss [11] within the HIGS-based integrators. The complete analysis performed in this section provides additional insights compared to the paper (Section 3.2), enabling a structured design approach for HIGS-based PI2 controller design in Section 3.4.

3.3.1 Configuration

As introduced in the paper (Section 3.2), the design philosophy for the HIGS-based integrator stems from describing function analysis [9]. That is, the first-order describing function of HIGS (given in (6) in the paper) shows first-order low-pass magnitude characteristics, such that it should be appended with a PI filter with its zero identical to the crossover frequency of the first-order describing function of HIGS to obtain magnitude characteristics of a linear integrator. The PI filter can be split into a PD filter and linear integrator, given by

$$V(s) = 1 + \frac{s}{\omega_c}, \quad \text{and} \quad W(s) = \frac{1}{s}, \tag{3.1}$$

respectively, where ω_c represents the crossover frequency of the first-order describing function of the HIGS, given by $\omega_c := \omega_h \, |1 + 4j/\pi|$. The use of V here should not be confused with the use of V in the paper, where it represented a gain loss filter. Performing this split and putting PD filter V in front of the HIGS is expected to give improved transient performance, similar as found in [18]. However, examples where PD filter V is located behind the HIGS also exist [10], whilst no reasons not to locate it behind the HIGS are known yet. Therefore, in this thesis, both locations for PD filter V are considered. On the other hand, the location of linear integrator W is always behind HIGS. HIGS itself cannot maintain a buffer (zero input gives zero output), but the linear integrator can. By placing the linear integrator behind HIGS, the HIGS functions as a filling/depletion mechanism of the linear integrator [18].

The two considered HIGS-based integrator designs in this thesis are therefore given by

$$I_1\{\mathcal{H}\} = V \cdot \mathcal{H} \cdot W, \quad \text{and} \quad I_2\{\mathcal{H}\} = \mathcal{H} \cdot VW, \tag{3.2}$$

where $\mathcal{H}$ refers to the switched differential-algebraic equations describing HIGS (given in (3) in the paper) and the dot indicates that the order between filters is important. With I_2, the order between linear filters V and W is thus irrelevant. Despite resulting in different behavior in the time domain, both HIGS-based integrator configurations are identical when approximated in the frequency domain, and are given by

$$\mathcal{I}(j\omega) = V(j\omega)\mathcal{D}(j\omega)W(j\omega), \tag{3.3}$$

where $\mathcal{D}$ represents the first-order describing function of HIGS (given in (6) in the paper).

3.3.2 Tuning parameter ω_h

Integrator frequency ω_h is the tuning parameter for HIGS (gain k_h is always set to 1). The value for ω_h determines the location of the crossover frequency of the HIGS (ω_c in the paper) and therefore also from which frequency onward the phase lead of the HIGS-based integrator starts. Choosing ω_h relatively small increases the phase advantages of the HIGS, enabling the largest bandwidths and/or best disturbance rejection performance. This is illustrated in the Bode diagram in Figure 3.1, where HIGS-based integrator (3.3) is plotted for different values of ω_h, being 5, 0.5 and 0.1 Hz. The larger ω_h, the more the HIGS-based integrator resembles a linear integrator, whereas the smaller ω_h, the more it resembles a Clegg integrator [19].

However, when analyzing the HIGS-based integrator designs (3.2) in the time domain, disadvantages of a small ω_h arise. In contrast to LTI systems, with HIGS, a single-frequency input signal typically induces a response that contains, in addition to the excitation frequency, harmonic content at multiple other frequencies (higher harmonics). This is illustrated in Figure 3.2, where both HIGS-based integrator configurations (3.2) are subjected to a single harmonic input of the form $z(t) = \sin(2\pi t)$ for different values of ω_h, again being 5, 0.5 and 0.1 Hz. The smaller the value for ω_h, the larger the relative power content of the higher harmonics. When comparing both HIGS-based integrators, one can observe that I_2 contains relatively more power

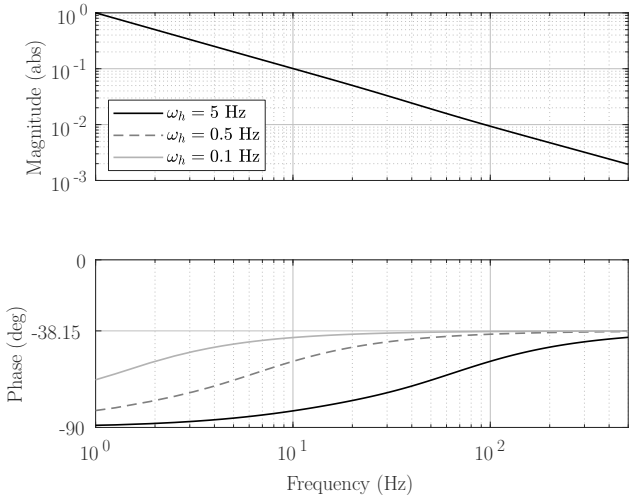

Figure 3.1: Bode diagram of the HIGS-based integrator (3.3) with $k_h = 1$ and (a) $\omega_h = 5$ Hz; (b) $\omega_h = 0.5$ Hz; (c) $\omega_h = 0.1$ Hz.

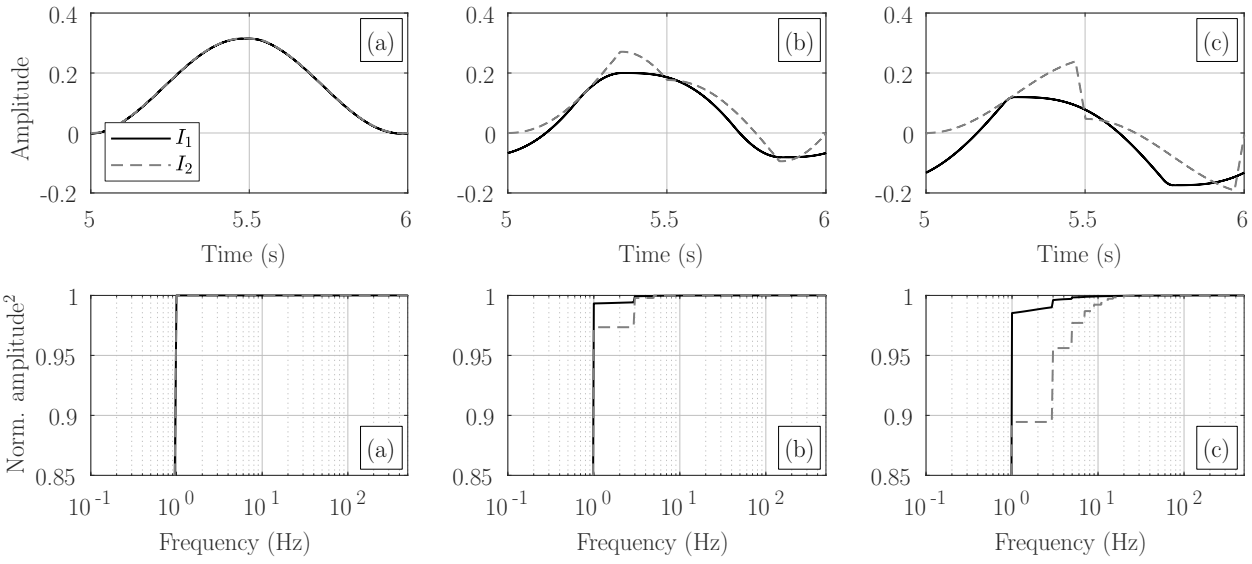

Figure 3.2: HIGS-based integrator I_1 and I_2 (3.2) subjected to input $z = \sin(2\pi t)$, with $k_h = 1$ and (a) $\omega_h = 5$ Hz; (b) $\omega_h = 0.5$ Hz; (c) $\omega_h = 0.1$ Hz, presented (top-row) in a time domain plot and (bottom-row) in a normalized cumulative power spectral density plot.

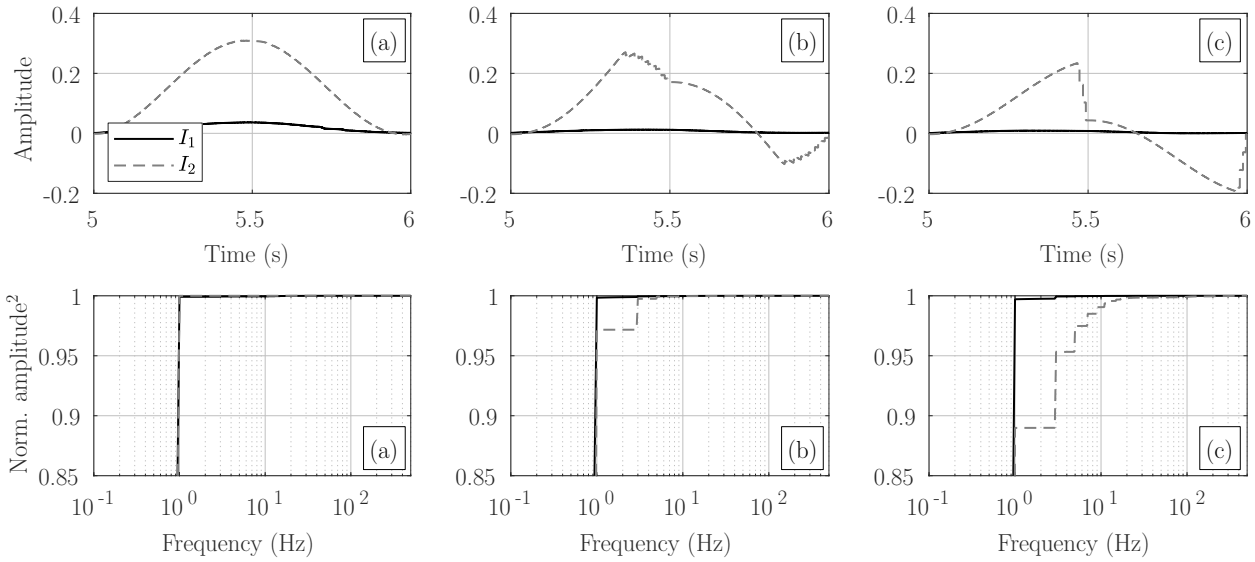

Figure 3.3: HIGS-based integrator I_1 (3.2) subjected to quantized input $z(t) = \sin(2\pi t)$, with $k_h = 1$ and (a) $\omega_h = 5$ Hz; (b) $\omega_h = 0.5$ Hz; (c) $\omega_h = 0.1$ Hz, presented (top-row) in a time domain plot and (bottom-row) in a normalized cumulative spectral density plot.

content at higher harmonics compared to I_1, and although not indicated by the figure, this is also the case in absolute terms. This is a result of the fact that for I_2 the generated higher harmonics by the HIGS are amplified by PD filter V, whereas for I_1 this is not the case as amplification by PD filter V occurs in front of HIGS. It is expected that the increased power of higher harmonic content results in worse performance. Based on these observations, I_1 seems more suited for HIGS-based controller design than I_2.

However, depending on the application, I_1 has other disadvantages. The peristaltic pump setup shown in Figure 2.1 experiences a quantization effect due to the finite resolution of the encoder (Section 2.2). To evaluate the effect of this quantization on the switching behavior of the HIGS-based integrators, input $z(t) = \sin(2\pi t)$ is subjected to this quantization effect, resulting in the response shown in Figure 3.3. For I_2, the output with quantization is similar to the output without quantization in Figure 3.2, whereas with I_1, this is not the case. This is a typical result of an effect called *gain loss* [11], which states that the presence of parasitic higher frequency components in the input of the HIGS can cause the HIGS to switch very frequently between integrator and gain mode, such that the integrator mode cannot build up sufficient gain for lower frequency components in the input. Quantization frequencies are generally present at higher frequencies compared to the input frequency. With I_1, PD filter V in front of the HIGS amplifies these higher frequency contributions, such that their amplitude becomes larger relative to the lower frequency contribution(s), resulting in gain loss. Additionally, a lower value for ω_h shifts the zero of PD filter V to a lower frequency, increasing the amplification of higher frequency contributions in the input of the HIGS and thereby possibly further increasing the amount of gain loss.

Where I_2 suffers from the amplification of generated higher harmonics, I_1 suffers (more) from gain loss. However, gain loss is a nonlinear phenomenon that occurs at the input side of HIGS, such that when shaping the input of HIGS with additional LTI filters, one could reduce or remove the effect of gain loss. Additionally shaping the output of HIGS with LTI filters could ensure the loop gain remains unaffected. In contrast, the amplification of generated higher harmonics with I_2 is a nonlinear phenomenon that occurs at the output side of the HIGS. Its effect could be reduced or removed by shaping the output of HIGS, but this alters the loop gain and is therefore undesired. The amplification of higher harmonics with I_2 is thus inevitable, whereas the gain loss with I_1 can be reduced or removed by shaping the HIGS with additional LTI filters. There are however disadvantages to latter approach as well, as elaborated on in Section 3.3.3. Note that depending on the input signals of the HIGS, I_2 might experience gain loss as well (Section 3.4.4), but this is generally significantly less severe than with I_1. Concluding, I_1 and I_2 each possess different advantages and disadvantages, such that both remain plausible choices for HIGS-based controller design.

3.3.3 Gain loss filters

The effect of gain loss can be reduced or removed by appending the HIGS with additional LTI shaping filters, referred to as gain loss filters. The sole purpose of these filters is to ensure that HIGS switches based on the desired (lower) frequency content, such that the output of HIGS is unaffected by parasitic higher frequency

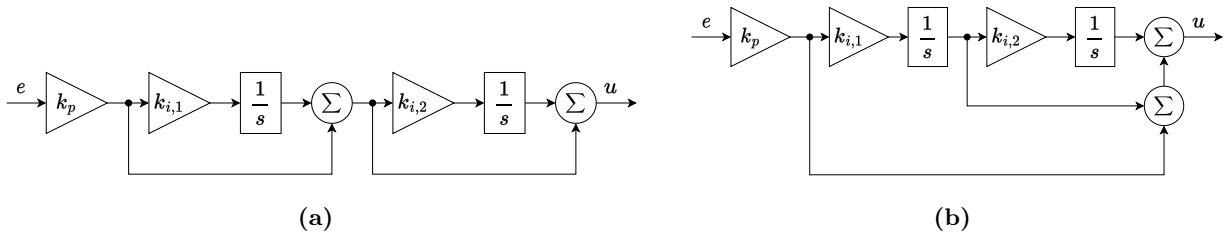

Figure 3.4: Controller with proportional double integrator action (a) in series configuration and (b) in parallel configuration.

components. Typical choices for gain loss filter are a low-pass, lag, (skew) notch or band-pass filter [11]. Which type to use is application-dependent. Regarding the example in Figure 3.3, a perfect gain loss filter would ensure that irrespective of the quantization effect, HIGS-based integrator I_1 generates a similar output as shown in Figure 3.2.

Gain loss filters are implemented as follows. The idea is to shape the input towards HIGS favourably, whilst the total loop gain is kept identical, such that (robust) stability properties based on frequency domain approximations remain unaffected. This can be realized by pre-filtering the HIGS with some LTI filter that reduces the amplitude of higher frequency content, and post-filtering with the inverse of this LTI filter. For this, the HIGS-based integrator designs (3.2) should be adjusted to

$$I_1\{\mathcal{H}\} = C_{gl}V \cdot \mathcal{H} \cdot WC_{gl}^{-1}, \quad \text{and} \quad I_2\{\mathcal{H}\} = C_{gl} \cdot \mathcal{H} \cdot VWC_{gl}^{-1}, \tag{3.4}$$

where C_{gl} represents the gain loss filter. Note that despite the example in Figure 3.3 shows hardly any gain loss with I_2, there could be situations where I_2 shows more gain loss and a gain loss filter is favourable.

There are however trade-offs in the design and the use of a gain loss filter as well. A general downside of the use of a gain loss filter is that post-filtering the HIGS with the inverse of the gain loss filter amplifies higher harmonic content generated by the HIGS, possibly affecting performance. A downside in the design of the gain loss filter is that the effectiveness of the filter depends on the parasitic high-frequency content in the input towards HIGS. If the parasitic high-frequency content differs per use case, finding a single suitable gain loss filter might be challenging. In Section 3.4.4, it is evaluated for different HIGS-based PI2 controller designs whether gain loss filters are favourable.

3.4 HIGS-based PI2 controller design

Equipped with the two HIGS-based integrator designs and the corresponding design considerations (Section 3.3), this section presents an improved HIGS-based PI2 controller design compared to the paper. First, a baseline linear PI2 controller configuration is chosen, which differs from the one used in the paper (Section 3.2). Then, eight different HIGS-based PI2 controller configurations are presented, which are designed by replacing one or both of the linear integrators with either of the HIGS-based integrators designs (3.2). A gain loss filter design is subsequently presented, which could be used for both HIGS-based integrator designs within any of the eight HIGS-based PI2 controllers. Then, a structured tuning methodology for HIGS-based PI2 controllers is provided, after which an optimal HIGS-based PI2 controller design is presented and its performance is compared to the HIGS-based PI2 controller from the paper and subsequently experimentally validated on the peristaltic pump setup shown in Figure 2.1.

3.4.1 Controller configurations

In contrast to the paper (Section 3.2), a different baseline configuration is chosen. The paper considers a series configuration of two PI filter blocks (Figure 3.4a), whereas from now on a parallel configuration is considered (Figure 3.4b). The corresponding newly designed baseline linear PI2 controller is given by

$$C_{lin}(s) = k_p\left(1 + \frac{k_{i,1}}{s} + \frac{k_{i,1}k_{i,2}}{s^2}\right), \tag{3.5}$$

with $k_p = 0.033$, $k_{i,1} = 60\pi$ and $k_{i,2} = 20\pi$, realizing a modulus margin (MM) of 0.51. An analysis on how these values were obtained can be found in the appendix in Section 3.8. The HIGS-based PI2 controllers are subsequently designed by keeping the values for $k_{i,1}$ and $k_{i,2}$ identical ($k_{i,1} = 60\pi$ and $k_{i,2} = 20\pi$), but by adjusting the value for k_p to realize a MM of 0.51 for each design. More on this can be found in Section 3.4.3. Figure 3.5 shows a Bode diagram of the open loop with the new parallel linear PI2 controller design

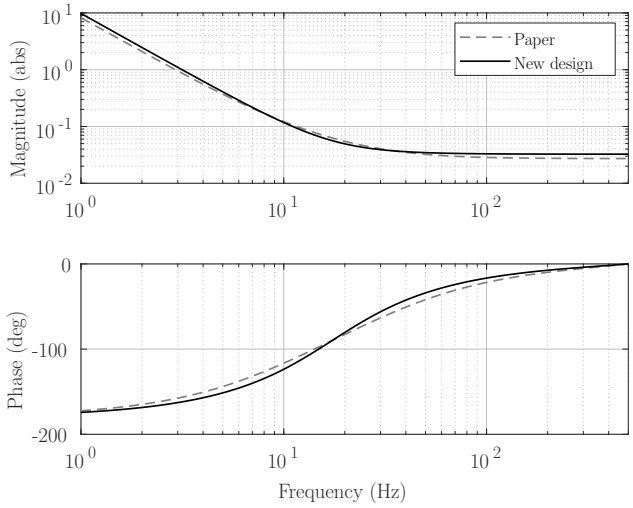

Figure 3.5: Bode diagram of the linear PI2 controller design in series configuration (paper) and in parallel configuration (new design).

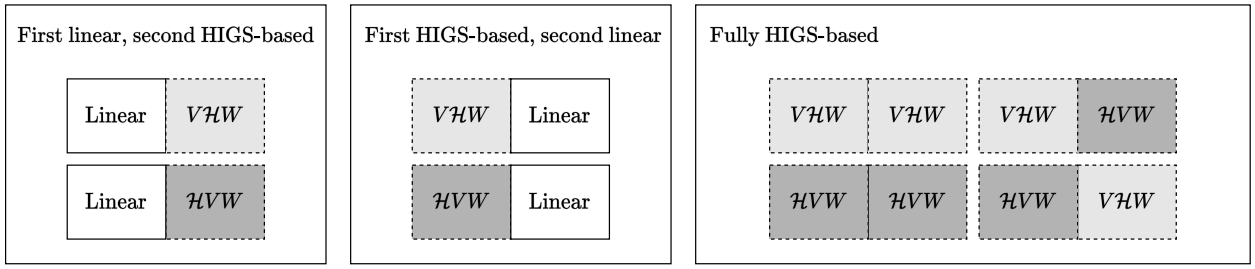

Figure 3.6: Schematic overview of the different HIGS-based PI2 controller configurations possible with the parallel configuration given in Figure 3.4b.

and with linear PI2 controller design used in the paper. Despite having very similar frequency domain characteristics, a parallel baseline configuration is preferred for the design of HIGS-based PI2 controllers based on time-domain reasoning.

The reason to switch from a series to parallel configuration is as follows. The parallel configuration has relevant advantages over the series configuration for some HIGS-based controller designs. Consider the case that the second linear integrator is replaced by a HIGS-based integrator. With the series configuration, the input towards the second HIGS is the first proportional path and a HIGS-based integrator path. The HIGS-based integrator path provides roll-off, whereas the proportional path does not. Despite the fact that the first proportional path cannot contain directly generated higher harmonics, it can contain higher harmonics present in the closed-loop system or other parasitic high-frequency content (e.g. quantization frequencies), which all could affect gain loss. With the parallel configuration, the input towards the second HIGS contains only an integrator path and thus less parasitic high-frequency content, thereby being less prone to gain loss.

Furthermore, the location of k_p is arbitrarily chosen in front of the controller loop. Placing it at the end of the controller loop is empirically found to give the same result irrespective of input frequency/frequencies and irrespective of HIGS-based PI2 controller design. Similarly, the location of the integrator gains can be in front or after a HIGS-based integrator, both giving the same response.

Finally, the HIGS-based PI2 controller designs are schematically represented in Figure 3.6. One could replace both of the linear integrators with either of the HIGS-based integrator designs (3.2), but one could also replace only the first or second linear integrator with a HIGS-based integrator. Considering all different options, this gives a total of eight possible configurations.

3.4.2 Gain loss filter design

In this subsection, a gain loss filter that is suited for both HIGS-based integrator designs (3.2) within each of the eight HIGS-based PI2 controller designs is presented. First, the origin of gain loss within the peristaltic pump system is analyzed, as well as the effect of different motor speeds on the amount of gain loss. Then, trade-offs in the design of a gain loss filter are elaborated on, after which the final gain loss filter design is presented. The design is also briefly compared to the design in the paper (Section 3.2).

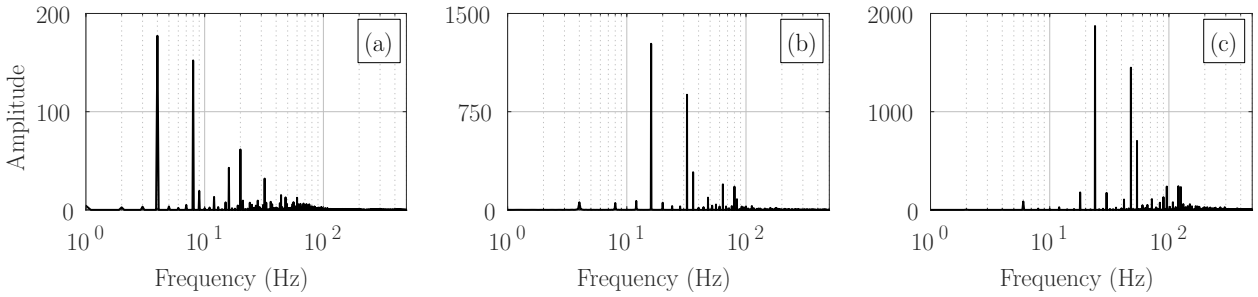

Figure 3.7: Input towards the second HIGS with HIGS-based PI2 controller configuration $V\mathcal{H}W|V\mathcal{H}W$ (without gain loss filters) for a setpoint speed of (a) 1; (b) 4 and (c) 6 rps, without including quantization.

Origin of gain loss

In order to design a gain loss filter, the origin of gain loss within the HIGS-based integrator should first be analyzed. As mentioned in Section 3.3.2, a prominent factor causing gain loss is quantization. Quantization is generally a very nonlinear and therefore unpredictable phenomenon, as quantization frequencies and the corresponding amplitudes strongly depend on the input frequencies. However, an observation from simulations is that the quantization frequencies are mainly present at frequencies above the input frequency or input frequencies, thereby being a prominent source for gain loss. With HIGS-based integrator design $V\mathcal{H}W$, PD filter V in front of the HIGS additionally amplifies high-frequency components in the input towards HIGS, such that the severity of gain loss is generally larger than with HIGS-based integrator design $\mathcal{H}VW$, as also concluded in Section 3.3.2.

An additional factor causing gain loss is the presence of higher harmonics. Especially for configurations with two HIGS-based integrators, the second HIGS-based integrator is likely to experience gain loss as a result of higher harmonics generated by the first HIGS-based integrator. Using simulations, it is found that prominent higher harmonic peaks in the input of HIGS are generally present at frequencies in Hz starting from factor 12 times the setpoint speed, whereas the largest higher harmonic peaks in Hz are generally present around factor 16 to 20 times the setpoint speed in rps. This is shown in an example in Figure 3.7, where the input of the second HIGS of HIGS-based PI2 controller configuration $V\mathcal{H}W|V\mathcal{H}W$ (without gain loss filters) is shown for a setpoint speed of 1, 4 and 6 rps, without including quantization. Here, pump ripple frequencies in Hz are present at factor 4, 8 and 9 times the setpoint speed in rps (Section 2.3.2), whereas the other peaks visible are higher harmonics generated by the HIGS elements.

Motor speed-dependency

The amount of gain loss experienced by a HIGS-based integrator within a HIGS-based PI2 controller is motor speed-dependent. Generally, more gain loss occurs at lower motor speeds, as found in the paper (Section 3.2). The reason for this is twofold. First of all, at lower speeds, pump ripple frequencies are lower (see Figure 2.7), thereby prominent higher harmonic frequencies and quantization frequencies are generally lower. At lower frequencies, there is less attenuation by the roll-off characteristics of linear integrators and by roll-off characteristics of the plant, such that the amplitude of the higher harmonics and quantization remains larger relative to the amplitude of the pump ripple frequencies, causing more gain loss. Secondly, at lower speeds, pump ripple frequencies are lower, thereby disturbance rejection is better, such that the setpoint error is smaller compared to higher speeds. Additionally, pump ripple amplitudes are lower at lower motor speeds, also contributing to a smaller setpoint error (see Figure 2.7). The result is generally that the quantization step size of the input towards HIGS is relatively large, i.e. the amplitude of quantization frequencies is large relative to the amplitude of the pump ripple frequencies, resulting in more gain loss. This was found to be the case especially with HIGS-based integrator design $V\mathcal{H}W$, as here PD filter V amplifies high-frequency content in the input towards HIGS. At higher speeds, the opposite could be true, such that less or no gain loss occurs. A gain loss filter would then not improve performance, but possibly deteriorate performance as a result of post-filtering the HIGS with the inverse of the gain loss filter, thereby amplifying generated higher harmonics. One could design a gain loss filter with poles and/or zeros proportional to the motor speed, which possibly improves performance at all speeds. The additional complexity involved with designing an adaptive gain loss filter however does not outweigh the expected performance improvements with such a filter.

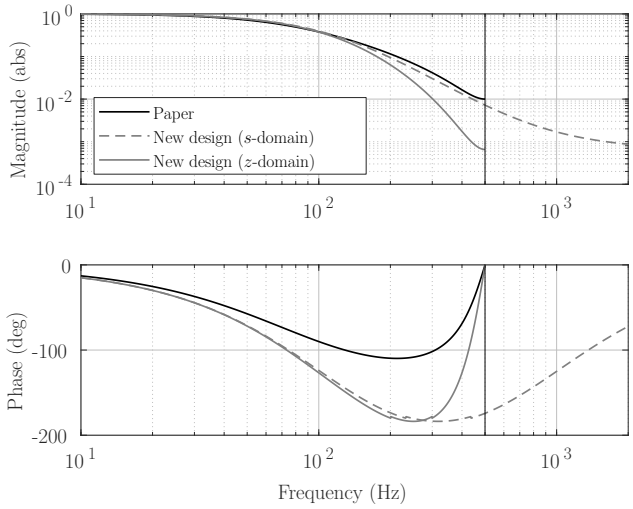

Figure 3.8: Bode diagram of the discretized gain loss filter used in the paper (Section 3.2), the newly designed gain loss filter (3.6) and its discretized version.

Trade-offs in design

The fact that the peristaltic pump operates at setpoint speeds from 1 to 6 rps poses trade-offs in the design of the gain loss filter. For a speed of 1 rps, the largest pump ripple frequency is 9 Hz, such that attenuation with a gain loss filter is desired after 9 Hz, as after 9 Hz, prominent parasitic higher harmonics and quantization frequencies could be present. For a speed of 6 rps, the largest pump ripple frequency is 54 Hz, such that attenuation with a gain loss filter is desired after 54 Hz. When attenuation would start below 54 Hz, pump ripple frequencies are suppressed as well, which is undesired. There thus exists a trade-off between sufficiently attenuating parasitic high-frequency content at low speeds and not attenuating pump ripple content at higher speeds.

Final design

The gain loss filter that desirably deals with the aforementioned trade-off is found to be a fourth-order lag filter given by

$$C_{gl}(s) = \frac{\omega_p^4}{\omega_z^4} \frac{(s+\omega_z)^4}{(s+\omega_p)^4}, \tag{3.6}$$

with $\omega_z = 50000$ rad/s and $\omega_p = 500$ rad/s. The filter is discretized using the Tustin method. Note that the zero $\omega_z = 50000$ rad/s is located at a higher frequency than the Nyquist frequency ($500{\cdot}2\pi$ rad/s), which in continuous time would not be implementable. However, when discretized, this results in an implementable filter that has characteristics which are not possible to obtain in continuous time, but are desired to have. The rational behind the newly designed discretized gain loss filter is to ensure attenuation starts from approximately 24 Hz onwards, which is the largest base frequency of the pump ripple considered, and attenuation becomes stronger especially after 54 Hz, which is the largest pump ripple frequency considered.

The discretized gain loss filter (3.6) is shown in a Bode diagram in Figure 3.8. Additionally, the discretized gain loss filter used in the paper (Section 3.2) is plotted for comparison. The newly designed gain loss filter is preferred over the gain loss filter in the paper as it provides stronger suppression at higher frequencies, thereby providing more attenuation against parasitic high-frequency content in the input towards HIGS. The flattening magnitude shape of both filters close to the Nyquist frequency ensures that post-filtering the HIGS with the inverse gain loss filter does not excessively amplify generated higher harmonic content.

3.4.3 Tuning methodology

HIGS-based PI2 controllers with one HIGS-based integrator

Four out of the eight HIGS-based PI2 controller configurations (Figure 3.6) contain only one HIGS-based integrator and one linear integrator, being

- Linear$|V\mathcal{H}W$,

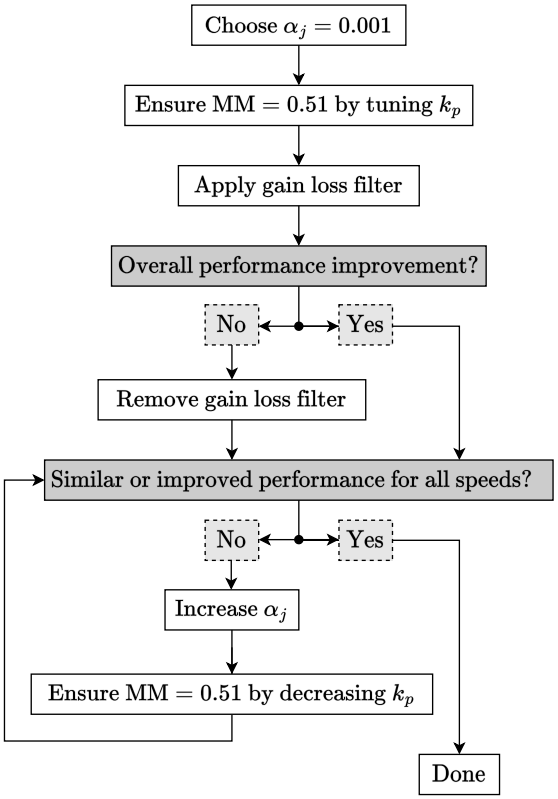

Figure 3.9: Tuning methodology of HIGS-based PI2 controllers with one HIGS-based integrator and one linear integrator.

- Linear$|\mathcal{H}VW$,
- $V\mathcal{H}W|$Linear,
- $\mathcal{H}VW|$Linear.

A tuning methodology for these controller configurations is developed, which is schematically illustrated in Figure 3.9. The methodology is further elaborated on below.

Integrator frequency ω_h is the tuning parameter for HIGS (k_h is always set equal to 1), and is defined as

$$\omega_{h,j} = \alpha_j k_{i,j}, \quad j = \{1, 2\}. \tag{3.7}$$

It follows from frequency domain approximations that α_j should be chosen small to realize optimal phase advantages (see Figure 3.1), which in turn opts for the largest bandwidths/disturbance rejection performance. Additionally, choosing α_j small results in local magnitude improvements for a HIGS-based PI filter compared to a linear PI filter, as shown in the paper (Section 3.2). An infinitely low value for α_j however is of no use, as phase and local magnitude improvements are not unbounded and robustness margins pose limits on closed-loop bandwidth and disturbance rejection properties. A value of $\alpha_j = 0.001$ is found sufficiently low.

However, such a low value for α_j also gives more nonlinearity. With HIGS-based integrator I_2, the output of HIGS is subject to PD filter V (3.1), thereby strongly amplifying higher harmonics generated by the HIGS, possibly affecting performance if subsequent roll-off by integrators or by the plant is not sufficient. With HIGS-based integrator I_1, the input of HIGS is subject to PD filter V (3.1), thereby strongly amplifying high-frequency noise in the input towards the HIGS, possibly resulting in gain loss and thereby affecting performance.

If gain loss occurs, appending the HIGS with gain loss filter (3.6) could improve performance. If this does not improve the overall performance, the filter should again be removed. Finally, one should check whether similar or improved performance is obtained for all speeds. If so, the design is done. If not, one should increase α_j. This will then generally improve performance, or at least result in similar performance as with linear PI2 control, as for larger α_j, the HIGS-based integrator approaches a linear integrator (see Figure 3.1). However, this also reduces the phase advantages of HIGS, thereby reducing the performance improvements compared to linear PI2 control.

HIGS-based PI2 controllers with two HIGS-based integrators

Four out of the eight HIGS-based PI2 controller configurations contain two HIGS-based integrators, being

- $V\mathcal{H}W|V\mathcal{H}W$,
- $\mathcal{H}VW|\mathcal{H}VW$,
- $V\mathcal{H}W|\mathcal{H}VW$,
- $\mathcal{H}VW|V\mathcal{H}W$.

By means of extensive trial and error using simulations, it is found that the tuning settings of HIGS-based PI2 controllers with only one HIGS-based integrator can almost straightforwardly be applied to HIGS-based PI2 controllers with two HIGS-based integrators, e.g. the optimal tuning settings for $\mathcal{H}VW|$Linear and Linear$|V\mathcal{H}W$ can almost straightforwardly be combined to get the optimal tuning settings for $\mathcal{H}VW|V\mathcal{H}W$.

Two additional actions should however be performed, the first one being adjusting k_p to ensure a modulus margin of 0.51. Secondly, it should be verified whether the addition of gain loss filter (3.6) to the second HIGS-based integrator is beneficial. Due to the fact that higher harmonic content generated by the first HIGS-based integrator is propagated towards the input of the second HIGS-based integrator, possibly (more) gain loss occurs. Besides, if the first HIGS-based integrator contains a gain loss filter, its generated higher harmonics might additionally be amplified as a result of post-filtering with the inverse gain loss filter, thereby resulting in additional parasitic high-frequency content in the input towards the second HIGS-based integrator, possibly resulting in (more) gain loss.

3.4.4 Selecting the optimal design

Using the tuning methodology described in Section 3.4.3, the different HIGS-based PI2 controllers are tuned, analyzed and compared. A summary of the findings is presented below.

It is found that configurations with $\mathcal{H}VW$ as replacement of the second linear integrator are unsuited both in configurations with one and with two HIGS-based integrators. As a result of post-multiplicating the HIGS with PD filter V (3.1), higher harmonics generated by the HIGS are strongly amplified. The higher harmonics are subsequently looped to the plant, affecting performance. Especially at lower motor speeds, where pump ripple frequencies are lower, such that higher harmonics occur at lower frequencies and roll-off from linear integrator W (3.1) and roll-off from the plant is limited, the effect is significant. By increasing α_j, one shifts the zero of PD-filter V (3.1) forward, such that generated higher harmonics are less amplified. However, the necessary increment in α_j is too large to still experience the desired (phase) advantages from HIGS, both in constructions with one and two HIGS-based integrators.

Configurations with $V\mathcal{H}W$ as replacement of the second linear integrator are suited. For $\alpha_j = 0.001$, the construction Linear$|V\mathcal{H}W$ experiences a slight amount of gain loss. Quantization frequencies seem mostly attenuated by the first linear integrator, such that these hardly affect switching of the HIGS within $V\mathcal{H}W$. The addition of a gain loss filter hardly improves switching at lower speeds but reduces performance at higher speeds. The reason is that HIGS already switched desirably at higher speeds, such that the addition of a gain loss filter, thereby amplifying generated higher harmonics in the post-filter, reduces performance. A gain loss filter is thus not desired here.

For configurations with two HIGS-based integrators in the controller, only $V\mathcal{H}W|V\mathcal{H}W$ and $\mathcal{H}VW|V\mathcal{H}W$ are thus left as suitable options. Both configurations benefit from having a gain loss filter within both HIGS-based integrators. The configurations show similar performance. It is found that the two aforementioned configurations give overall better performance than any configuration with one HIGS-based integrator, such that configurations with one HIGS-based integrator are not further considered. To make a proper choice between $V\mathcal{H}W|V\mathcal{H}W$ and $\mathcal{H}VW|V\mathcal{H}W$, an additional transient performance analysis is performed, which can be found in Section 3.4.5. In short, a significant improvement in overshoot for similar rise time was found for $V\mathcal{H}W|V\mathcal{H}W$ compared to $\mathcal{H}VW|V\mathcal{H}W$, such that finally, $V\mathcal{H}W|V\mathcal{H}W$ is found to be the optimal HIGS-based PI2 configuration and is therefore selected. An overview of the tuning settings for $V\mathcal{H}W|V\mathcal{H}W$ can be found in Table 3.3, where it is referred to as 'New design'.

3.4.5 Transient analysis

In this section, a small transient performance analysis in terms of rise time and overshoot is performed for HIGS-based PI2 controller designs $V\mathcal{H}W|V\mathcal{H}W$ and $\mathcal{H}VW|V\mathcal{H}W$, after which an optimal design is chosen based on the analysis. The tuning settings used for both controllers can be found under the name 'New design' in Table 3.3. Note that for both $V\mathcal{H}W|V\mathcal{H}W$ and $\mathcal{H}VW|V\mathcal{H}W$, both HIGS-based integrators contain a gain loss filter.

Table 3.1: Overshoot values with HIGS-based control and linear control for setpoint speeds ranging from 1 to 6 rps. Improvement is calculated using $\frac{\text{OS linear}-\text{OS HIGS}}{\text{OS linear}} \cdot 100\%$.

Setpoint	(rps)	1	2	3	4	5	6
OS linear	(rps)	0.22	0.48	0.70	0.94	1.22	1.50
OS $V\mathcal{H}W\|V\mathcal{H}W$	(rps)	0.11	0.27	0.43	0.51	0.65	0.75
Improvement	(%)	44.0	43.8	38.6	45.7	47.5	50.0

Table 3.2: Overshoot values with HIGS-based control and linear control for setpoint speeds ranging from 1 to 6 rps. Improvement is calculated using $\frac{\text{OS linear}-\text{OS HIGS}}{\text{OS linear}} \cdot 100\%$.

Setpoint	(rps)	1	2	3	4	5	6
OS linear	(rps)	0.22	0.48	0.70	0.94	1.22	1.50
OS $\mathcal{H}VW\|V\mathcal{H}W$	(rps)	0.21	0.37	0.61	0.80	1.05	1.17
Improvement	(%)	4.5	22.9	12.9	14.9	13.9	22.0

For the transient analysis, the setup in Figure 2.1 is subjected to a pulse of the form

$$r_{pulse}(\omega) : \begin{cases} \frac{\omega}{2}, & \text{if } t < t_{step}, \\ \omega, & \text{if } t \geq t_{step}, \end{cases} \tag{3.8}$$

where ω represents the speeds considered, being 1 to 6 rps, and where t represents time and t_{step} is the time instance at which the pulse/step occurs. The actuator used in the peristaltic pump setup might have a preferred starting position, such that the pulse is not initiated from zero speed, but at half the speed of the final setpoint speed. Besides, the experienced transient response is found to strongly depend on the configuration of the rollers, i.e. whether rollers are engaging with and disengaging from the tube during the transient period. To omit this configuration dependence, the system is consecutively subject to 20 of these pulses, occurring 2π s apart, from which the average findings are used for further analysis.

Measurements are performed using linear PI2 controller (3.5) and using HIGS-based PI2 controllers $V\mathcal{H}W|V\mathcal{H}W$ and $\mathcal{H}VW|V\mathcal{H}W$. The obtained rise time values with all three controllers are found very similar and as low as in the order of 0.01 s for all six setpoint speeds (1 to 6 rps). The differences between HIGS-based PI2 controllers are in the order of 0.001 s, which is considered negligible, such that rise time is not further analyzed. However, significant differences in overshoot (OS) were found and are displayed in Table 3.1 and 3.2.

The overshoot significantly reduces with both HIGS-based PI2 controllers. With $V\mathcal{H}W|V\mathcal{H}W$, the improvement in overshoot is significantly more than with $\mathcal{H}VW|V\mathcal{H}W$. Pre-multiplication with PD filter V (3.1) results that HIGS switches based on a differentiated signal, such that it 'predicts' the future and therefore seems to act sooner on a changing input, thereby resulting in less overshoot. According to this analysis, configuration $V\mathcal{H}W|V\mathcal{H}W$ is thus preferred.

3.5 Conference paper design versus new design

In this section, performance with the HIGS-based PI2 controller designed in the paper (Section 3.2) is compared to the performance with the newly designed HIGS-based PI2 controller (Section 3.4). As a reference, performance with linear PI2 controller (3.5) is also evaluated. For a fair comparison between both HIGS-based controllers, values for their tuning parameters are obtained according to the same methodology, being that integrator gains $k_{i,1}$ and $k_{i,2}$ are kept identical to the values of linear PI2 controller (3.5), but k_p is altered to ensure a MM of 0.51. An overview of the two HIGS-based PI2 controller designs can be found in Table 3.3.

Table 3.3: Overview of the HIGS-based PI2 controller design from the paper (Section 3.2) and the new HIGS-based PI2 controller design (Section 3.4).

	Configuration	k_p	α_1	α_2	$C_{gl}(s)$
Paper	Series	0.025	0.5	0.5	$\frac{\omega_p^2}{\omega_z^2}\frac{(s+\omega_z)^2}{(s+\omega_p)^2}$
New design	Parallel	0.029	0.8	0.001	$\frac{\omega_p^4}{\omega_z^4}\frac{(s+\omega_z)^4}{(s+\omega_p)^4}$

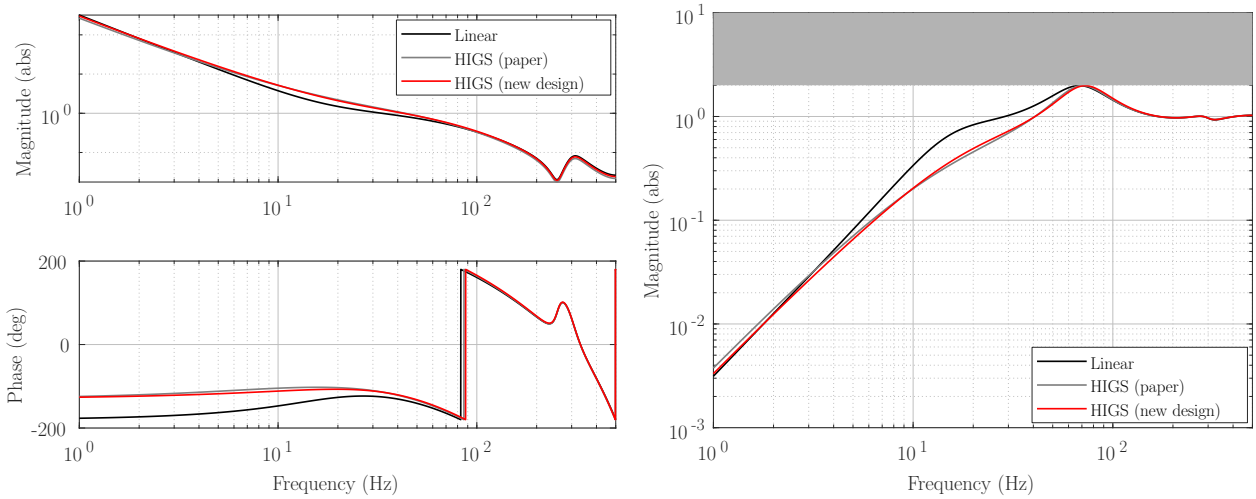

Figure 3.10: (a) Bode diagram of the open loop and (b) Bode magnitude diagram of the sensitivity function with linear PI2 controller (3.5) (black), the HIGS-based PI2 controller from the paper (Section 3.2) (dark gray) and the newly designed HIGS-based PI2 controller (Section 3.4) (red).

Table 3.4: RMS values of the simulated steady-state setpoint error with linear PI2 controller (3.5), with the HIGS-based PI2 controller design from the paper and with the new HIGS-based PI2 controller design for setpoint speeds ranging from 1 to 6 rps. Improvement of the new HIGS-based controller w.r.t. the paper is calculated using $\frac{\text{RMS HIGS (paper)} - \text{RMS HIGS (new design)}}{\text{RMS HIGS (paper)}} \cdot 100\%$ and improvement w.r.t. the linear PI2 controller is calculated using $\frac{\text{RMS linear} - \text{RMS HIGS (new design)}}{\text{RMS linear}} \cdot 100\%$.

Setpoint	(rps)	1	2	3	4	5	6
RMS linear	(rps)	0.064	0.218	0.383	0.558	0.703	0.822
RMS HIGS (paper)	(rps)	0.085	0.181	0.291	0.360	0.500	0.673
RMS HIGS (new design)	(rps)	0.064	0.149	0.245	0.356	0.495	0.666
Improvement w.r.t linear	(%)	0	31.7	36.0	35.5	29.6	19.0
Improvement w.r.t paper	(%)	24.7	17.7	15.8	1.1	1.0	1.0

Figure 3.10a shows a Bode diagram of the open loop with linear PI2 controller (3.5), with the HIGS-based PI2 controller from the paper (Section 3.2) (dark gray) and with the newly designed HIGS-based controller (Section 3.4) (red). Figure 3.10b shows a Bode magnitude diagram of the sensitivity function with the three controllers. The HIGS-based controllers are approximated in the frequency domain using describing function analysis, similar to the approach outlined in the paper (Section 3.2). The figures indicate very similar frequency domain characteristics for both HIGS-based controllers, thereby hardly any difference in performance is expected based on these frequency domain approximations.

However, in the time domain, significant differences can be observed. For this, performance with the three controllers is simulated on nominal plant model (2.2), additionally using pump ripple model (2.7) and including the effect of quantization (Section 2.2). The system is subject to angular speed setpoints ranging from 1 to 6 rps. For each of the six setpoints, steady-state simulations of 60 s are conducted using either linear PI2 control or either of the HIGS-based PI2 control strategies. The simulated steady-state setpoint error of the motor speed, defined as $e(t) = \dot{\theta}_1(t) - \dot{\theta}_r(t)$, is used to quantify the RMS values, which are defined as performance measure in Section 1. The results are summarized quantitatively in Table 3.4 and Figure 3.11.

Small fragments of 0.5 s of the simulated steady-state setpoint error with linear PI2 controller (3.5) with the HIGS-based PI2 controller from the paper (dark gray) and with the newly designed HIGS-based controller (red) are shown in the left column in Figure 3.11, whereas a frequency-domain analysis in terms of the cumulative power spectral density is shown in the right column in Figure 3.11. The square root of the cumulative power spectral density plot at the Nyquist frequency (500 Hz) indicates the RMS values of the setpoint error, for which the exact values are listed in Table 3.4.

Both the time-domain plots in Figure 3.11 as well as the RMS values in Table 3.4 show that for lower motor speeds, performance with the new HIGS-based controller design is significantly improved compared to the design in the paper. This seems attributed to a reduction in gain loss. This is partly contributed to

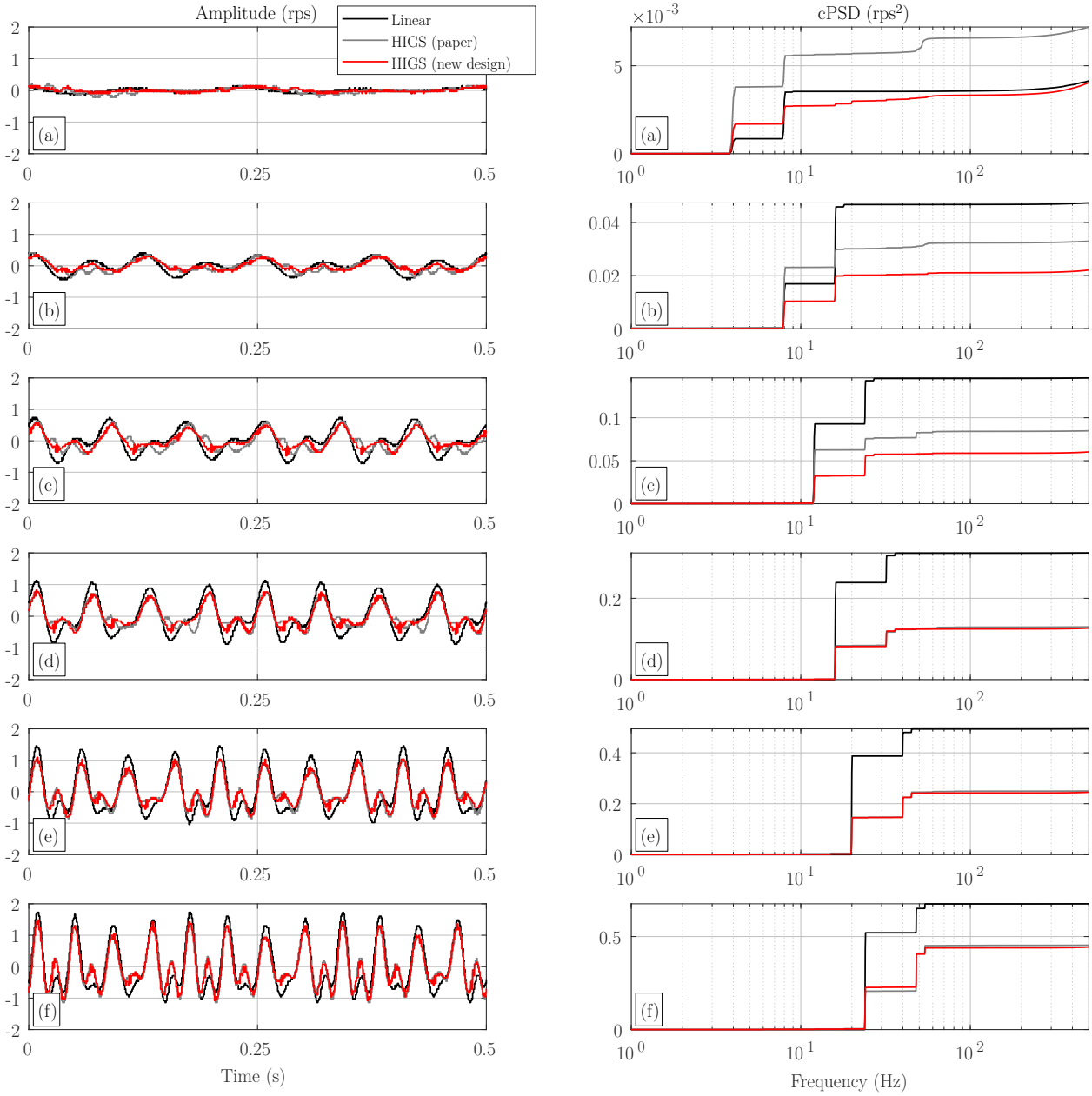

Figure 3.11: (left) Steady-state time domain simulations and (right) cumulative power spectral density representation of the setpoint error with the HIGS-based PI2 controller design from the paper (dark gray) and with the new HIGS-based PI2 controller design (red) for setpoint speeds ranging from (a) 1; (b) 2; (c) 3; (d) 4; (e) 5; to (f) 6 rps.

Table 3.5: RMS values of the measured setpoint error with linear PI2 controller (3.5) and with the new HIGS-based PI2 controller design for setpoint speeds ranging from 1 to 6 rps. Improvement is calculated using $\frac{\text{RMS linear}-\text{RMS HIGS (new design)}}{\text{RMS linear}} \cdot 100\%$.

Setpoint	(rps)	1	2	3	4	5	6
RMS linear	(rps)	0.085	0.170	0.277	0.386	0.454	0.501
RMS HIGS (new design)	(rps)	0.093	0.159	0.210	0.270	0.325	0.368
Improvement	(%)	-9.4	6.5	24.2	30.1	28.4	26.5

the improved gain loss filter design. Another part is contributed to the parallel configuration, which ensures the input towards the second HIGS contains less parasitic high-frequency content compared to the series configuration. The largest factor reducing the amount of gain loss is the increased value for α_1 compared to the paper, which increases the frequency of the zero of PD filter V (3.1), thereby providing less amplification of parasitic high-frequency content in the input towards the first HIGS-based integrator. Besides, the increased value for α_1 reduces the higher harmonic content generated by the first HIGS-based integrator, such that the input towards the second HIGS-based integrator contains less parasitic high-frequency content. Furthermore, the reduced value for α_2 increased the magnitude and phase improvements with the second HIGS-based integrator, thereby making up for the reduced magnitude and phase improvements of the first HIGS-based integrator as a result of a higher α_1.

3.6 Experimental results

In this section, performance with linear PI2 controller (3.5) is experimentally compared to the performance with the newly designed HIGS-based PI2 controller (Section 3.4) on the peristaltic pump setup shown in Figure 2.1. During the experiments, the system is subject to angular speed setpoints ranging from 1 to 6 rps. For each of the six setpoints, steady-state measurements of 60 s are conducted using either linear or HIGS-based control. The measured steady-state setpoint error of the motor speed, defined as $e(t) = \dot{\theta}_1(t) - \dot{\theta}_r(t)$, is used to quantify the RMS values, which are defined as performance measure in Section 1. The results are summarized quantitatively in Table 3.5 and Figure 3.12.

Small fragments of 0.5 s of the measured setpoint error with linear (black) and HIGS-based control (red) are shown in the left column in Figure 3.12. A frequency-domain analysis in terms of the cumulative power spectral density is shown in the right column in Figure 3.11. At higher speeds, the HIGS-based PI2 controller outperforms the linear PI2 controller, with improvements up to 30.1% in terms of RMS value. This observation is in line with the expectations coming from the (approximate) sensitivity function plots in Figure 3.10b. However, at a motor speed of 1 rps, corresponding to a base frequency of the pump ripple of 4 Hz, there appears to be a slight deterioration in terms of RMS value, which is not in line with the expectations coming from these plots. This seems attributed to gain loss at a frequency of 4 Hz. Note that the cumulative power spectral density plot shows a significantly larger power at 4 Hz with HIGS-based control compared to linear control, whereas the power distribution at larger frequencies is relatively similar. A similar observation can be made for a motor speed of 2 rps, corresponding to a base frequency of the pump ripple of 8 Hz, although the difference between expectation based on approximated sensitivity function plots and the cumulative power spectral density plots is much smaller. A simple adjustment that likely improves performance at 1 and 2 rps is increasing the value for α_1, but note that this likely comes at the cost of performance at higher speeds.

Furthermore, note that the experimental performance shows differences with the performance obtained with simulations (compare Figure 3.11 and Table 3.4 with Figure 3.12 and Table 3.5, respectively). This seems strongly attributed to time-variance in the dynamics of the peristaltic pump shown in Figure 2.1, which was observed throughout the experimental validation. The models used within the simulations are based on measurement data from a different day compared to the measurement data in this section. Time-variance of the dynamics is not further analyzed in this thesis.

3.7 Conclusions

This chapter presented a HIGS-based PI2 controller design for the peristaltic pump developed by Demcon to reduce the steady-state setpoint error of the motor speed compared to linear PI2 control while at least maintaining the same robustness margins. An initial design was provided by means of conference paper submission. After an elaborate analysis on HIGS-based PI2 controller design, a structured tuning methodology for HIGS-based PI2 controllers was developed, eventually resulting in an improved design compared

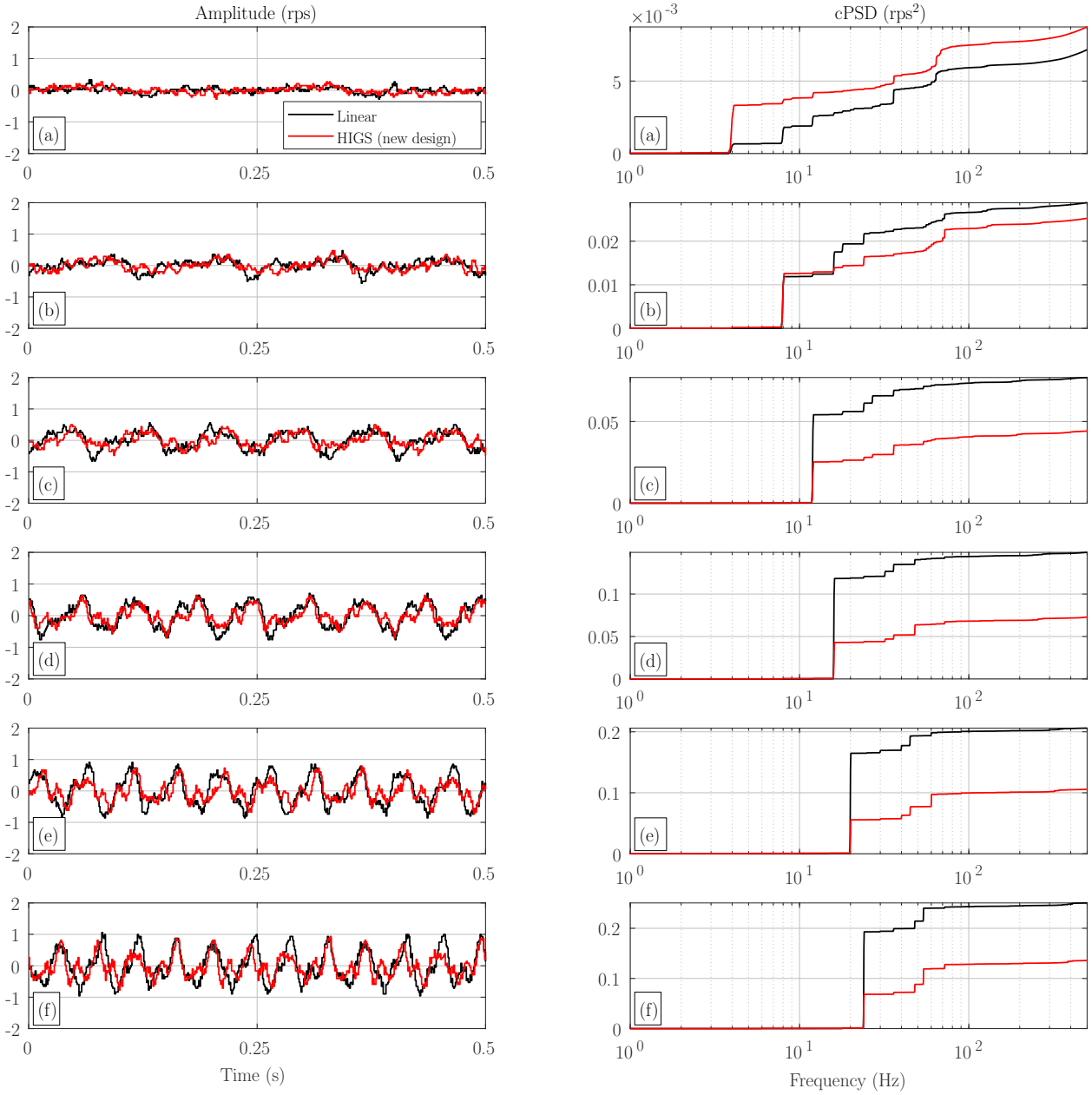

Figure 3.12: (left) Steady-state time domain measurements and (right) cumulative power spectral density representation of the setpoint error with linear PI2 control (black) and with HIGS-based PI2 control (red) for setpoint speeds ranging from (a) 1; (b) 2; (c) 3; (d) 4; (e) 5; to (f) 6 rps.

Table 3.6: Controller parameters of the linear PI2 controller design.

	Design 1	Design 2	Design 3	Design 4
k_p	0.033	0.040	0.025	0.024
$k_{i,1}$	60π	25π	90π	90π
$k_{i,2}$	20π	25π	10π	30π

to the paper. Where the conference paper design lacked at lower speeds, the new design made up for this, showing improvements up to 24.7% in terms of RMS value using simulations. Key for these improvements is contributed to a different gain loss filter design, a switch from series to parallel baseline configuration and different values for HIGS tuning parameter ω_h. Experimental validation of the new HIGS-based PI2 controller design showed slightly deteriorated performance at the lowest motor speed compared to linear PI2 control, which seems to be attributed to gain loss, but improved performance for all higher considered motor speeds, showing improvement up to 30.1% in terms of RMS value. Additionally, transient improvements up to 50.0% in terms of overshoot were observed, all for similar rise time, and while maintaining the same robustness margins as obtained with linear PI2 control.

3.8 Appendix: Linear PI2 controller design

A linear PI2 speed controller is designed for the peristaltic pump shown in Figure 2.1. The controller adheres to the parallel configuration presented in Figure 3.4b. Nominal plant model P_n (2.2) is used as plant for the controller design. The design of the controller should comply with set requirements by Demcon, being that the closed-loop system should

- be robustly stable (gain margin > 2, phase margin $> 30°$, modulus margin > 0.5) and
- have a bandwidth ≥ 30 Hz.

Furthermore, there are additional design considerations. The pump ripple is considered an input disturbance. Rejection of input disturbances is characterized by the sensitivity function, which is given by

$$S(s) = \frac{1}{1 + P(s)C(s)}. \tag{3.9}$$

As stated in Section 2.3.1, the most prominent pump ripple frequencies occur up to 54 Hz, whereas the largest peaks occur up to 24 Hz. A strong disturbance rejection, i.e. a low sensitivity function, up to 54 Hz is thus desired, and especially up to 24 Hz.

Four different considerable controller designs with the parallel configuration in Figure 3.4b are shown in the top-left in Figure 3.13. The designs are discretized using the Tustin method. All designs are robustly stable with a modulus margin equal to 0.51, as indicated in the sensitivity function plot in Figure 3.13. A larger gain margin comes at cost of a larger phase margin, as shown in the open loop plot in the top-right in Figure 3.13. All designs also meet the bandwidth requirement of 30 Hz, as indicated in the Bode magnitude plot of the complementary sensitivity function in the bottom-right in Figure 3.13. The controller parameters for the four different options are displayed in Table 3.6.

As stated above, a low sensitivity function is desired up to 54 Hz, and especially up to 24 Hz, as this is the frequency of the most prominent contribution to the pump ripple. Above 54 Hz, the sensitivity function can be larger. Up to 14 Hz, Design 4 has the lowest sensitivity function, Design 3 between 14 and 19.5 Hz and Design 2 between 19.5 and 66.5 Hz. As a result of the waterbed effect, increments in a certain frequency range come at cost of decrements in another. The large increment in sensitivity between 14 and 54 Hz is undesired, just as the large increment between 3 and 17 Hz with Design 2, so these designs are not chosen. Design 1 shows an improved sensitivity function below 9 and above 25.5 Hz compared to Design 3, whereas Design 3 overrules Design 1 in between these frequencies. To quantify the overall difference, the area under the sensitivity function up to 54 Hz is calculated for both designs, indicating a 13% lower area for Design 1 than Design 3. Besides, Design 1 has a bandwidth of 85.8 Hz whereas Design 3 has a bandwidth of 74.2 Hz, which benefits reference tracking. Then, the peristaltic pump is in practice mainly being used at relatively low speeds, where Design 1 shows a better disturbance rejection. The final choice for a baseline linear PI2 controller is therefore Design 1.

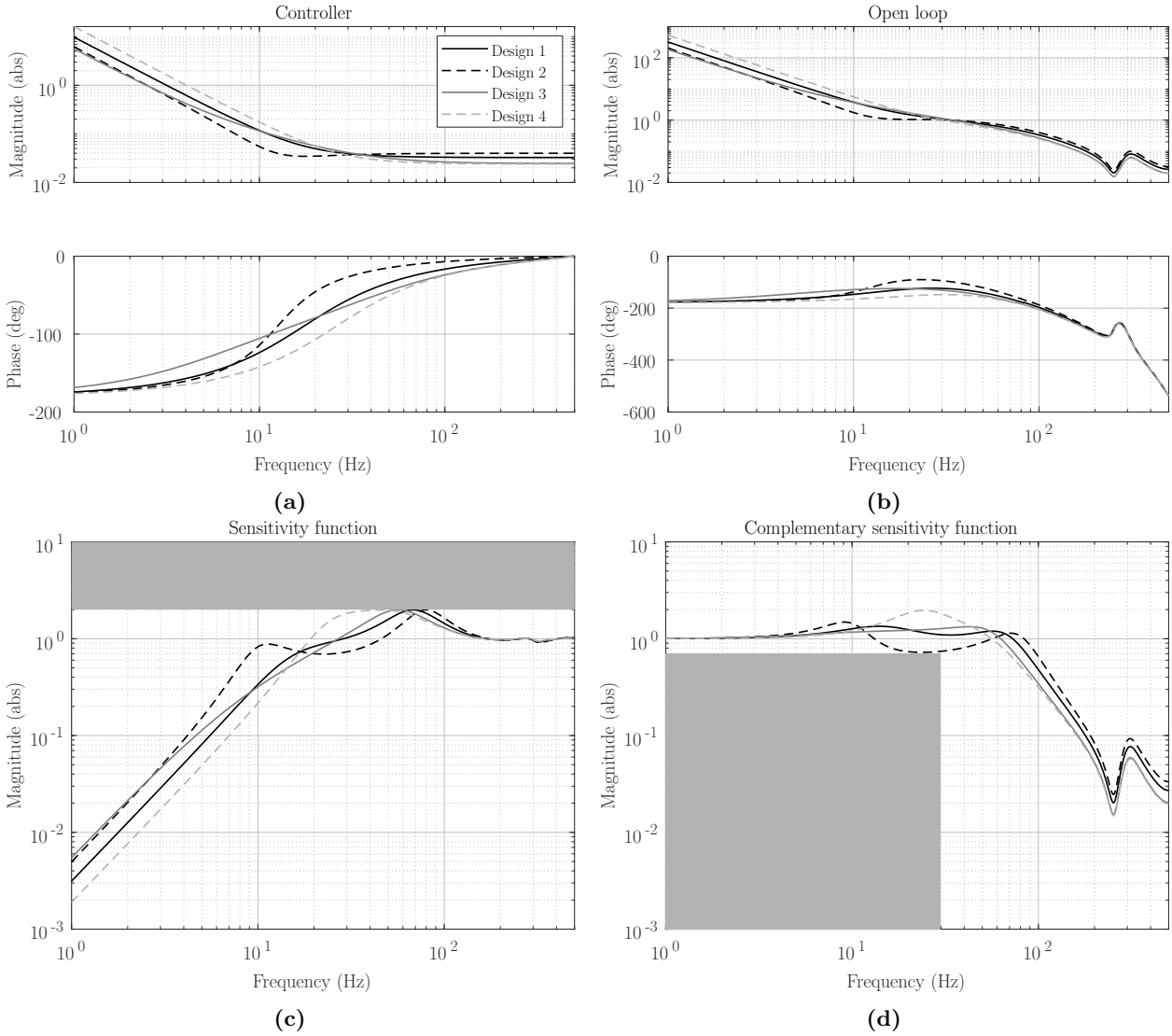

Figure 3.13: (a) Four different linear controller designs; (b) the corresponding open loops; (c) the sensitivity functions along with the 0.5 modulus margin; (d) the complementary sensitivity functions along with the bandwidth requirement of 30 Hz.

Chapter 4

Inversion-based disturbance-observer-based control

4.1 Introduction

This chapter presents a disturbance observer design for the purpose of reducing the steady-state setpoint error of the motor speed of the peristaltic pump shown in Figure 2.1 compared to linear PI2 control. The specific method used here is called 'inversion-based disturbance-observer-based control' (IBDOBC), which is a variant of 'disturbance-observer-based control' (DOBC) [15]. The concept of IBDOBC is illustrated in Figure 4.1, with conventional feedback controller C, plant P, nominal plant model P_n, LTI filter Q, reference r, error e, feedback controller output c, disturbance observer output $\hat{d}$, total controller output u, input disturbances d and output y. The basic idea behind IBDOBC is to estimate input disturbances and/or uncertainties using an inverse nominal plant model and directly compensate the controller output with the estimate. The method assumes an LTI system and considers uncertainties or unmodeled dynamics as a part of the input disturbances, such that the effect of uncertainty on stability is disregarded. The disturbance observer is an addition to a linear feedback controller. The linear feedback controller can conventionally be designed according to tracking performance specifications and stability, whilst the disturbance observer is used to further reject disturbances and suppress uncertainties [14].

The design of the disturbance observer will closely resemble the approach outlined in Chapter 2.3.1, where the dynamics of the pump ripple were reconstructed from measurements. However, in this chapter, estimation of the pump ripple is not performed offline, but online, and the estimate is directly used to compensate the controller output. Latter implies that an additional loop is closed, such that stability of this closed loop should be checked. Besides, a different Q-filter design than (2.5) that is more suited for online implementation is considered.

This chapter is organized as follows. Section 4.2 presents some fundamentals of reference tracking and disturbance rejection with IBDOBC. A stability condition is elaborated on in Section 4.3. The Q-filter design is presented in Section 4.4, whereas performance with the disturbance observer is evaluated and compared

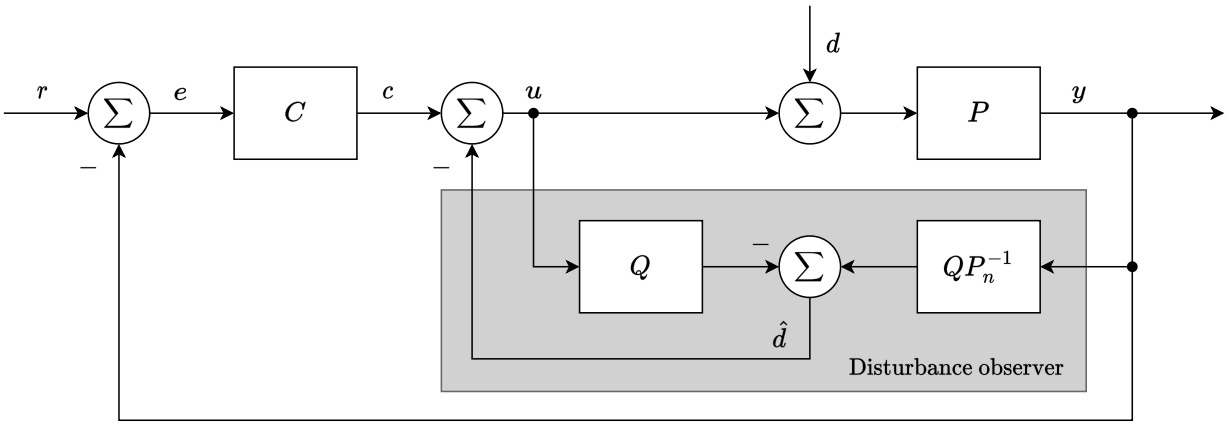

Figure 4.1: General block scheme of of IBDOBC.

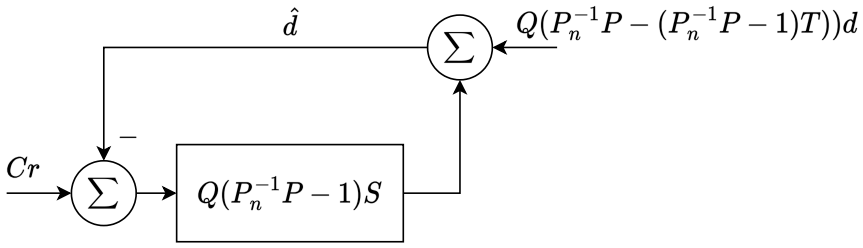

Figure 4.2: General block scheme of IBDOBC rewritten, with $S = (1 + PC)^{-1}$ and $T = PC(1 + PC)^{-1}$.

to the performance with only linear PI2 control using simulations in Section 4.9 and experimentally in Section 4.5. In addition, the performance with the combination of IBDOBC with HIGS-based PI2 control is evaluated and compared to linear PI2 control in Section 4.6. Section 4.7 outlines the main conclusions of this chapter.

4.2 Reference tracking and disturbance rejection

For conventional linear feedback systems (Figure 2.4), reference tracking and disturbance rejection can be expressed in terms of the complementary sensitivity function and the process sensitivity function, i.e. in the transfer from r to y and from d to y, respectively, given by

$$y(s) = \frac{P(s)C(s)}{1 + P(s)C(s)}r(s) + \frac{P(s)}{1 + P(s)C(s)}d(s). \tag{4.1}$$

With IBDOBC, this relation should be rewritten to

$$y(s) = \frac{P(s)C(s)}{1 + Q(s)(P_n^{-1}(s)P(s) - 1) + P(s)C(s)}r(s) + \frac{P(s)(1 - Q(s))}{1 + Q(s)(P_n^{-1}(s)P(s) - 1) + P(s)C(s)}d(s). \tag{4.2}$$

For a Q-filter design equal to 0, (4.2) and (4.1) are identical, as this describes the situation without IBDOBC. For a Q-filter design equal to 1 and a perfect nominal plant model, i.e. $P_n^{-1}P = 1$, the transfer from d to y becomes zero, implying perfect compensation of d, whereas the transfer from r to y remains unaffected by IBDOBC. However, for a Q-filter design equal to 1 and an imperfect nominal plant model, i.e. $P_n^{-1}P \neq 1$, the transfer from d to y is still zero, but the transfer from r to y is now affected by the uncertainty. Latter is undesired, as the disturbance observer is used for improved disturbance rejection without altering reference tracking performance. Then there are options where a Q-filter has a value in between 0 and 1, which could ensure a balance in aforementioned trade-offs.

In this thesis, the Q-filter cannot equal 1 as it needs to be used to ensure that the inverse nominal plant model (2.2) becomes stable and proper (similar as concluded in Section 2.3.1). The effect of different Q-filter designs on tracking and disturbance rejection is therefore evaluated in Section 4.4, as well as the effect of plant uncertainty.

4.3 Stability

Since IBDOBC closes an additional loop compared to a conventional linear feedback system, an additional stability check should be performed. To this end, the small-gain theorem [20] is used, as defined in Theorem 4.3.1.

Theorem 4.3.1 (Small-gain theorem) *Consider a system with a stable loop transfer function $L(s)$. Then the closed-loop system is stable if*

$$||L(j\omega)|| < 1 \quad \forall\omega, \tag{4.3}$$

where $||L||$ denotes any matrix form satisfying $||AB|| \leq ||A|| \cdot ||B||$.

Consider the block scheme in Figure 4.2. Here, the general block scheme of IBDOBC shown in Figure 4.1 is rewritten in a form suited for small-gain theorem analysis. A derivation on how this form is obtained can be found in Appendix A in Section 4.8. In order to satisfy closed-loop stability according to Theorem 4.3.1, the loop transfer function

$$L(s) = Q(s)(P_n^{-1}(s)P(s) - 1)S(s) \tag{4.4}$$

Table 4.1: Three different low-pass filter designs with poles at 100, 200 and 300 Hz to be used for $C_{lp}(z)$ (4.5).

	Pole location	Low-pass filter
$C_{lp,1}$	100 Hz	$\frac{0.47}{z-0.53}$
$C_{lp,2}$	200 Hz	$\frac{0.72}{z-0.28}$
$C_{lp,3}$	300 Hz	$\frac{0.85}{z-0.15}$

should be stable and its magnitude should be below 1. Conventional feedback controller C and plant P are generally stable. The Q-filter should be a stable LTI filter and can be used to ensure QP_n^{-1} becomes stable. Besides, it can be tuned to ensure the magnitude of the loop transfer function is below 1. The effect of different Q-filter designs on stability is further evaluated in Section 4.4, as well as the effect of plant uncertainty. Note that additionally the transfer functions in front of r and d in Figure 4.2 should be stable. This will however typically be the case, as C, QP_n^{-1}, P and T are generally stable.

4.4 Q-filter design

The Q-filter design is very similar to the approach taken in Section 2.3.1 to reconstruct the dynamics of the pump ripple. Again, P_n (2.2) is used as a nominal plant model. The model is NMP and strictly proper, such that its inverse is unstable and non-proper. The Q-filter is again used to ensure that $Q(z)P_n^{-1}(z)$ is stable and proper. To ensure stable inversion, ZMETC (2.18) is used. However, in contrast to Section 2.3.1, where three delays were used to ensure properness of $Q(z)P_n^{-1}(z)$, a cubed first-order low-pass filter is used. Specifically, the Q-filter design is given by

$$Q(z) = \frac{B_u(z)}{B_u^*(z)} C_{lp}^3(z). \tag{4.5}$$

The choice for a low-pass filter, thereby attenuating high-frequency components in the input disturbance estimation, is substantiated as follows. Pump ripple frequencies are known to mainly occur at lower frequencies, especially up to 54 Hz (Section 2.3.1). Besides, high-frequency content in the input disturbance estimation is undesired as it induces actuator wear when being compensated for. Also, the accuracy of the input disturbance estimation reduces for higher frequencies, as indicated by the estimation error in Figure 2.9. And finally, high-frequency input disturbances are already attenuated by roll-off of the plant.

Furthermore, there exists are trade-off between disturbance rejection and stability within the design of the Q-filter. The pole of low-pass filter C_{lp} can be used to balance this trade-off desirably. Further in this section, three different low-pass filter designs are compared in performance and stability characteristics using simulations. Performance is compared with frequency domain information on tracking and disturbance rejection (4.2), whereas differences in stability characteristics are validated and compared using (4.3). A scenario with and without plant uncertainty is examined. The scenario with plant uncertainty concerns an example of a situation where the actual plant has a reduced belt stiffness, which could in practice be a result of belt loosening.

4.4.1 Low-pass filter design

The pole locations of the three considered low-pass filters within the Q-filter are 100, 200 and 300 Hz. The specific designs are given in Table 4.1. Figure 4.3 shows the effect on reference tracking and disturbance rejection, i.e. the transfer from r to y and from d to y, respectively, with respect to only using linear PI2 control. A value below 1 indicates improvement, whereas a value above 1 indicates deterioration.

Figure 4.3a and 4.4a consider a scenario without plant uncertainty, i.e. $P = P_n$. Tracking performance remains unaffected, whereas disturbance rejection is improved for lower frequencies. The improvement is limited as the Q-filter does not equal 1, but also due to causality. As expected, a larger pole value results in better disturbance rejection at lower frequencies. With $C_{lp,1}$, disturbance rejection is improved up to 31 Hz, with $C_{lp,2}$ up to 48 Hz and with $C_{lp,3}$ up to 58 Hz. Besides, Figure 4.4a indicates stability is ensured for each of the three designs. Considering prominent pump ripple frequencies mainly occur up to 54 Hz (Chapter 2.3.1), $C_{lp,3}$ seems most suited.

However, in practice, different plant uncertainties could be present, i.e. $P \neq P_n$. One probable scenario would be loosening of the belt over time, which results in a lower belt stiffness. As an example, the effect of

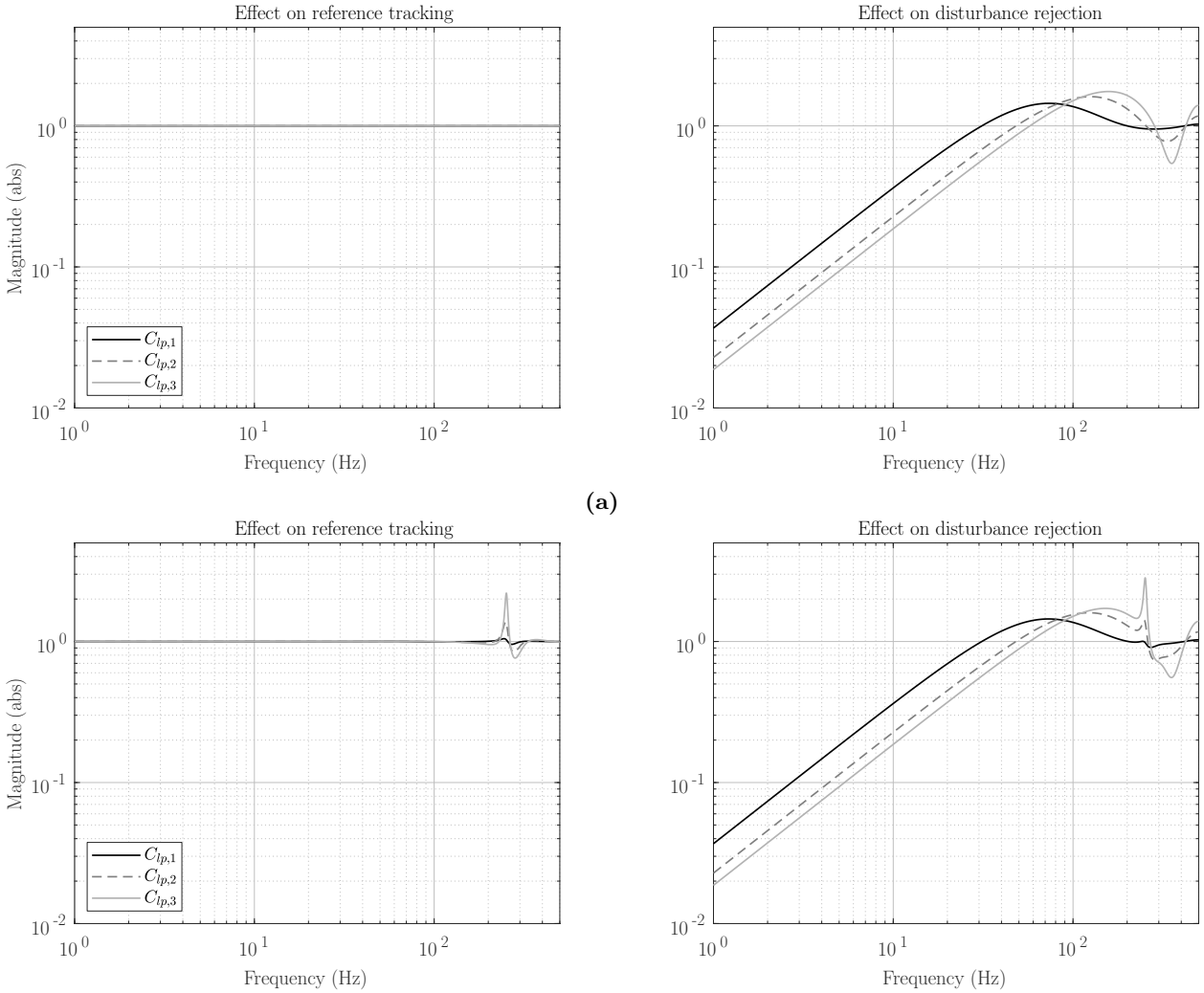

Figure 4.3: Effect on reference tracking and disturbance rejection for several different Q-filter designs compared to using only linear PI2 control, calculated by dividing the terms in front of r and d in (4.2) by the terms in front of r and d in (4.1), respectively, with (a) no plant uncertainty and (b) plant uncertainty where the actual plant has a 10% reduction in belt stiffness. A value below 1 indicates improvement, whereas a value above 1 indicates deterioration.

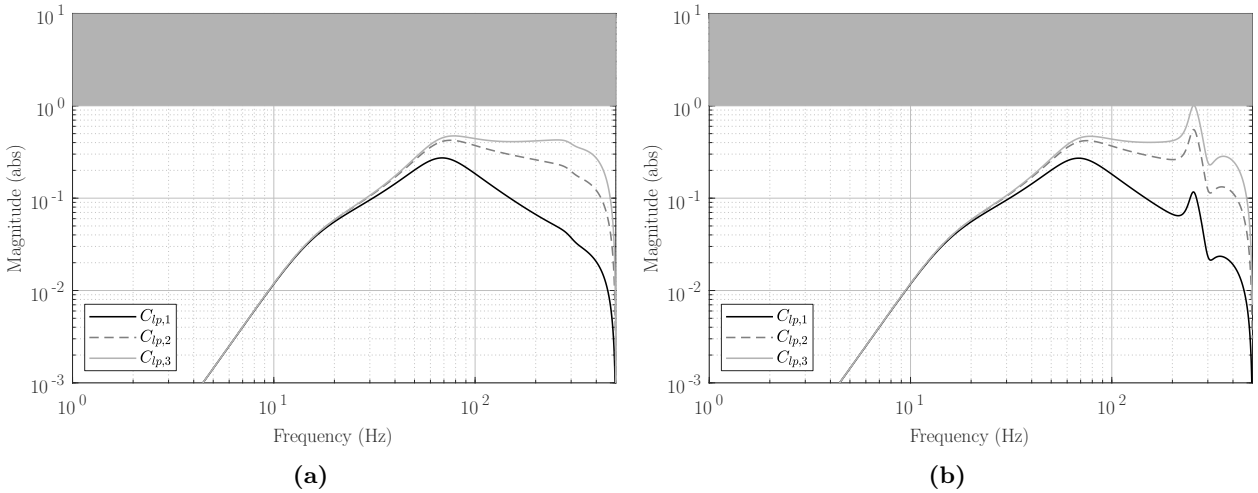

Figure 4.4: Stability condition (4.3) with each of the three low-pass filter designs with (a) no plant uncertainty and (b) plant uncertainty where the actual plant has a 10% reduction in belt stiffness.

Table 4.2: RMS values of the measured steady-state setpoint error of the motor speed with linear PI2 control and with linear PI2 control combined with IBDOBC for setpoint speeds ranging from 1 to 6 rps. Improvement is calculated using $\frac{\text{RMS linear}-\text{RMS IBDOBC \& linear}}{\text{RMS linear}} \cdot 100\%$.

Setpoint	(rps)	1	2	3	4	5	6
RMS linear	(rps)	0.085	0.170	0.277	0.386	0.454	0.501
RMS IBDOBC & linear	(rps)	0.079	0.128	0.153	0.216	0.275	0.365
Improvement	(%)	7.1	24.7	44.8	44.0	39.4	27.1

a 10% reduction in stiffness on reference tracking and disturbance rejection is considered in Figure 4.4b. For both, the low-frequency characteristics are unchanged, but above 200 Hz, where the internal anti-resonance and resonance of the belt are located, changes can be observed. The higher the pole location, the worse the effect of this stiffness reduction. Regarding reference tracking, the plant uncertainty is not so problematic as it occurs far beyond the system bandwidth. Regarding disturbance rejection, high-frequency noise, e.g. from quantization, is more amplified, which could affect performance. Besides, the reduced stiffness has an effect on stability. The higher the pole location, the closer the system is to instability. It should be noted that this is just an example of a plant uncertainty, whereas in practice different unforeseen plant uncertainties could be present.

Therefore, it is decided that the advantage of increased disturbance rejection performance up to 54 Hz does not outweigh the possibility of increased high-frequency noise amplification and instability as a result of plant uncertainty. Robustness is valued over performance here, so $C_{lp,3}$ is not chosen. Then, $C_{lp,1}$ shows significantly worse disturbance rejection performance compared to $C_{lp,2}$, while at the same time $C_{lp,2}$ is expected to be sufficiently robust against plant uncertainty. The final choice is therefore $C_{lp,2}$, such that the complete Q-filter design is given by

$$Q(z) = \frac{B_u(z)}{B_u^*(z)} C_{lp,2}^3(z). \tag{4.6}$$

4.5 Experimental results

In this section, performance with linear PI2 controller (3.5) is experimentally compared to the performance with IBDOBC combined with linear PI2 controller (3.5) on the peristaltic pump setup shown in Figure 2.1. During the experiments, the system is subject to angular speed setpoints ranging from 1 to 6 rps. For each of the six setpoints, steady-state measurements of 60 s are conducted using either of the two control methods. The measured steady-state setpoint error of the motor speed, defined as $e(t) = \dot{\theta}_1(t) - \dot{\theta}_r(t)$, is used to quantify the RMS values which are defined as performance measure in Section 1. The results are summarized quantitatively in Table 4.2 and Figure 4.5.

Small fragments of 0.5 s of the measured steady-state setpoint error of the motor speed with linear PI2 control (black) and IBDOBC combined with linear PI2 control (blue) are shown in the left column in Figure 4.5. A frequency-domain analysis in terms of the cumulative power spectral density is shown in the right column in Figure 4.5. As stated before, the square root of the cumulative power spectral density plot at the Nyquist frequency (500 Hz) indicates the RMS values of the setpoint error, for which the exact values are listed in Table 4.2. The addition of IBDOBC outperforms linear PI2 control at all considered motor speeds, with improvements in RMS values up to 44.8%. Considering setpoints speeds 3, 4, 5 and 6 rps, both Figure 4.5 as well Table 4.2 indicate that the improvement becomes smaller for higher setpoint speeds. This observation is in line with the expected improved disturbance rejection performance coming from the frequency domain plots in Figure 4.3a, as for higher setpoint speeds, pump ripple frequencies are higher (Section 2.3.2), whereas disturbance suppression is smaller. At a setpoint speed of 1 and 2 rps, improvement is smaller than expected based on these plots. This seems mainly attributed to quantization. At lower speeds, the fixed quantization step size is larger relative to the setpoint error. However, with IBDOBC the setpoint error is even smaller, such that additional quantization power content seems to appear around 65 Hz and 130 Hz, resulting in a larger effect of quantization relative to the setpoint error. This observation is similar as found with simulations in Appendix B in Section 4.9, where quantization could be included and excluded to observe its effect.

Furthermore, note that the experimental performance shows differences with the performance obtained with simulations (compare Figure 4.10 and Table 4.4 with Figure 4.5 and Table 4.2, respectively). Similar as stated in Section 3.6, this seems strongly attributed to time-variance in the dynamics of the peristaltic pump shown in Figure 2.1, which was observed throughout the experimental validation. The models used

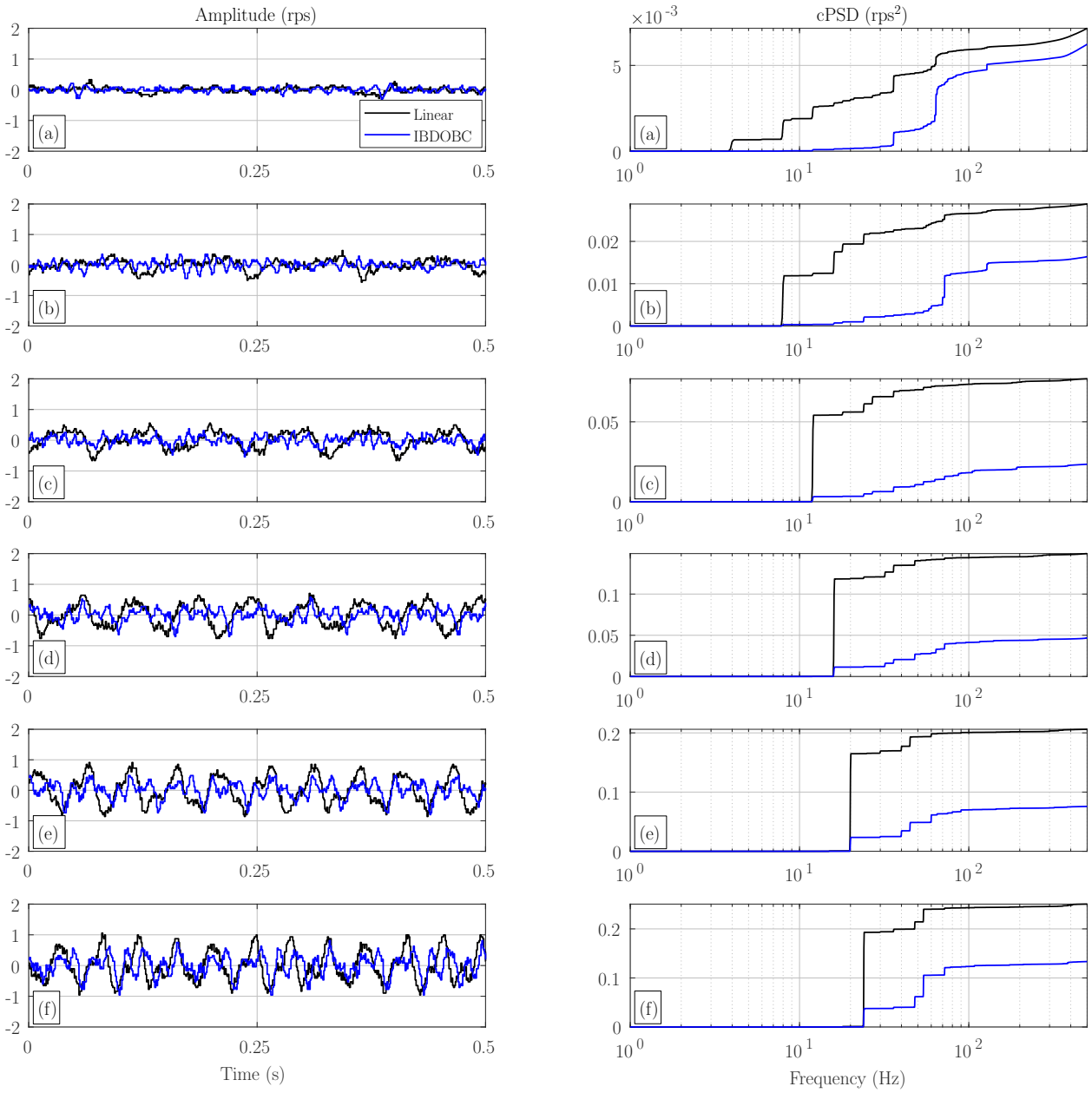

Figure 4.5: (left) Steady-state time domain measurements and (right) cumulative power spectral density representation of the setpoint error with linear PI2 control (black) and with IBDOBC combined with linear PI2 control (blue) for setpoint speeds ranging from (a) 1; (b) 2; (c) 3; (d) 4; (e) 5; to (f) 6 rps.

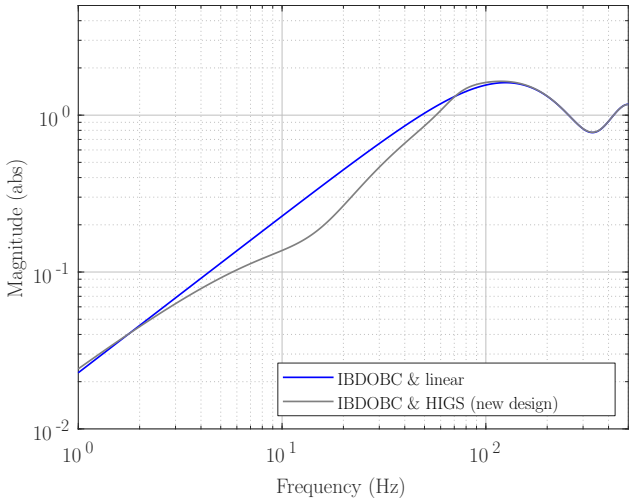

Figure 4.6: Effect on disturbance rejection with IBDOBC combined with linear PI2 control (blue) and with IBDOBC combined with HIGS-based PI2 control (dark gray), calculated by dividing the terms in front d in (4.2) by the terms in front d in (4.1). A value below 1 indicates improvement compared to using only linear PI2 control, whereas a value above 1 indicates deterioration.

Table 4.3: RMS values of the measured steady-state setpoint error of the motor speed with linear PI2 control and with HIGS-based PI2 control combined with IBDOBC for setpoint speeds ranging from 1 to 6 rps. Improvement is calculated using $\frac{\text{RMS linear} - \text{RMS IBDOBC \& HIGS}}{\text{RMS linear}} \cdot 100\%$.

Setpoint	(rps)	1	2	3	4	5	6
RMS linear	(rps)	0.085	0.170	0.277	0.386	0.454	0.501
RMS IBDOBC & HIGS	(rps)	0.078	0.136	0.145	0.191	0.248	0.325
Improvement	(%)	8.2	20	47.7	50.5	45.4	35.1

within the simulations are based on measurement data from a different day compared to the measurement data in this section. Time-variance of the dynamics is not further analyzed in this thesis.

4.6 Combination with hybrid integrator-gain-based control

In this section, performance of IBDOBC combined with the new HIGS-based PI2 controller design (Section 3.4) is experimentally compared to the performance with IBDOBC combined with linear PI2 controller (3.5) on the peristaltic pump setup shown in Figure 2.1. Stability is verified using Theorem 4.3.1, for which the HIGS-based PI2 controller is again approximated in the frequency domain using describing function analysis, similar as in Section 3.4. The corresponding results are comparable to the results of IBDOBC combined with linear PI2 control and are therefore not further elaborated on. Expected performance differences are constructed by means of (approximate) sensitivity function plots, as shown in Figure 4.6, where a value below 1 indicates improvement compared to only using linear PI2 control, whereas a value above 1 indicates deterioration. With the combination of IBDOBC and HIGS-based PI2 control one expects improved performance within a frequency range of 1 to 70 Hz compared to the combination of IBDOBC and linear PI2 control, with the largest improvements around 15 Hz. For the experiments, the same methodology is conducted as elaborated on in Section 4.5. The results are summarized quantitatively in Table 4.3 and Figure 4.7.

Small fragments of 0.5 s of the measured steady-state setpoint error of the motor speed with linear PI2 control (black) and IBDOBC combined with HIGS-based PI2 control (dark gray) are shown in the left column in Figure 4.5. A frequency-domain analysis in terms of the cumulative power spectral density is shown in the right column in Figure 3.11, additionally showing the measured steady-state setpoint error of the motor speed with HIGS-based PI2 control (red) as reference and with IBDOBC combined with linear PI2 control (blue). IBDOBC combined with HIGS-based PI2 control outperforms linear PI2 control at all considered motor speeds, with improvements in RMS value up to 50.5%. It shows similar or improved performance compared to IBDOBC combined with linear PI2 control, with larger improvements for higher motor speeds. At a motor speed of 1 and 2 rps, the base frequency of the pump ripple (4 and 8 Hz respectively) shows to be less attenuated compared to IBDOBC combined with linear PI2 control. This is not in line with the

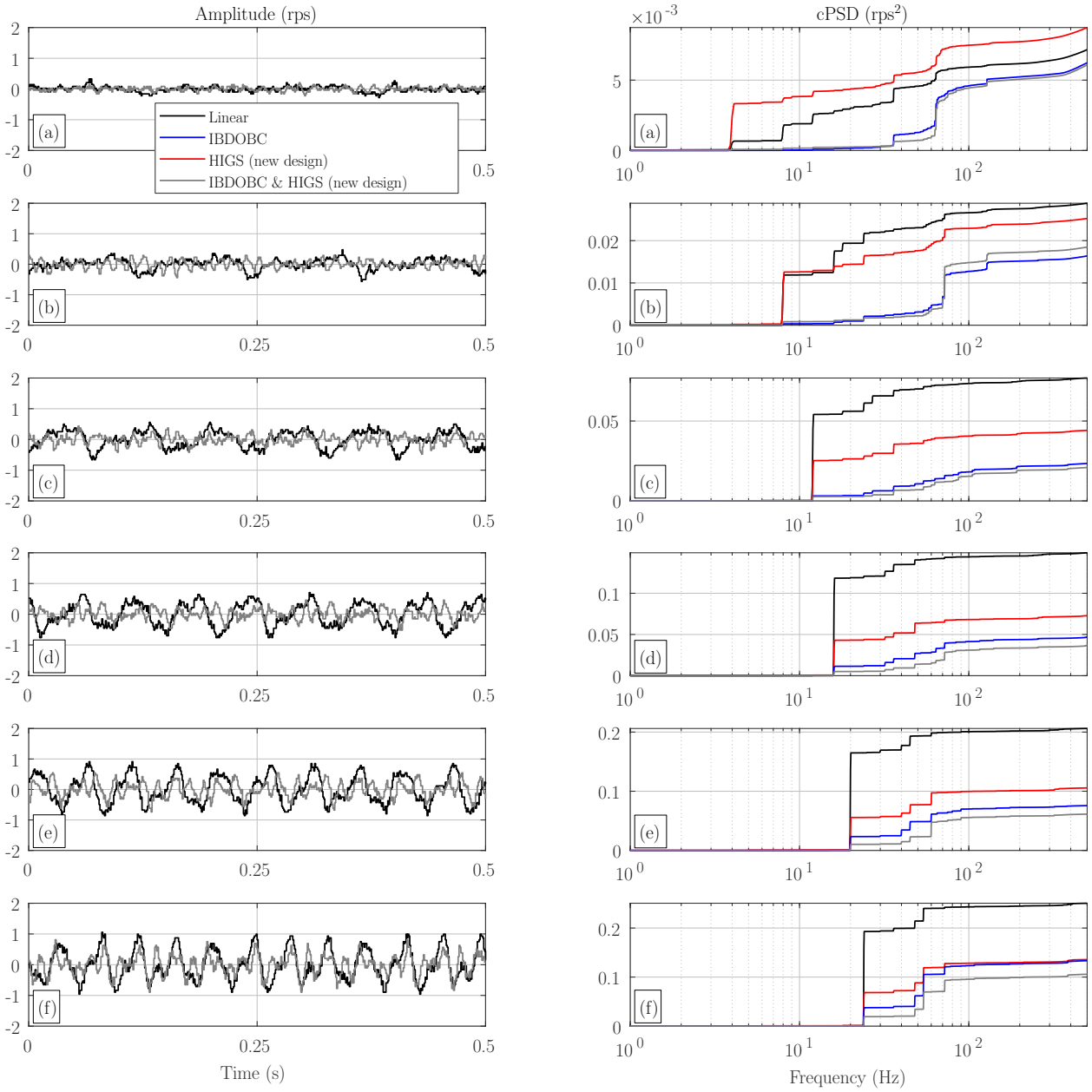

Figure 4.7: (left) Steady-state time domain measurements and (right) cumulative power spectral density representation of the setpoint error with linear PI2 controller (3.5) (black) and with the combination of IBDOBC with the newly designed HIGS-based PI2 controller (Section 3.4) (gray) for setpoint speeds ranging from (a) 1; (b) 2; (c) 3; (d) 4; (e) 5; to (f) 6 rps. For comparison, results with the newly designed HIGS-based PI2 controller and results with the linear PI2 controller combined with IBDOBC are also shown in the cumulative power spectral density plot.

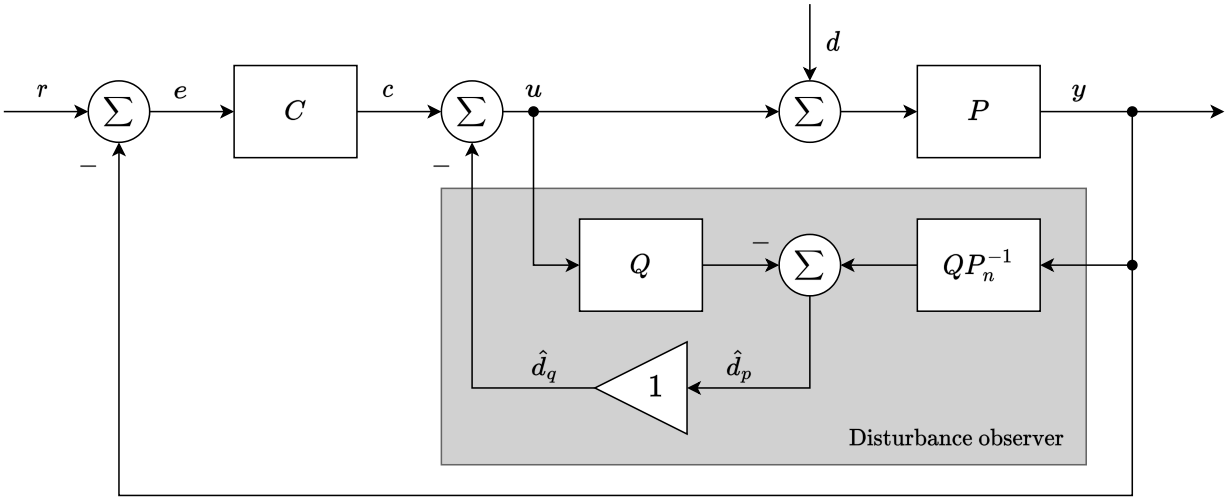

Figure 4.8: Adjusted block scheme of IBDOBC. Compared to the general block scheme of IBDOBC shown in Figure 4.1, $\hat{d}$ is split into $\hat{d}_p$ and $\hat{d}_q$.

expectations coming from (approximate) sensitivity function plots shown in Figure 4.6. This seems a typical result of gain loss [11]. Relatively high-amplitude quantization frequencies seem to be present around 65 Hz and 130 Hz, similar as found in Section 4.5, but also from 350 Hz onward. This parasitic high-frequency quantization content seems to be the main factor causing gain loss at 4 and 8 Hz at a setpoint speed of 1 and 2 rps, respectively.

4.7 Conclusions

This chapter presented an IBDOBC design for the peristaltic pump developed by Demcon for the purpose of reducing the steady-state setpoint error of the motor speed compared to linear PI2 control. The design consists of a nominal plant model and a so-called Q-filter. The Q-filter is used to ensure that inversion of the nominal plant model results in a stable and proper system, and to enforce stability of the closed-loop system. Experimental results with IBDOBC show performance improvements compared to linear PI2 control for all considered motor speeds, with improvements up to 44.8% in terms of RMS value when combined with linear PI2 control and up to 50.5% when combined with HIGS-based PI2 control. Improvements at lower speeds are less than expected based on frequency domain characterisations, which seems a result of quantization. The combination with HIGS-based PI2 control additionally seems to suffer from gain loss at lower motor speeds.

4.8 Appendix A: Small-gain theorem for IBDOBC

In this section, the general block scheme of IBDOBC shown in Figure 4.1 is rewritten in a form suited for small-gain theorem analysis, which is performed in Section 4.3. For this, first consider the adjusted block scheme shown in Figure 4.8, where $\hat{d}$ is split into $\hat{d}_p$ and $\hat{d}_q$. For small-gain theorem analysis, the loop-gain between $\hat{d}_p$ and $\hat{d}_q$ should be derived.

For this, let us first rewrite u as function of $\hat{d}_q$ and inputs r and d, so

$$\begin{aligned} u &= c - \hat{d}_q, \\ &= C(r - y) - \hat{d}_q, \\ &= C(r - P(d + u)) - \hat{d}_q, \\ &= Cr - PCd - PCu - \hat{d}_q, \\ (1 + PC)u &= Cr - PCd - \hat{d}_q, \end{aligned}$$

where dependence on Laplace variable s is omitted for reasons of clarity. Solving for u gives

$$u = CSr - Td - S\hat{d}_q, \tag{4.7}$$

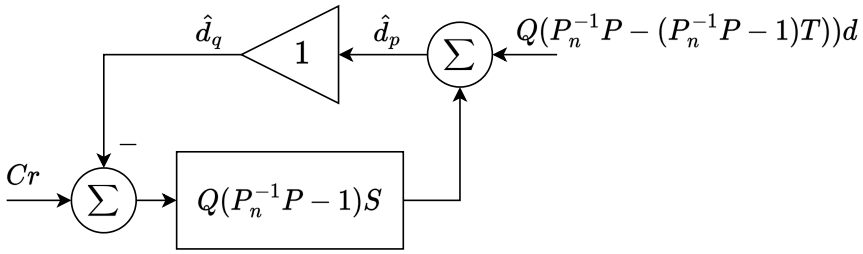

Figure 4.9: Adjusted block scheme of IBDOBC rewritten.

Table 4.4: RMS values of the simulated steady-state setpoint error of the motor speed with linear PI2 control and with linear PI2 control combined with IBDOBC for setpoint speeds ranging from 1 to 6 rps. Improvement is calculated using $\frac{\text{RMS linear} - \text{RMS IBDOBC \& linear}}{\text{RMS linear}} \cdot 100\%$.

Setpoint	(rps)	1	2	3	4	5	6
RMS linear	(rps)	0.064	0.218	0.383	0.558	0.703	0.822
RMS IBDOBC & linear	(rps)	0.033	0.071	0.140	0.238	0.365	0.582
Improvement	(%)	48.4	67.4	63.4	57.3	48.1	29.2

with

$$S = \frac{1}{1+PC}, \quad T = \frac{PC}{1+PC}. \tag{4.8}$$

As an intermediate step, let us write $\hat{d}_p$ as function of inputs d and u, so

$$\begin{aligned} \hat{d}_p &= QP_n^{-1}y - Qu, \\ &= QP_n^{-1}(P(d+u) - Qu, \\ &= QP_n^{-1}Pd + QP_n^{-1}Pu - Qu, \\ &= QP_n^{-1}Pd + Q(P_n^{-1}P - 1)u. \end{aligned} \tag{4.9}$$

Substitution of (4.9) in (4.7) results in the final relation for $\hat{d}_p$ as function of $\hat{d}_q$ and inputs r and d, thereby also obtaining the loop-gain between $\hat{d}_p$ and $\hat{d}_q$, so

$$\begin{aligned} \hat{d}_p &= QP_n^{-1}Pd + Q(P_n^{-1}P - 1)(CSr - Td - S\hat{d}_q), \\ &= QP_n^{-1}Pd + Q(P_n^{-1}P - 1)CSr - Q(P_n^{-1}P - 1)Td - Q(P_n^{-1}P - 1)S\hat{d}_q, \\ &= Q(P_n^{-1}P - 1)CSr + Q(P_n^{-1}P - (P_n^{-1}P - 1)T)d - Q(P_n^{-1}P - 1)S\hat{d}_q. \end{aligned} \tag{4.10}$$

Using this relation, the block scheme shown in Figure 4.8 can be rewritten into the form shown in Figure 4.9. Finally, Figure 4.2 shows the corresponding block scheme without splitting $\hat{d}$ into $\hat{d}_p$ and $\hat{d}_q$.

4.9 Appendix B: Simulation results

In this section, performance with linear PI2 controller (3.5) is compared to the performance with IBDOBC combined with linear PI2 controller (3.6) using simulations. For this, nominal plant model P_n (2.2) is subjected to angular speed setpoints ranging from 1 to 6 rps. For each setpoint, steady-state simulations of 60 s are conducted using either linear PI2 control (3.5) or IBDOBC combined with linear PI2 control (3.5). Plant uncertainty is not considered, i.e. $P = P_n$. The simulated steady-state setpoint error of the motor speed, defined as $e(t) = \dot{\theta}_1(t) - \dot{\theta}_r(t)$, is used to quantify the root-mean-square (RMS) value of the setpoint error, which was defined as performance measure in Section 1. The results are summarized quantitatively in Table 4.4 and Figure 4.10.

Small fragments of 0.5 s of the simulated steady-state setpoint error with linear PI2 control (black) and linear PI2 control combined with IBDOBC (blue) are shown in the left column in Figure 4.10, whereas a frequency-domain analysis in terms of the cumulative power spectral density is shown in the right column in Figure 4.10. The addition of IBDOBC significantly outperforms linear PI2 control at all considered motor speeds, with improvements in RMS value up to 67.4%. Apart from a setpoint speed of 1 rps, both Figure 4.10 as well Table 4.4 indicate increasing improvement for lower setpoint speeds. This observation is in line with

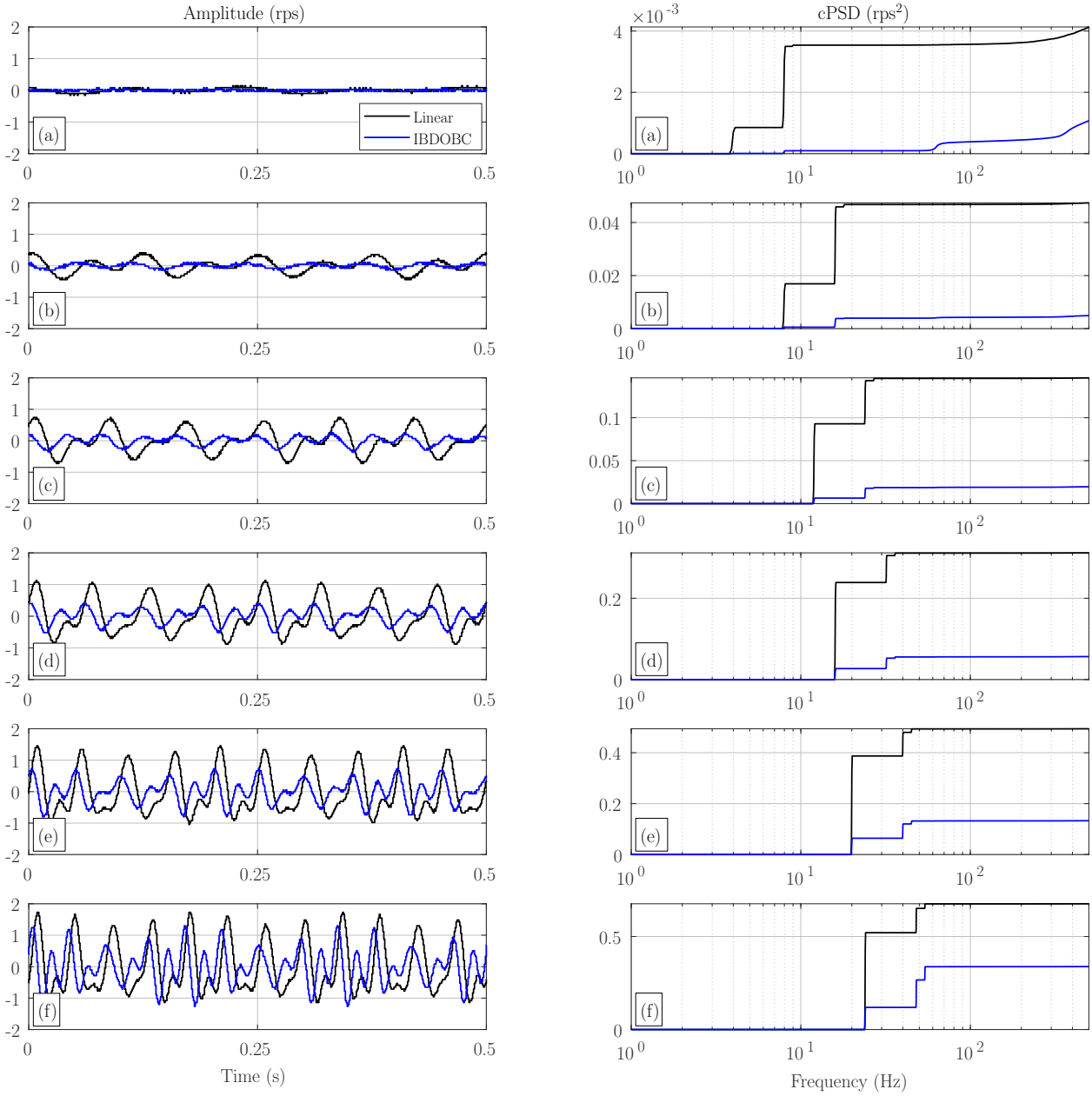

Figure 4.10: (left) Steady-state time domain simulations and (right) cumulative power spectral density representation of the setpoint error with linear (black) and IBDOBC (blue) for setpoint speeds ranging from (a) 1; (b) 2; (c) 3; (d) 4; (e) 5; to (f) 6 rps.

the expected improved disturbance rejection performance coming from the frequency domain plots in Figure 4.3a, as for lower setpoint speeds, pump ripple frequencies are lower (Section 2.3.2), whereas disturbance suppression is larger. At a motor speed of 1 rps, improvement is smaller than expected based on these plots. This is attributed to quantization. At lower speeds, the fixed quantization step size is larger relative to the setpoint error. However, with IBDOBC the setpoint error is even smaller, such that additional quantization power content seems to appear around 65 Hz, resulting in a larger effect of quantization relative to the setpoint error.

Chapter 5

Conclusions and recommendations

5.1 Conclusions

In this thesis, a HIGS-based PI2 controller is presented with the objective to reduce the steady-state setpoint error of the motor speed of a peristaltic pump while at least maintaining robustness margins obtained with linear PI2 control. Besides, an IBDOBC design that can be combined with either linear or HIGS-based PI2 control is presented with the objective to reduce the steady-state setpoint error of the motor speed of a peristaltic pump.

Models of the peristaltic pump and its prominent experienced disturbances are used to realize the HIGS-based PI2 controller and IBDOBC design. A structured tuning methodology for HIGS-based PI2 controller design was developed and used to improve upon an initial HIGS-based PI2 controller design. This initial design was also developed within this thesis and was presented by means of a conference paper. Simulation results indicated similar performance at higher speeds, but improvements up 24.7% in terms of RMS value at lower speeds with the new HIGS-based PI2 controller design compared to the HIGS-based PI2 controller design from the paper. Key for these improvements was contributed to a switch from series to parallel baseline configuration, a different gain loss filter and different values for HIGS tuning parameter ω_h.

Finally, experimental validation of the new HIGS-based PI2 controller design showed slightly deteriorated performance at the lowest motor speed compared to linear PI2 control, which seems to be attributed to gain loss, but improved performance for all higher considered motor speeds, showing improvement up to 30.1% in terms of RMS value. Transient performance was additionally enhanced as well, showing improvements up to 50.0% in terms of overshoot for similar rise time compared to linear PI2 control.

Experimental results with IBDOBC showed performance enhancements compared to linear PI2 control for all considered motor speeds, with improvements up to 44.8% in terms of RMS value when combined with linear PI2 control and up to 50.5% when combined with HIGS-based PI2 control. Improvements at lower speeds were less than expected based on frequency domain characterisations, which seemed a result of quantization.

5.2 Recommendations

Based on the results and conclusions presented in this thesis, several recommendations for future research directions are formulated:

- Stability with the HIGS-based PI2 controller is validated using the Nyquist stability criterion, for which both HIGS elements are approximated using describing function analysis. No formal stability proof of the HIGS-based PI2 controller exists yet, whereas the existence of this would ensure more certainty regarding stability. Especially in the medical industry, where design requirements are generally strict, such a proof would be greatly valued.

- The transient performance with IBDOBC has not been evaluated in this thesis. However, it would be interesting to see whether IBDOBC combined with either linear or HIGS-based PI2 control improves or deteriorates the transient performance compared to not using IBDOBC.

- Robust performance and stability of IBDOBC has been addressed in this thesis by means of an example of a probable plant uncertainty. However, a suitable method to analyse robust stability and performance with IBDOBC in the presence of plant uncertainties in general is missing and not yet available in literature.

- The peristaltic pump setup used in this thesis seems to exhibit time-variant dynamics. This seems largely attributed to the degradation of the stiffness of the disposable tubes used during pump operation. Besides, slight misalignments resulting from shock loads or thermal effects possibly further alter the dynamics of the peristaltic pump from time to time. A more thorough analysis on this time-variance might be beneficial to eventually design a suitable robust controller or realize an improved mechanical redesign of the pump.

- In this thesis, HIGS-based PI2 control and IBDOBC are considered approaches to reduce the effects of the pump ripple, without using the periodicity of the pump ripple. Control methods that would make use of this periodicity, such as repetitive control, seem promising as well. One could apply such a strategy in the time domain, but also in the spatial domain to make the compensation independent of the actual pump speed [21].

- In this thesis, only the disturbance corresponding to the pulsation/ripple about the desired speed is considered: the pump ripple. However, the peristaltic pump principle introduces an additional periodic disturbance as a result of the fact that fluid is displaced in parts, resulting in a so-called flow ripple. One could use an external flow sensor to analyze the severity of this ripple on the flow and thereby determine whether additional control action would be desired. Similar as for the pump ripple, disturbance-observer-based control methods might be suited for this.

Bibliography

[1] J. Klespitz and L. Kovács, "Peristaltic pumps—a review on working and control possibilities," in *2014 IEEE 12th International Symposium on Applied Machine Intelligence and Informatics (SAMI)*. IEEE, 2014, pp. 191–194.

[2] E. Smolinski, A. Benkmann, W. Drewelow, T. Jeinsch, and H.-J. Cappius, "Observer-based controller design for the minimally invasive surgery," *Current Directions in Biomedical Engineering*, vol. 4, no. 1, pp. 41–44, 2018.

[3] J. Klespitz and L. Kovács, "Identification and control of peristaltic pumps in hemodialysis machines," in *2013 IEEE 14th International Symposium on Computational Intelligence and Informatics (CINTI)*. IEEE, 2013, pp. 83–87.

[4] R. H. Munnig Schmidt, G. Schitter, and J. van Eijk, *The design of high performance mechatronics. High-tech functionality by multidisciplinary system integration.* IOS Press, 2011.

[5] M. M. Seron, J. H. Braslavsky, and G. C. Goodwin, *Fundamental Limitations in Filtering and Control*. Springer, 1997.

[6] J. Freudenberg and D. Looze, "Right half plane poles and zeros and design tradeoffs in feedback systems," *IEEE transactions on automatic control*, vol. 30, no. 6, pp. 555–565, 1985.

[7] M. F. Heertjes, S. J. A. M. van den Eijnden, and B. Sharif, "An overview on hybrid integrator-gain systems with applications to wafer scanners," in *2023 IEEE International Conference on Mechatronics (ICM)*, 2023, pp. 1–8.

[8] L. F. van Eijk, S. Beer, R. M. J. van Es, D. Kostić, and H. Nijmeijer, "Frequency-domain properties of the hybrid integrator-gain system and its application as a nonlinear lag filter," *IEEE Transactions on Control Systems Technology*, vol. 31, no. 2, pp. 905–912, Mar. 2023.

[9] M. F. Heertjes, N. Irigoyen, and D. A. Deenen, "Data-driven tuning of a hybrid integrator-gain system," *IFAC-PapersOnLine*, vol. 50, no. 1, pp. 10 851–10 856, Jul. 2017.

[10] S. J. A. M. van den Eijnden, M. F. Heertjes, and H. Nijmeijer, "Experimental demonstration of a nonlinear PID-based control design using multiple hybrid integrator-gain elements," in *2020 American Control Conference (ACC)*. IEEE, jul 2020.

[11] M. F. Heertjes, S. J. A. M. van den Eijnden, W. P. M. H. Heemels, and H. Nijmeijer, "A solution to gain loss in hybrid integrator-gain systems," in *2021 IEEE Conference on Control Technology and Applications (CCTA)*. IEEE, aug 2021.

[12] L. Guo and S. Cao, "Anti-disturbance control theory for systems with multiple disturbances: A survey," *ISA Transactions*, vol. 53, no. 4, pp. 846–849, Jul. 2014.

[13] S. Li, J. Yang, W.-H. Chen, and X. Chen, *Disturbance observer-based control: Methods and applications*. Institute of Electrical and Electronics Engineers (IEEE), 2014.

[14] K. Ohishi, M. Nakao, K. Ohnishi, and K. Miyachi, "Microprocessor-controlled dc motor for load-insensitive position servo system," *IEEE Transactions on Industrial Electronics*, vol. IE-34, no. 1, pp. 44–49, Feb. 1987.

[15] W.-H. Chen, J. Yang, L. Guo, and S. Li, "Disturbance-observer-based control and related methods—an overview," *IEEE Transactions on Industrial Electronics*, vol. 63, no. 2, pp. 1083–1095, Feb. 2016.

[16] G. Hillerström and K. Walgama, "Repetitive control theory and applications - a survey," *IFAC Proceedings Volumes*, vol. 29, no. 1, pp. 1446–1451, Jun. 1996.

[17] J. Butterworth, L. Pao, and D. Abramovitch, "Analysis and comparison of three discrete-time feedforward model-inverse control techniques for nonminimum-phase systems," *Mechatronics*, vol. 22, no. 5, pp. 577–587, Aug. 2012.

[18] S. J. A. M. van den Eijnden, M. F. Heertjes, W. P. M. H. Heemels, and H. Nijmeijer, "Hybrid integrator-gain systems: A remedy for overshoot limitations in linear control?" *IEEE Control Systems Letters*, vol. 4, no. 4, pp. 1042–1047, oct 2020.

[19] J. C. Clegg, "A nonlinear integrator for servomechanisms," *Transactions of the American Institute of Electrical Engineers, Part II: Applications and Industry*, vol. 77, no. 1, pp. 41–42, 1958.

[20] S. Skogestad and I. Postlethwaite, *Multivariable feedback control: analysis and design.* John Wiley & sons, 2005.

[21] G. Hillerstrom and J. Sternby, "Application of repetitive control to a peristaltic pump," in *1993 American Control Conference.* IEEE, 1993, pp. 136–141.